Investigation of Local and Average Structure in Li-ion Battery Electrode Materials by X-ray Diffraction

PhD dissertation

M.Sc. Murat Yavuz

TECHNISCHE
UNIVERSITÄT
DARMSTADT

MATERIAL-
WISSENSCHAFT

Ehrenwörtliche Erklärung

Ich erkläre hiermit ehrenwörtlich, dass ich die vorliegende Arbeit selbstständig angefertigt habe. Sämtliche aus fremden Quellen direkt oder indirekt übernommenen Gedanken sind als solche kenntlich gemacht.

Die Arbeit wurde bisher keiner anderen Prüfungsbehörde vorgelegt und noch nicht veröffentlicht.

Darmstadt, den 9. November 2015

Investigation of Local and Average Structure in Li-ion Battery Electrode Materials by X-ray Diffraction

Vom Fachbereich Material- und Geowissenschaften
der Technische Universität Darmstadt

zur Erlangung des akademischen Grades
Doktor-Ingenieur
(Dr.-Ing.)

genehmigte Dissertation
von
Murat Yavuz M.Sc.
geboren in Tekirdağ, Türkei

1. Prüfer : Prof. Dr. rer. nat. Wolfgang Donner
   Technische Universität Darmstadt (TUD)
2. Prüfer : Prof. Dr. rer. nat. Helmut Ehrenberg
   Karlsruhe Institut für Technologie (KIT)

Tag der Einreichung : 09/11/2015
Tag der mündlichen Prüfung : 11/12/2015

Darmstadt 2016
D 17

Contents

Abbreviations

B(r)	envelope function
BEVs	Battery Electric Vehicles
χ^2	the goodness-of-fit parameter
C	capacity
C-rate	charge/discharge rate
$\Delta E^0(anode)$	standard electrode potential at the anode side
$E^0(cathode)$	standard electrode potential at the cathode side
EREVs	Extended-Range Electric Vehicles
EVs	Electric Vehicles
F	Faraday constant
F_{hkl}	structure factor
f_i	scattering factors for atom i
G(r)	Pair Distribution Function
HEVs	Hybrid Electric Vehicles
HRPD	High Resolution Powder Diffraction
HRTEM	High Resolution Transmission Electron Microscopy

I	Current
I^{coh}	Coherently scattered intensity
ICP-OES	Inductively coupled plasma-optical emission spectroscopy
k	wave vector
LCO	$LiCoO_2$
LFP	$LiFePO_4$
LIBs	Lithium Ion Batteries
LMO	$LiMn_2O_4$
m	Amount of active mass involved in the reaction
MSPD	Material Science Powder Diffraction
NCA	Lithium Nickel Cobalt Aluminium Oxide
NiMH	Nickel Metal Hydrides
NMC	Lithium Nickel Manganese Coblat Oxide
NMR	Nuclear Magnetic Resonance
p	specific power
PDF	Pair Distribution Function
PHEVs	Plug-in Hybrid Electric Vehicles
p_v	power density
Q	magnitude of the scattering vector

r	distance
RDF	Radial Distribution Function
R_{exp}	Expected Weighted Profile Factor
R_p	Profile Factor
R_{wp}	Weighted Profile Factor
S(Q)	total scattering function
SEI	Solid Electrolyte Interphase
SHE	Standard Hydrogen Electrode
t	time
V	volume
w	specific energy
w_i	the weighting factor
W_V	Energy density
Y_{calc_i}	the observed intensity
Y_{obs_i}	the calculated intensity
δ	Dirac delta function
ρ(r)	the microscopic pair density
σ	standard deviation

List of Figures

List of Tables

Abstract

In order to study structure and microstructure of crystalline materials, the powder diffraction method, which allows rapid and non-destructive analysis of multi-component mixtures is now one of the most widely used technique in many research fields.

In this work,

i) the instrument parameters of a Mo-$K_{\alpha1}$ diffractometer, the P02.1 beamline at Petra III and the MSPD beamline at ALBA for both real and reciprocal space are determined. The real space resolution LaB_6 in the PDF are 0.1977 Å, 0.1009 Å and 0.1193 Å for a Mo-$K_{\alpha1}$ diffractometer, the P02.1 beamline at Petra III (SDD 200mm) and the MSPD beamline at ALBA, respectively. On the other hand, the angular resolution in the Rietveld refinement of LaB_6 are 0.0666°, 0.0556° and 0.0281°.

ii) the average and local structure of nanocrystalline $Al_{0.57}Sn_{0.43}O_{1.71}$ anode material was investigated using conventional Rietveld refinement and X-ray Pair Distribution Function (PDF) technique. The crystallite sizes of both $Al_{0.57}Sn_{0.43}O_{1.71}$ nanoparticles synthesized at 550°C and 40°C determined from the peak attenuation in the PDF refinement are about 20 Å, which are smaller in the Rietveld refinement due to the small size of the nanoparticles, which results in peak broadening. According to the weight-independent partial PDFs of cation-anion pairs for both samples, oxygen vacancies are located mostly around the Al atoms and cation-cation pairs for both samples illustrate a clustering of Al atoms. The volume changes during Li-Sn alloying/dealloying can be compensated by a large enough Li-Al-O matrix which may help to give better electrochemical performance. The best electrochemical cycling stability performance was obtained for the sample calcined at 550°C.

iii) the electronic structure of $LiMn_2O_4$ was obtained using Rietveld refinement and PDF methods based on *ex situ* data, and the successful application of in situ total scattering experiments on $LiMn_2O_4$ was also shown. The results of the average structure analysis of $LiMn_2O_4$ sample obtained from the Rietveld refinement are in agreement with that of PDF, however in short distances they do not match very well due to the local distortion around the Mn ions. Because of that and to illustrate the electronic structure of *ex situ* PDF data RMC refinements were performed. As a result the average valence of the Mn ions is obtained to +3.72 and the structure has 0.56 mol of Mn^{3+}. Additionally, *in situ* total scattering experiments were carried out on $LiMn_2O_4$, where background measurements were done and subtracted from the data of the active material.

Chapter 1 - Introduction

The powder diffraction method is one of the most widely used techniques available to study the structure and microstructure of crystalline materials [1]. Powder diffraction allows rapid, non-destructive analysis of multi-component mixtures without the need for extensive sample preparation. This gives laboratories the ability to quickly analyse unknown materials and perform materials characterization in such fields as chemistry, materials science, geology, mineralogy, forensics, archaeology, and the biological and pharmaceutical sciences [2]. The powder diffraction method was devised independently in 1916 by Debye and Scherrer [3] in Germany and in 1917 by Hull [4] in the United States. After half a century, this technique developed steadily and, the conventional applications were established such as phase identification, the determination of accurate unit-cell dimensions, the analysis of structural imperfections and to measure sample purity [5]. After the Second World War, rapid progress took place in the powder diffraction methods. The progress in the speed of data collection and quality of results were due to the development of instrumentation (automated diffractometers, goniometers, generators, detectors etc.), as well as the availability of digitised data and to numerical methods of structure solving and refinement [6].

In 1967, Hugo Rietveld introduced a powerful method for refining the parameters of the crystal structures from powder diffraction data [7]. Rietveld refinement is described simply as matching the entire experimental diffraction pattern and the model which is created based on this experimental data by refining both instrumental and structure parameters until the best fit is reached.

Modern technology demands nanoparticles and more sophisticated complex materials because of having higher performance. To investigate the nanoparticles and to increase the performance of complex functional materials, it is crucial to understand the properties of these materials. Increasingly, these complex materials have disorder and the shortcomings of the conventional crystallographic analysis become apparent. The conventional crystallographic analysis is based on Bragg reflections that relate to the long-range average structure of materials. It ignores the weak diffuse scattering that contains valuable information about the local structure. As a result, it gives only spatially averaged information of the structure and the information regarding the local deviations from the perfect lattice is not represented accurately. An alternative approach is the so-called total scattering technique and treats both, the Bragg and diffuse scattering (i.e. all diffraction data). Fourier transformation of the total scattering data is known as Pair Distribution Function (PDF) analysis [8,9].

The Pair Distribution Function (PDF) that is a description of the real space structure gives the probability of finding a pair of atoms at a distance of r. The PDF method has successfully been used in the study of liquids, glasses and other amorphous materials which have no long range order at all and crystalline materials as well [8–11].

With the rapid development of portable electronic devices, and electrical/hybrid cars much attention has been paid to high energy and high power density lithium ion batteries (LIBs) [12–14]. Recent investigation shows that higher power and energy densities could be achieved by introducing disorder into the electrode. By properly controlling the type and degree of disorder, the electrochemical properties of lithium ion batteries can be improved in some cases. Calcination temperature or doping plays an effective role on the degree of disorder and in enhancing the performance [15,16]. The alternative approach to conventional crystallographic analysis, the PDF analysis on the disordered structure of electrodes in LIBs opens up a new field of structural analysis.

It has already been reported that SnO_2 is a promising candidate material as an anode material in LIBs since it has higher capacity in comparison to graphite anode material [17–21]. However, SnO_2 type material suffers from irreversible capacity loss due to the formation of an electrochemically inactive Li_2O matrix around the active Sn metal, as well as a large volume expansion of more than 200% during electrochemical cycling [18,22,23] causing huge internal stress . Because of the stress, a capacity fading during cycling occurs, due to the loss of electric contact [24–27]. In order to overcome these drawbacks and to improve the electrochemical performance, the particle size can be reduced to 2-3 nm, which leads to a decrease of mechanical stress in the particles due to the volume expansion. Kim *et al.* showed that SnO_2 nanoparticles with an average size of 3 nm have negligible capacity fading after 60 cycles even at high charging rates [28]. On the other hand, in parallel with a reduced particle size [29–31], some of the Sn can be substituted by a second metal with different oxidation state like Al in order to induce oxygen vacancies inside the structure to improve the electrochemical performance.

In this study, the average and the local structures of the selected electrode materials are investigated. In order to do so the instrument parameters of Mo-$K_{\alpha 1}$ diffractometer, P02.1 beamline at Petra III and MSPD beamline at ALBA for both real and reciprocal space have to be determined. Then, the average and local structure investigations of nanocrystalline $Al_{0.57}Sn_{0.43}O_{1.71}$ anode material are carried out using conventional Rietveld refinement [32] and X-ray Pair Distribution Function (PDF) techniques [8,33]. The structural properties with respect to the results of electrochemistry, NMR, HRTEM and Mössbauer of nanocrystalline $Al_{0.57}Sn_{0.43}O_{1.71}$ anode material will be discussed.

The electronic structure of $LiMn_2O_4$ (determination of the oxidation state of Mn) is obtained by using the Rietveld and PDF methods based on *ex situ* data as well as the application of *in situ* total scattering experiments on $LiMn_2O_4$, as well.

Chapter 2 - FUNDAMENTALS

2.1. Battery

2.1.1. Battery Concepts

Electrochemical power sources convert chemical energy into electrical energy, and/or vice versa using redox reactions [34].

A battery consists of one or more galvanic elements which is the simplest electrochemical cell [35]. A galvanic element, which consists of electrode materials dipped into the electrolyte, is a current source where a local separation of oxidation (at the anode) and reduction (at the cathode) processes exist [34].

oxidation $$A \rightleftharpoons A^{+} + e^{-} \quad (1)$$

reduction $$B^{+} + e^{-} \rightleftharpoons B \quad (2)$$

To satisfy different applications and in order to obtain high battery voltages, the cells are connected in series (***Figure 1*-a**), and to obtain high power they should be connected in parallel (***Figure 1*-b**).

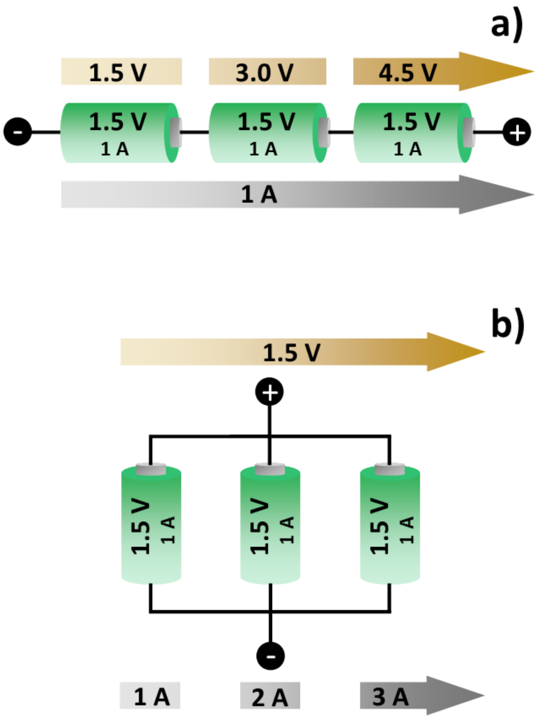

Figure 1 *- An illustration of batteries connected (a) in serial and (b) in parallel.*

Electrochemical batteries are classified into 2 categories depending on the principles of their operation;

The primary battery is a non-rechargeable cell, or group of cells [36] in which the electrochemical reaction is irreversible and it can be used only once through to the discharged state and is then discarded.

Secondary batteries are rechargeable multiple times [34]. In today´s market, the most common rechargeable batteries are lead acid, nickel-cadmium (NiCd), nickel-metal hydride (NiMH) and lithium ion batteries (LIBs). LIBs offer a high energy density, a high operational voltage, high capacity, lightweight and a long cycle lifetime. A comparison of secondary batteries is shown in ***Table 1***.

Table 1 - *Comparison of secondary batteries.*

Battery Type	Lead Acid	NiCd	NiMH	Lithium Ion
Specific Power (W/kg)	30 – 50	40 – 60	60 – 120	100 – 150
Cycle Life	180	150	250 – 1000	300 – 3000
Operating Voltage (V)	4500	800 – 1200	500 – 2000	>2000
Operating Temperature (^0C)	~2.1	~1.2	1.2	0.5 – 5
Charge/discharge efficiency (%)	-80	-90	-20 – 50	-10 – 50
Charging Time (h)	50 – 92	75 – 93	66	8–90
Working Life (Year)	8	1.5	4	4–0.5
(Charge one time per day)	1	2	2	5.5
Memory Effect	No	Yes	Little	No
Cost ($/kWh)	269	280	500 – 100	Consumer electronics : 300-800 Vehicles : 1000-2000
Battery Characteristics	High reliability, Low cost	Memory effect	Memory effect, currently, best value, and most popular battery for HEVs	Small size, light weight
Application	Car battery, forklift, golf cart, backup power	Replacement for flashlight battery	HEVs, replacement for flashlight battery	Consumer electronics, HEVs, PHEVs, BEVs, EREVs

HEVs : Hybrid Electric Vehicles
PHEVs : Plug-in Hybrid Electric Vehicles
BEVs : Battery Electric Vehicles
EREVs : Extended-Range Electric Vehicles

2.1.2. Battery Characteristics

Batteries are characterized by the following parameters;

2.1.2.1. Voltage

Voltage, the electrical driving force, is equal to the difference between the standard electrodes potential at the cathode and at the anode [30,37]. The voltage of a cell which is not on charge/discharge is called open circuit voltage. On the other hand, the voltage of a cell which is connected to a circuit and produces a current through it, is called closed circuit voltage.

$$\Delta E^0(cell) = E^0(cathode) - E^0(anode) \tag{3}$$

2.1.2.2. Capacity and Specific Capacity

The capacity (C) is the total amount of charge stored in the cell and is given by

$$C = n.F = I.t\ (Ah) \tag{4}$$

The capacity is conventionally expressed as Ah/kg and called specific capacity:

$$C_{specific} = \frac{n.F}{\sum_i m_i}\ (Ah/kg) \tag{5}$$

2.1.2.3. Power Density and Specific Power

Specific power and power density are a measure of the power that can be derived per unit mass (*Eq.* 6) or volume (*Eq.* 7), respectively. The power of a battery is improved by enhancing both diffusion of ions and electrical conductivity.

$$p = \frac{I.\Delta E^0}{\sum_i m_i} \; (W/kg) \tag{6}$$

$$P_V = \frac{I.\Delta E^0}{\sum_i V_i} \; (W/l) \tag{7}$$

2.1.2.4. Energy Density and Specific Energy

Specific energy and energy density are the amount of energy delivered per unit mass and volume, respectively.

$$w = \frac{n.F.\Delta E^0}{\sum_i m_i} \; (Wh/kg) \tag{8}$$

$$W_V = \frac{n.F.\Delta E^0}{\sum_i V_i} \; (Wh/l) \tag{9}$$

2.1.2.5. The Charge/Discharge Rate

The C-rate is defined as the current to charge/discharge a battery. It is a measure of how fast the cell is charged or discharged. 1C means that the cell is either charged or discharged in 1 hour. 0.5C means that it is charged or discharged in 2 hours.

Rate capability or rate performance indicates how much capacity can be delivered by a battery or a cell at different current rates applied. A lower degree of capacity reduction at high rates is preferred.

2.1.3. Overview of Lithium Ion Batteries

Lithium secondary batteries use the lithium ions as the main charge carrier. The electrodes are dipped in the electrolyte that is an ion conduction material with low internal resistance and can be in the form of a liquid, molten salt, or in the solid state [38]. The separator is a barrier for electron transport and allows ionic transport only. As a consequence it prevents short circuits. When the electrochemical redox reaction occurs at the interface of the electrodes and electrolyte, Li ions are shuttled between the electrodes and at the same time, an electron flow starts between electrodes via the external wire in a closed circuit [30,37].

The terms of anode and cathode should always be mentioned with respect to the discharging process in the case of rechargeable batteries. Li^+ and electron transport during charging and discharging in a Li-ion cell are schematically shown in ***Figure 2***. In a discharging battery, the anode is the electrode where the electrochemical oxidation reaction (release of electrons into the external circuit) takes place and the cathode is the electrode where the electrochemical reduction reaction (gain of electrons from the external circuit) occurs. When the cell is connected to a power supply, the process occurs in reverse way. To avoid the confusion of the terms, it is better to use positive and negative electrodes for higher (cathode) and lower (anode) standard potentials, respectively.

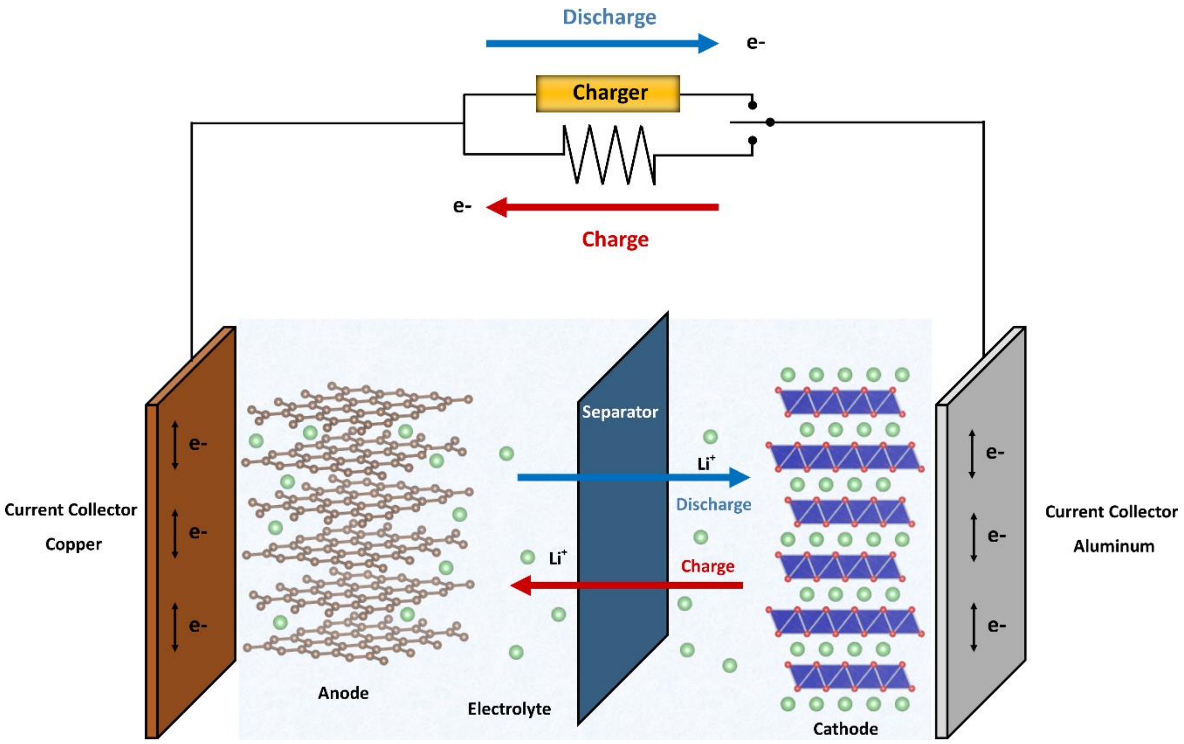

Figure 2 *– Transport of Li$^+$ and electrons during charging and discharging in a Li-ion cell.*

In the early stage of development, lithium metal was used as an anode owing to its negative redox potential (-3.05 V) and the high theoretical specific capacity (3860 mAh/g). However, it fails due to safety issues such as the formation of dendrites on the surface of lithium metal which leads to short circuits [2,39]. For that reason, the lithium metal anode was replaced by carbon-based materials such as graphite. Graphite, 372 mAh/g of theoretical specific capacity, can intercalate up to one Li per six carbon atoms between graphene layers electrochemically and reversibly at low potentials (from 0-0.25 V vs. Li$^+$/Li).

Physical and chemical properties of the most widely used commercial secondary batteries are shown in ***Table 2*** [39]. Both, ***Table 1***, ***Table 2*** and ***Figure 3*** demonstrate that lithium ion batteries show high output voltage, high energy density, long lifespan and flexible lightweight design.

The electrolyte of lithium ion batteries commonly consists of a lithium salt in an organic solvent. In recent years with an increasing interest in high voltage LIBs, the electrolyte plays a critical role because the available electrolytes are not stable at high voltages and the decomposition of electrolyte starts around 4.5 V [40]. The electrolyte for LIBs should be stable, safe and highly ionic conductive. Current collectors of LIBs conduct electricity between the electrode and the terminal [41]. Aluminium and copper foils are commonly used for the cathode and anode sides, respectively.

Table 2 *- Properties of most used commercial secondary batteries.*

	Negative Electrode	**Positive Electrode**	**Electrolyte**	**Voltage (V)**	**Cycle life**
Lithium-ion	Graphite	$LiCoO_2$	$LiPF_6$(nonaqueous)	3.7	>1000
Lead-acid	Pb	PbO_2	H_2SO_4(aqueous)	2.1	<500
NiCd	Cd	NiOOH	KOH(aqueous)	1.2	2000
NiMH	Intermetallic	NiOOH	KOH(aqueous)	1.2	500-1000

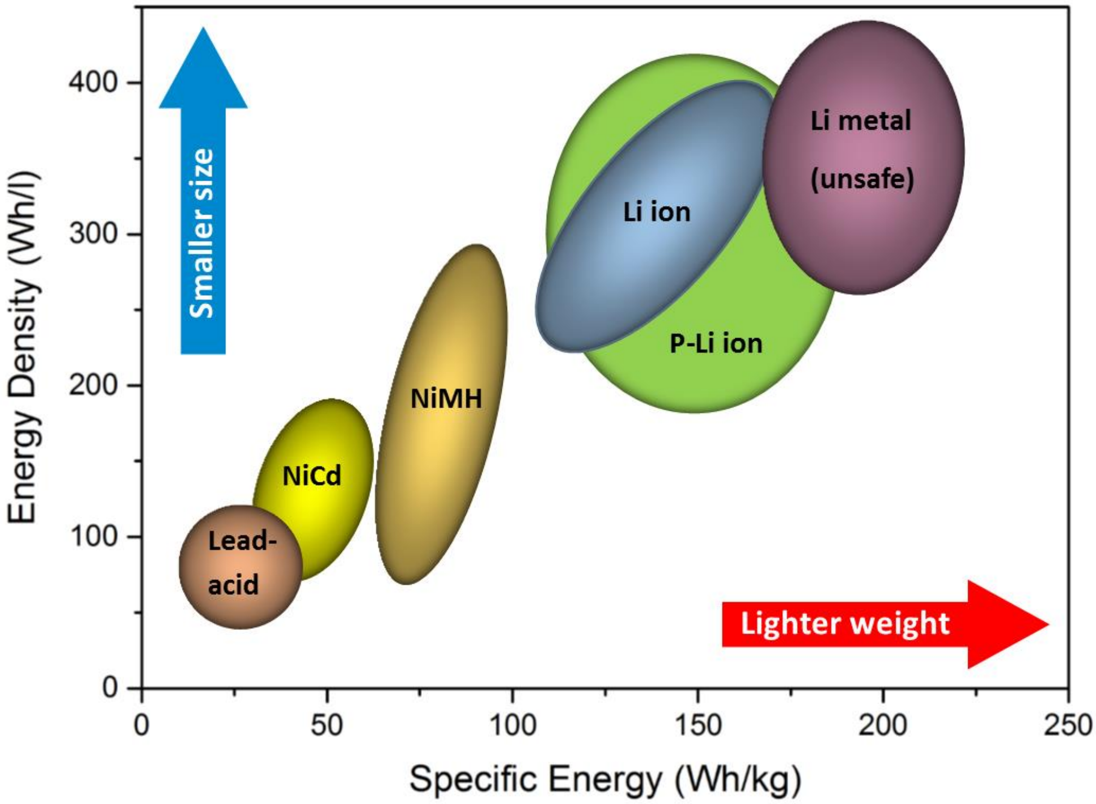

Figure 3 *- Comparison of energy densities of secondary batteries in terms of volumetric and gravimetric* [2,42].

2.1.3.1. Positive Electrodes

The term cathode is used for positive electrodes where the reduction occurs during discharging in the case of rechargeable batteries. The development of promising cathode materials for LIBs is critical because of the high cost of the actually available materials. The cost of cathode material is almost twice that of anode´s [43]. Beside low cost, the cells should also provide high energy density, high capacity, safety and improved efficiency. Modern cathode materials are generally prepared in the discharged state that is in the lithiated state.

The structure of the currently well-known cathode materials, typically determines the lithium diffusion pathways. They are classified into three major types; o*ne-dimensional* (the olivine type of $LiFePO_4$ (LFP), *two-dimensional* (the layered structures with a formula of $LiMO_2$ (M=Co, Ni, Mn etc.)) and *three-dimensional* (spinel type structures).

The spinels with a general sum formula of AB_2O_4, have three-dimensional channels for lithium diffusion as shown in ***Figure 4***. The well-known and most commonly used spinel type cathode material is $LiMn_2O_4$, which is one of the investigated materials in this work. This type of cathode material has low cost, excellent high rate performance due to its 3D framework and high energy density [44]. On the other hand, it has some shortcomings such as low discharge capacity and the dissolution of manganese during cycling [41]. These drawbacks can be partially suppressed by doping at the *16d* site (in $Fd\bar{3}m$) with elements such as Ni, Cr, Ti etc.

The spinel structure crystallizes with space group symmetry $Fd\bar{3}m$ in which lithium and metal $M^{3+/4+}$ such as Mn, Ti, V etc. ions are located at the *8a* tetrahedral and *16d* octahedral sites, $[Li]_{tet}[M_2]_{oct}O_4$, respectively with a cubic close-packed (ccp) oxygen sublattice. The oxygen ions are situated on a *32e* site. While the *16d* octahedral sites share edges with each other, the *8a* tetrahedral sites share faces with vacant *16c* octahedral sites.

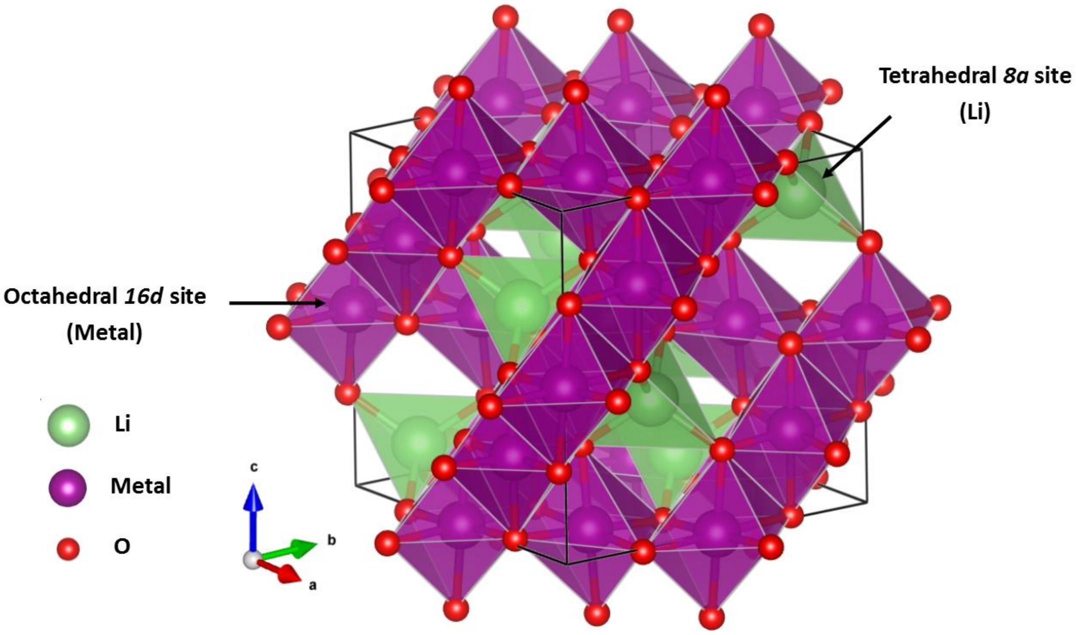

Figure 4 - *Crystal structure of spinel* LiM_2O_4 *(M=Mn, Ti and V etc.) in* $Fd\bar{3}m$ *space group.*

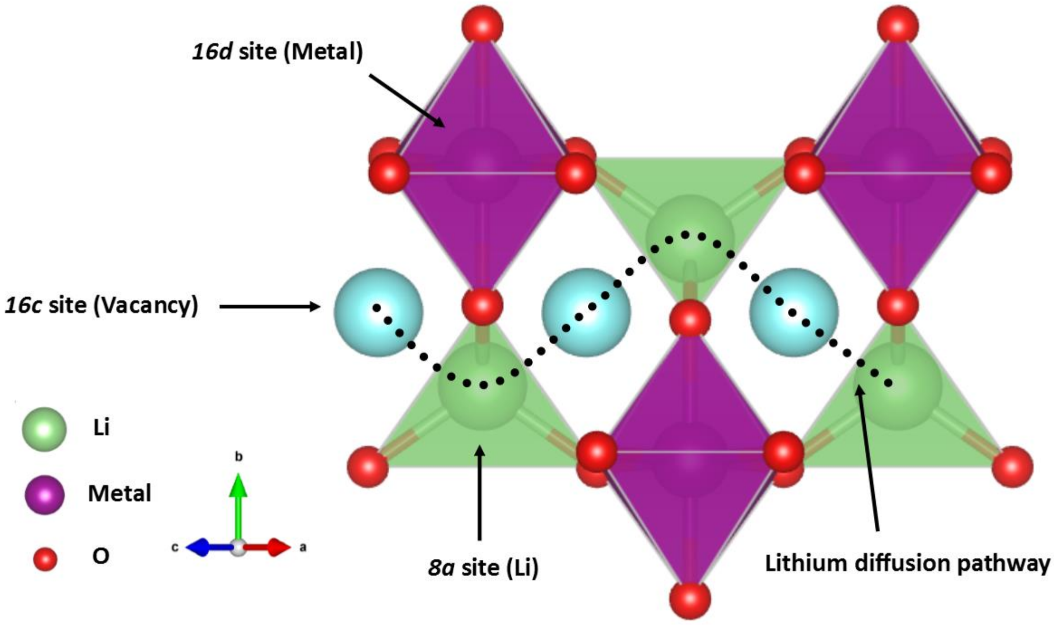

Figure 5 - *Lithium diffusion pathway in the spinel structure in projection along [101].*

Lithium ions move along a zigzag pathway (*8a-16c-8a-16c*) in three dimensions, which is energetically favourable in the structure (***Figure 5***). The 3D pathway yields rapid lithium diffusion in the three-dimensional structure during electrochemical cycling. In addition, the spinel structure has good electrical conductivity due to metal-metal interaction between the cations on the *16d* octahedral site [34].

The presence of Mn^{3+} ions in the $LiMn_2O_4$ structure causes a Jahn-Teller distortion that is a geometric distortion of a system. Jahn-Teller distortion reflects the interaction between electronic and structural degrees of freedom [45]. The Mn^{4+} ion has the d^3 configuration that is electronically degenerate and symmetric. However, the Mn^{3+} ion has high spin d^4 configuration, which is electronically non-degenerate. In this case, the orbitals are asymmetrically occupied and the energy in the system is reduced by distorting the environment.

2.1.3.2. Negative Electrodes

Anode materials for high performance LIBs should have a low potential so that high cell voltage can be obtained together with the cathode [30]. To improve cycle life, the crystal structure of the anode material should have no significant changes during Li^+ de/intercalation.

At the beginning of lithium battery development, lithium metal was used as an anode material. Lithium metal has a very low standard potential (-3.05 V vs. a standard hydrogen electrode (SHE)) [46], high specific capacity (3680 mAh/g) and low density (0.534 gcm^{-3}). However, lithium metal has some drawbacks such as safety problems as well as handling. Hydrogen can be produced when in contact with water (moisture), which makes it necessary to assemble cells in a dry room and take precautions against hydrogen gas explosions. Additionally, Li metal is prone to dendrite formation during cycling that can eventually penetrate into the separator and lead to short circuit of the cell. To overcome these problems, lithium metal is replaced by carbon based and non-carbon based materials (such as titanium containing materials ($Li_4Ti_5O_{12}$), alloying materials etc.).

2.1.3.2.1. Graphite

Currently, carbon based materials such as graphite or soft (graphitizable by calcination) /hard (non-graphitizable by calcination)) carbon are used as major anode materials. Graphite has a specific capacity of 372 mAh/g and high electronic conductivity. Additionally, the working voltage range of graphite *vs.* Li^+/Li is from 0 to 0.25 V. On the other hand, it shows low specific capacity, lithium metal plating on the surface which may occur especially at high charging current and low temperature, limited rate capability upon charge, the SEI (the solid electrolyte interphase) expansion, graphite exfoliation due to interaction of solvent, cracks, gas formation, SEI dissolution and volume expansion of ~10% [46–49].

2.1.3.2.2. Alloys

Besides commercially available graphite, numerous metals such as Ag, Al, Ge, Sb, Si, Sn, Zn etc. are able to electrochemically form alloys with lithium [30,34,42]. Some metals (Sn and Si) have a low potential and a high specific capacity similar to that of lithium metal. Characteristic properties of some metallic anode materials and graphite are tabulated in ***Table 3***. However, during electrochemical cycling the alloying of the metals causes a huge volume expansion/contraction, as shown in ***Figure 6***, which leads to cracks and pulverization of the electrode. In the end rapid capacity loss occurs due to loss of electric contact [17,23,46].

Table 3 - *Properties of anode materials* [30].

Anode	Theoretical capacity (mAh/g)	Practical Capacity (mAh/g)	Avg. Potential (V)
Li metal	3800	-	0
Graphite	372	360	0.1
Silicon	4200	1000	0.16
Tin	790	700	0.4

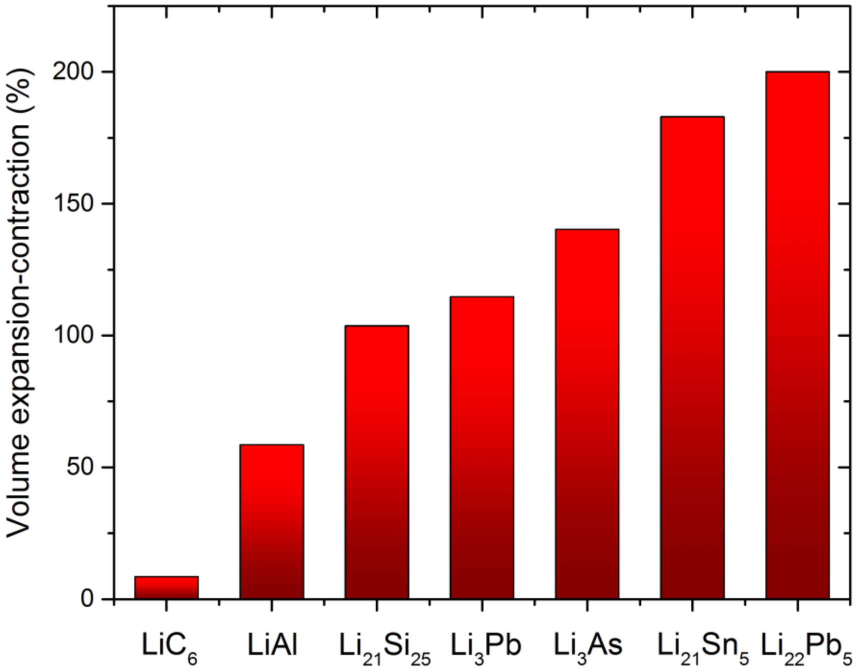

Figure 6 - *Volume expansion/contraction of metal alloys during cycling* [41].

Besides graphite as anode material, which has a specific capacity of 372 mAh/g and a volumetric capacity of 820 mAh/cm^3, Sn is one of the most attractive candidates that offers high capacity. Although Sn metal has a lower theoretical gravimetric capacity (790 mAh/g) than metallic lithium (3800 mAh/g) and Si (4200 mAh/g), the volumetric capacity of Sn (~2000 mAh/cm^3) is comparable to metallic lithium (~2000 mAh/cm^3) and Si (~2400 mAh/cm^3) [27,50]. Additionally, the working voltage of Sn and its alloys is between 0.6 V and 0.2 V. However, Sn metal has disadvantages such as pulverization and mechanical stress caused by the volume expansion and cracking of particles during cycling ***Figure 7***. The formation of cracks is directly proportional to the amount of lithium ions. In the following cycles, a solid electrolyte interface (SEI) layer with the decomposed electrolyte forms in the cracks and this results in a huge capacity loss [30] and eventually leads to capacity fading.

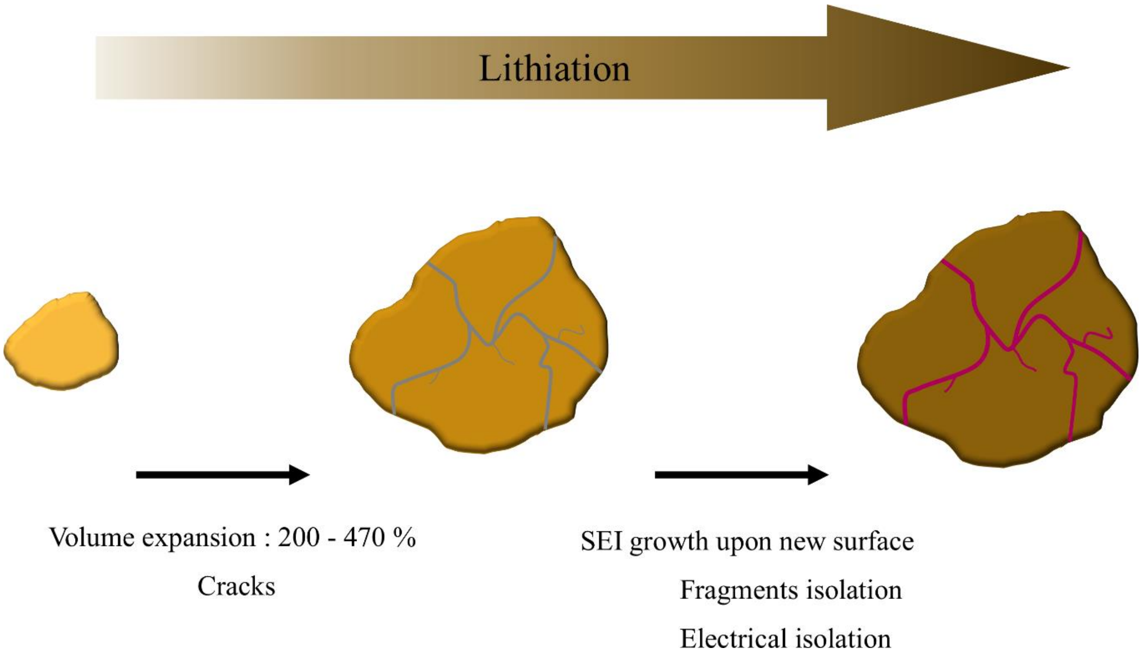

Figure 7 *- Illustration of volume expansion, cracks and SEI formation in metal particles.*

In order to suppress the excessive volume expansion of Sn based anode materials and to improve the electrochemical performance several methods can be used such as:

i. ***Reducing the particle size*** [28,29,51,52]

It is known that minimizing the particle size diminishes the mechanical stress caused by volume expansion/contraction during cycling. Recently, investigations show that below a critical particle size cracks do not occur [30]. Kim *et al.* showed that SnO_2 nanoparticles with an average size of 3 nm have negligible capacity fading after 60 cycles even at high charging rates [28].

ii. The use of active/inactive metal composites [28,30,53]

Electrochemically active Sn metals are well dispersed in the inactive Li_2O matrix and thereby the aggregation of Sn metals is hindered. However, Sn metals from delithiation of the Li-Sn alloy phase aggregate again with each other upon further cycling and this aggregation destructs the inactive Li_2O matrix [27].

iii. The use of ternary compounds [52–57]

In order to avoid the huge capacity loss from the irreversible reactions associated with the inactive Li_2O matrix in the first cycle, oxygen could be replaced with another metal such as Mo, B, Si, Al etc. or by using ternary compounds (SnM_xO_y). Even though the metal has better electronic conductivity compared to the Li_2O matrix, it reduces the mobility of lithium ions during cycling [30] and leads to a decrease of the rate capability. For that reason, the inactive Li_2O matrix is also necessary besides the metal. According to recent investigations, the best performance can be obtained using nanostructured materials together with ternary compounds.

Sn based anode materials offer much higher capacity (700-1491 mAh/g) [17–19,58,59] than commonly used graphite. The reaction of SnO_2 with Li during Li intercalation evolves in two steps [21–23,26]:

$$\mathrm{SnO_2 + 4Li^+ + 4e^- \rightarrow Sn + 2Li_2O} \tag{10}$$

$$\mathrm{Sn + 2Li_2O + xLi^+ +} xe^- \rightleftharpoons \mathrm{Li_xSn + 2Li_2O\ (0 \leq x \leq 4.4)} \tag{11}$$

The mainly irreversible reduction process of SnO_2 to metallic Sn is shown in Eq. (10) which causes an initial irreversible capacity loss due to the formation of an amorphous inactive Li_2O matrix [21,28]. Its theoretical capacity is 711 mAh g^{-1}. On the other hand, the second reaction (Eq. 11) is the mostly reversible alloying/dealloying process between metallic Sn and Li_xSn metal. This process corresponds to a theoretical capacity of 991 mAh g^{-1} which is more than the theoretical capacity of the currently used graphitic carbon. However, a large volume expansion of more than 200% occurs during the reversible alloying/dealloying process [22,23], causing huge internal stress. In the end, a capacity fading during cycling occurs due to the loss of electric contact [24–26]. Different approaches can be applied to overcome this problem as explained above. It has been reported that the electronic, optical, and electrochemical properties of SnO_2 can be tuned by Al doping [60–63] and it could also be shown that doping with Al restricts the grain growth during thermal treatment [64–67].

Sn-based anode materials ($Al_{0.57}Sn_{0.43}O_{1.71}$), which were synthesized at two different calcination temperatures (550°C and 40°C) is investigated in this work. The reaction mechanism of nanocrystalline $Al_{0.57}Sn_{0.43}O_{1.71}$ material is illustrated schematically in ***Figure 8***.

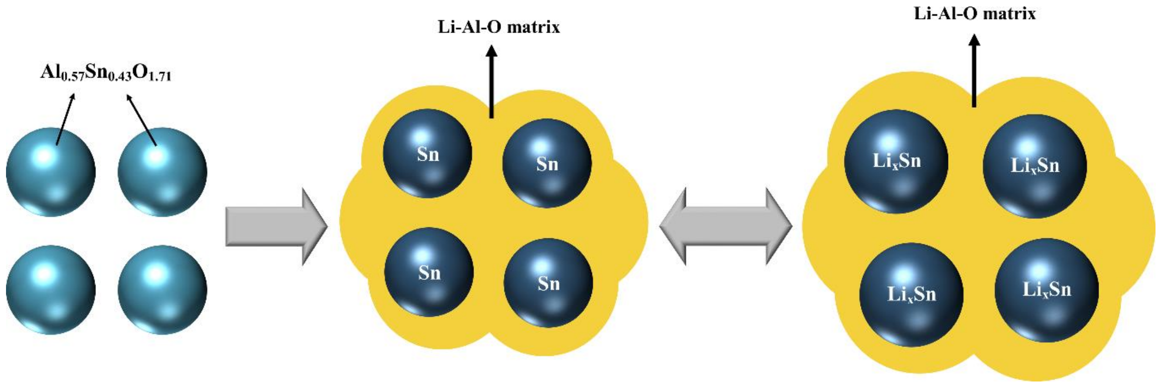

Figure 8 *– Schematic illustration of the $Al_{0.57}Sn_{0.43}O_{1.71}$ reaction with Li.*

2.2. Experimental Methods

2.2.1. Rietveld Method

In order to investigate the average structure of the material in reciprocal space, the Rietveld full-profile fitting method [7] was applied using the program package FullProf Suite [68]. The Rietveld method is a powerful technique for extracting the crystal structural information from X-ray and neutron powder diffraction data. The Rietveld method uses a least-squares approach, to minimise the weighted sum of the point-by-point differences squared in a powder diffraction pattern. The intensity is calculated using the experimental parameters such as instrumental parameters, background intensities, absorption, extinction etc. and the sample dependent parameters such as unit cell parameters, atomic fractional coordinates, atomic occupancy of each crystallographic site, Debye-Waller factors and background. Minimization is defined by an equation such as:

$$Minimization = \sum_{i=0}^{N-1} \left(w_i \left(Y_{obs_i} - Y_{calc_i} \right)^2 \right) \tag{12}$$

where w_i is the statistical weight and it is equal to $1/\sigma_i^2$ where σ_i^2 is the variance of the observed intensity and σ is the standard deviation. N is the total number of points of the pattern used in the refinement. Constraints can be applied to reduce the degree of freedom of the set of equations that has to be solved. The Rietveld method allows refining unit cell dimensions, atomic coordinates, profile parameters, atomic site occupancies, temperature factors and background parameters at once. The information of the entire powder pattern can be separated into four groups [10] shown in ***Table 4***:

***Table 4** - Information content of a powder pattern*

peak intensity $\left\|F_{hkl}\right\|^2$	structure factors, occupancy, temperature factor, atomic positions, texture, absorption and geometrical contributions (e.g. polarization)
peak position	lattice parameters, symmetry and instrumental contributions
background	diffuse scattering (e.g. local structure, amorphous fraction etc.), Compton scattering and scattering from sample container or air
peak shape	microstructural parameters (e.g. microstrain and crystallite size) and instrument profile

The quality of the Rietveld refinement is indicated by some residual functions, see below. The profile R-factor, which is the most straightforward discrepancy index, is a measure of the disagreement between the observed and calculated profile:

Profile Factor:

$$\mathrm{R_p}=100\frac{\sum_{\mathrm{i=0}}^{\mathrm{n-1}}\left|Y_{obs_i}-Y_{calc_i}\right|}{\sum_{i=0}^{n-1}Y_{obs_i}} \tag{13}$$

Weighted Profile Factor:

$$\mathrm{R_{wp}}=100\sqrt{\frac{\sum_{i=0}^{n-1}w_i\left|Y_{obs_i}-Y_{calc_i}\right|^2}{\sum_{i=0}^{n-1}w_iY_{obs_i}^2}} \tag{14}$$

The $\mathrm{R_{wp}}$ considers the statistical error associated with each point (the weighting scheme).

Expected Weighted
Profile Factor:

$$\mathrm{R_{exp}}=100\sqrt{\frac{N-P}{\sum_{i=0}^{n-1}w_iY_{obs_i}^2}} \tag{15}$$

The expected weighted profile factor gives the statistically best possible R_{wp} quantity using the number of data points, N and the number of refined parameters, P. The R_{exp} reflects the quality of the data (the counting statistics).

A good measure of the quality of the Rietveld refinement, so-called reduced chi-square, is the squared ratio between the weighted profile R-value and the expected R-value, which is given as:

Reduced chi-square
$$\chi^2 = \left[\frac{R_{wp}}{R_{exp}}\right]^2 = \frac{\sum_{i=0}^{n-1} w_i \left|Y_{obs_i} - Y_{calc_i}\right|^2}{N-P} \qquad (16)$$

In order to reduce the number of free parameters, constraints can be introduced into the refinement. In crystalline materials, groups of atoms, molecules or coordination polyhedra have a well-established structure and they are not completely independent [10]. Constraints apply on the coordinates of sites with specific local symmetries. A Rietveld refinement combined with restraints has a beneficial effect on the progress of the refinement. Examples of restraints are linear restraints (e.g. chemistry and crystallographic site occupancy), interatomic distances and angles. Using restraints, the refinement is stabilized, false minima are avoided and convergence is faster.

2.2.2. Pair Distribution Function

2.2.2.1. Theoretical Background

The Pair Distribution Function (PDF) gives the probability of finding an atom at a given distance r from another atom in real space [69]. It is a histogram of interatomic separations in a material [70] and it represents a weighted bond length distribution. The PDF, $G(r)$, is obtained via a sine Fourier transform of the total structure function, $S(Q)$, according to:

$$G(r) = 4\pi r[\rho(r) - \rho_0] = \frac{2}{\pi}\int_0^\infty Q[S(Q) - 1]\sin(Qr)dQ \qquad (17)$$

where ‘r’ is the distance between two atoms and Q is the magnitude of the scattering vector, $Q=|k-k_0|$. For elastic scattering, $Q=4\pi sin\theta/\lambda=2\pi/d$, where 2θ is the scattering angle and λ is the wavelength of the scattering radiation. ρ_0 is the average number density of scatterers (number of atoms in symmetrized unit cell per unit cell volume), $\rho(r)$ is the pair density function (Eq. 18), f_i and f_j are the scattering factors for atoms i and j and $<f>^2$ is the square of the average of the atomic form factors in the sample. In the case of X-rays, it becomes very small at high-Q [8,71].

$$\rho(r) = \frac{1}{4\pi r^2}\sum_i\sum_j \frac{f_i f_j}{\langle f\rangle^2}\delta(r - r_{ij}) \qquad (18)$$

The PDF can be calculated straightforwardly;

$$G(r) = \frac{1}{r}\sum_i\sum_j \frac{f_i f_j}{\langle f\rangle^2}\delta(r - r_{ij}) - 4\pi\rho_0 \qquad (19)$$

The sum goes over all pairs of *i*th and *j*th atoms in the sample separated by r_{ij}, δ is the delta distribution.

The PDF is a sine Fourier transform of *S(Q)* of the measured intensity and takes both, Bragg and diffuse scattering into account. The Bragg scattering contribution can be analysed by the conventional Rietveld approach with high degree of accuracy in reciprocal space and provides information on the average and periodic structure regarding long-range order. The diffuse scattering which lies between and beneath the Bragg reflections yields information regarding the short range order and, therefore, local deviations from the average structure [72]. It has weaker intensities compared to Bragg reflections and dominates at higher scattering angles where the Bragg reflections are weak due to the Debye-Waller factor. In conventional Rietveld refinements, the diffuse scattering contribution is usually discarded.

The coherently scattered intensity from a sample is given by the Debye Equation [73,74]:

$$I^{coh}(\vec{Q}) = \sum_{i,j}^{N} f_i(|\vec{Q}|) f_j(|\vec{Q}|) e^{i\vec{Q}(\vec{r}_i - \vec{r}_j)} \qquad (20)$$

which gives,

$$I^{coh}(\vec{Q}) = N\langle f^2(|\vec{Q}|)\rangle + \sum_{i \neq j}^{N} f_i(|\vec{Q}|) f_j(|\vec{Q}|) e^{i\vec{Q}(\vec{r}_i - \vec{r}_j)} \qquad (21)$$

where *N* is the total number of atoms and *f* is the *Q*-dependent X-ray scattering factor. The coherently scattered intensity can be written from *Equation* (20).

$$\frac{I^{coh}(\vec{Q})}{N\langle f(|\vec{Q}|)\rangle^2} - \frac{\langle f^2(|\vec{Q}|)\rangle}{\langle f(|\vec{Q}|)\rangle^2} = \frac{1}{N\langle f(|\vec{Q}|)\rangle^2} \sum_{i \neq j}^{N} f_i(|\vec{Q}|) f_j(|\vec{Q}|) e^{i\vec{Q}(\vec{r}_i - \vec{r}_j)} \qquad (22)$$

S(Q)-1 can be defined in *Equation* (22). To obtain *S(Q)-1*; the self-scattering $\langle f^2 \overrightarrow{|Q|} \rangle$ which has no atom-pair correlation information is subtracted [75]. Finally, *S(Q)* can be written in terms of the coherently scattered intensity that has only structure dependent information. After ignoring the total number of atoms, N, as a result the equation below is obtained:

$$S(\vec{Q}) = \frac{I(\vec{Q}) - \langle f^2 \rangle + \langle f \rangle^2}{\langle f \rangle^2} = 1 + \frac{1}{N\langle f \rangle^2} \sum_{i \neq j}^{N} f_i f_j e^{i\vec{Q}(\vec{r}_i - \vec{r}_j)} \tag{23}$$

where $-\langle f^2 \rangle + \langle f \rangle^2$ is the so-called Laue monotonic diffuse scattering which is coming from the mixture or different chemical species in a sample. Using $e^{i\vec{Q}(\vec{r}_i - \vec{r}_j)} \approx sinQr/Qr$, *S(Q)* can be rewritten as Equation (24). Note that in a macroscopically isotropic sample, $\vec{r}_i - \vec{r}_j$ takes all orientations in space with equal probability.

$$S(\vec{Q}) = 1 + \frac{1}{N\langle f \rangle^2} \sum_{i \neq j}^{N} f_i f_j \frac{sin(\vec{Q}.\vec{r})}{\vec{Q}.\vec{r}} \tag{24}$$

The total structure function, *S(Q)*, oscillates around 1 as $Q \to \infty$. The coherently diffracted intensity in *S(Q)* dies out with increasing Q due to the Debye-Waller factor [76]. For a single element system, $\langle f^2 \rangle$ is equal to $\langle f \rangle^2$ in Equation (23) and as a result $I(\vec{Q}) = \langle f \rangle^2$ at high Q-values. *S(Q)* oscillates around $\langle f \rangle^2$ at low Q-values and it approaches 1 at high Q-values.

F(Q) is known as the reduced total scattering structure function and defined in terms of *S(Q)* in Equation (25) as:

$$F(Q) = Q[S(Q) - 1] \tag{25}$$

F(Q) oscillates around zero when Q goes to high Q-values. Diffuse scattering can be seen more clearly in *F(Q)* than in *S(Q)*.

G(r) is called the pair distribution function and it is a one-dimensional function oscillating around zero. Positive peaks in *G(r)* show the probability of finding interatomic distances where microscopic pair density exceeds the average number density ($\rho(r)>\rho_0$). On the other hand, negative peaks correspond to a real space vector not having atoms where a microscopic pair density is lower than average ($\rho(r)<\rho_0$). In the case of neutron diffraction, positive peaks correspond to two nuclei with either both negative or both positive scattering length, while negative peaks correspond to pairs with one negative and one positive scattering length of the nucleus.

The pair distribution function is a weighted sum of N(N+1)/2 partial PDFs that describe the pair correlations between certain elements in the material, where N is the number of elements [77,78]. Note that "+" in this formula describes the self-correlations between the atoms of the same type. The weighting factors w_{ij} depend on the respective atomic concentration and atomic form factors of each element [78] (*Eq.* 26). Here the weights for x-rays are constant over all Q-values and they are calculated as f(Q=0).

$$w_{ij} = c_i c_j f_i(Q) f_j(Q) / \sum |c_i f_i(Q)|^2 \qquad (26)$$

2.2.2.2. Requirements for High Quality Total Scattering Data

The PDF method requires mainly high maximum momentum transfer, Q_{max} (for good resolution in real space), high Q-resolution (for a broad extension in real space), good counting statistics at high Q-values, low and subtractable background scattering. The PDF method carries no less information than Rietveld method.

Effect of Q_{max} value

The main difference from an experimental point of view between data for conventional Rietveld refinements and PDF is the necessity to measure to as large Q-values as possible for PDF. The real space resolution of the PDF is given by $\delta r \approx \pi/Q_{max}$ and directly related to the maximum Q-value, Q_{max} [79] and the real space resolution gets better with increasing the Q_{max} value.

In practice, the data cannot be measured up to infinite momentum transfer, Q, the accessible maximum Q is limited. Hence, the finite Q-range of the data introduces errors into the experimental PDF, known as *termination ripples*. The termination ripples are spurious oscillations at small r-values, typically lower than reasonable nearest neighbour distances and vanish at increasing r. In practical applications, the Fourier sine transform of *F(Q)* does not go from zero to infinite, but from minimum to maximum Q-values [9]). The termination ripples can be described by convoluting the *G(r)* with a step function cutting at Q_{max}. The sinc(r) step function is given by:

$$S(r) = \sin(Q_{max}.\mathrm{r})/\mathrm{r} \qquad (27)$$

The termination ripples oscillate with a wavelength $\sim 2\pi/Q_{max}$ in *G(r)* and the wavelength of the ripples increases with decreasing Q_{max} [8]. On the other hand, the convolution of *G(r)* with *S(r)* results in a Gaussian like peak broadening. However, thermal motion of atoms always broadens the PDF and the additional broadening due to termination is negligible if a high enough Q-value is chosen. If Q_{max} is larger than 30 Å^{-1}, termination produces minimal errors [80].

To compare the expected PDF for different instruments simulations with a standard reference material were performed. Results are shown in ***Figure 9***. The maximum Q attainable is 6.28 Å^{-1} and 7.30 Å^{-1} (at 2θ=127°) using laboratory diffractometers with Co-Kα_1 and Cu-Kα_1 radiation, respectively. However, PDF analysis cannot be applied using these diffractometers due to the limited real space resolution and the termination ripples with long wavelength. In order to obtain high Q_{max}, the use of laboratory sources with short wavelength (high-energy) such as Mo-Kα_1 (Q_{max}=15.85 Å^{-1}) or Ag-Kα_1 (Q_{max}=20.11 Å^{-1}) radiations are necessary together with a maximum scattering angle (2θ) near 127° which can usually be achieved. The real space resolution and the termination ripples of PDFs from Mo and Ag sources are reasonable and these sources are suitable for PDF analysis. However, high energy X-ray synchrotron radiation is always preferred for accurate PDF measurements with short acquisition time and good statistics which affect the Q_{max} and with highest real space resolution. PDFs of LaB$_6$ are modelled for different X-ray sources considering only Q_{max}, high-energy beamlines MSPD (the energy of 30 keV) at ALBA, Barcelona and P0.2.1, HRPD (the energy of 60 keV) at Petra III, Hamburg (***Figure 9***).

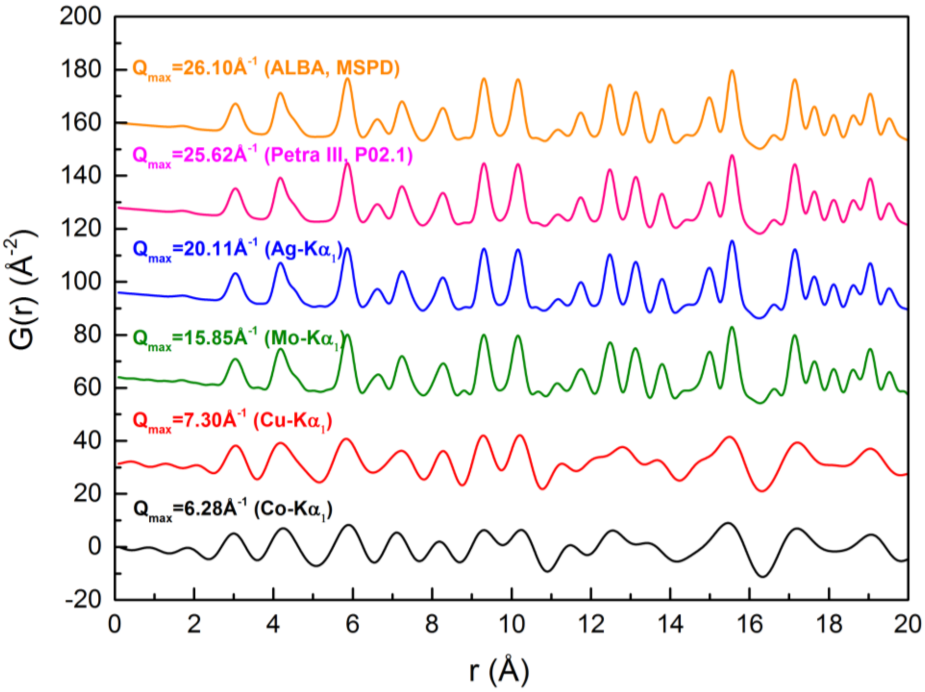

Figure 9 *- Simulated PDFs of* LaB_6 *for different finite Q ranges.*

Effect of Q resolution

The finite angular or Q resolution of the measurement leads to a decrease in the amplitude of the PDF peaks with increasing ‘r’. High resolution data can be obtained even at high Q-values using X-ray scattering [9,76]. In a crystal with perfect structural coherence, PDF peaks extend to infinity with a constant envelope of the amplitude. But in practice, the amplitude of PDF peaks attenuates more rapidly due to the finite Q resolution of the measurement [8]. This is the limitation on the spatial coherence of the measurement. The envelope of the peak attenuation due to the finite Q resolution follows a Gaussian shape and this envelope is characteristic for each experimental setup. The Gaussian envelope is described by:

$$B(r) = exp\left(-\frac{(rQ_{damp})^2}{2}\right) \tag{28}$$

where Q_{damp} is the dampening parameter which is characteristic for each experimental setup. Q_{damp} can be determined by measuring a material of high crystallinity and crystallite size giving the maximum range of coherently diffracting regions. In order to obtain the PDF peaks over a large r-distance, it is important to use a high Q-resolution, so that structural correlations can be detected up to high Q-values. Beyond the instrument envelope, no structural information can be detected. The maximum range in real space where structural information can be gathered is defined by [8],

$$r_{max} \leq \frac{\pi}{\Delta Q} \tag{29}$$

In the section of 3.3.1, Q_{damp} values were obtained for a Stoe Mo diffractometer and beamlines P02.1 at Petra III and MSPD at ALBA.

Effect of Counting Statistics

The Debye-Waller factor reduces the intensities of Bragg peaks, thereby, at high Q-values the scattering is predominantly diffuse scattering and the signal to noise ratio is poor. Therefore, it is mandatory to measure with very good counting statistics especially at high Q-values. The PDF peak broadening due to counting statistics is given by [80],

$$\sigma^2_{\rho(r)} \approx (8\pi^4 r^2)^{-1} \sum [Q_i^2 / N_{tot}(Q_i)][\Delta Q_i]^2 \tag{30}$$

where $N_{tot}(Q_i)$ is the total number of counts collected in each region of Q. Good statistics can be obtained with increasing counting time at high angles. Insufficient counting time in particular at high Q-values, will produce unwanted noise in the PDF.

Effect of Other Contributions

To measure accurate total scattering data low backgrounds, stable detectors and detector electronics during the experiment are necessary. Total scattering data include extrinsic contributions, such as the sample container, air scattering or necessary admixtures to the sample in addition to the scattering from the sample itself, so that it is important to measure all these contributions and to subtract them from the total scattering data, if possible.

2.2.2.3. Structural Information from the PDF

Structural information can be extracted from the peak position, intensity, width and peak attenuation of the PDF. The *peak position* in the PDF gives directly the bond length, which represents the average separation of the pairs of atoms in real space. The bond lengths can be obtained up to diminishing amplitude of the PDF due to limited structural coherence in the sample or due to restricted Q resolution. The *integrated intensity* of a PDF peak yields information regarding the coordination number. The coordination numbers can be calculated from the radial distribution function, RDF, R(r), which is;

$$R(r) = 4\pi r^2 \rho(r) \tag{31}$$

and the coordination number is given by;

$$N_C = \int_{r_1}^{r_2} R(r)dr \tag{32}$$

where r_1 and r_2 define the RDF peak that corresponds to the coordination shell [8].

The PDF *peak width* gives information about the static and dynamic disorder in the atom pairs. The *peak attenuation* of the PDF reveals the length of the structural coherence, if all PDF peaks from the structure are within the instrumental envelope.

Chapter 3 - EXPERIMENTAL

3.1. Electrochemistry

In order to perform electrochemical experiments, a VMP (Perkin Elmer Instruments, USA) multichannel potentiostat controlled by computer with the program EC-Lab was used. Furthermore, Galvanostatic Cycling with Potential Limitation (GCPL) was used for the electrochemical cycling process. In this technique, there is a potential limitation between working and counter electrodes and the changes of potential between these limited values with time are recorded by applying constant current.

3.2. Diffraction Experiments

Powder X-ray diffraction experiments were performed on a STOE STADI/P laboratory powder diffractometer (Mo-Kα_1 radiation), at the high-resolution powder diffraction beamline (P02.1) at PETRA-III, DESY and at the Materials Science and Powder Diffraction Beamline (MSPD) at ALBA.

3.2.1. Laboratory Diffractometer

The STOE STADI/P powder diffractometer (***Figure 10***) has a curved Ge 111 monochromator yielding pure Kα_1 radiation and the Dectris MYTHEN 1K detector. The molybdenum tube gives relatively good flux and its Kα_1 emission energy is 17.5 keV (λ=0.7093Å). The maximum accessible scattering angle (2θ) is about 127^o in Debye-Scherrer mode and the Q_{max} is 15.85 Å^{-1}. Using this Mo diffractometer acceptable low resolution PDFs can be obtained. The 1D diffraction patterns of samples in a 0.5 mm capillary were recorded on a Dectris MYTHEN 1K detector, which is located at a distance of 180 mm from the sample center. The MYTHEN 1K detector has a low background without dark current resulting in an excellent signal-to-background ratio. To get adequate statistics at higher Q-values, PDF data were collected over an angular range of 1° to 127.89° in 2θ with the position sensitive detector (PSD) step of 0.45° and 40 s per each step for a single range and 8 ranges were measured in total (~25 h).

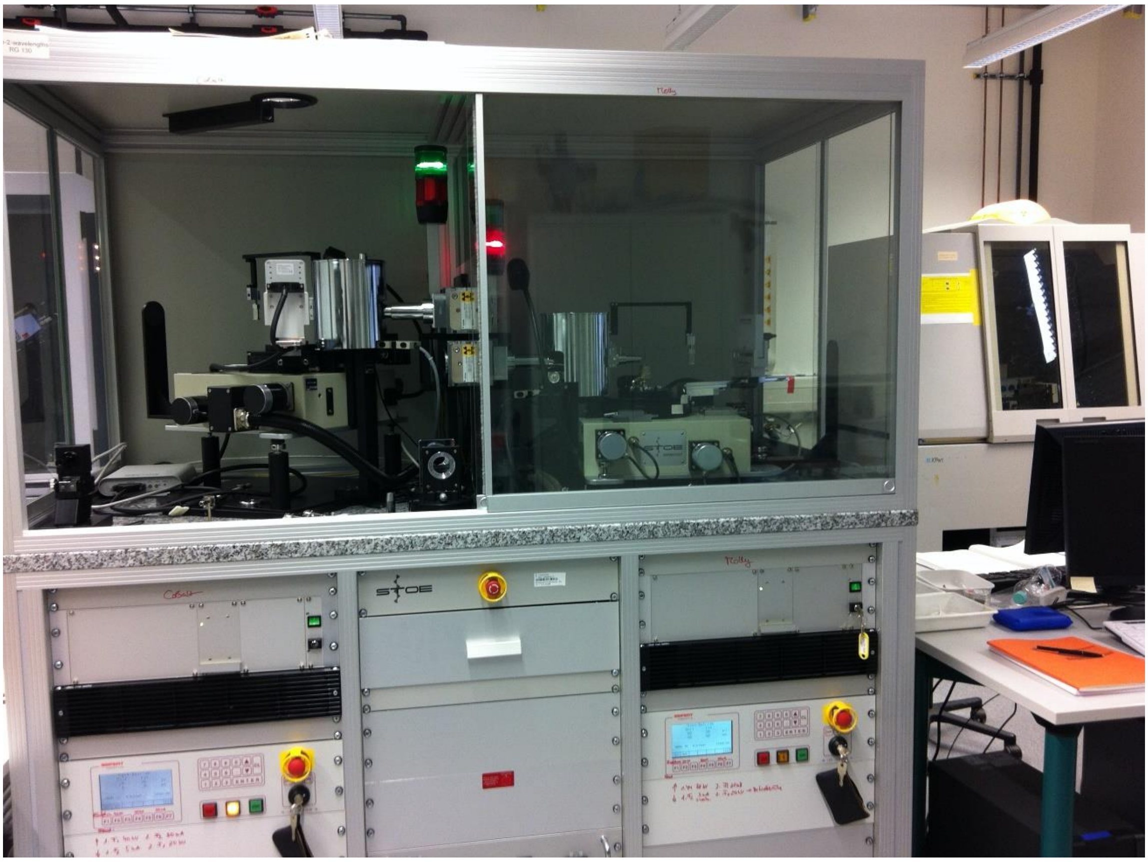

Figure 10 *- Photograph of the Mo diffractometer.*

3.2.2. Material Science and Powder Diffraction Beamline

The ALBA-CELLS synchrotron in Barcelona is the most recent synchrotron source in Europe. The machine consists of a 268 m circumference storage ring and the electrons are accelerated to 3 GeV (***Figure 11***).

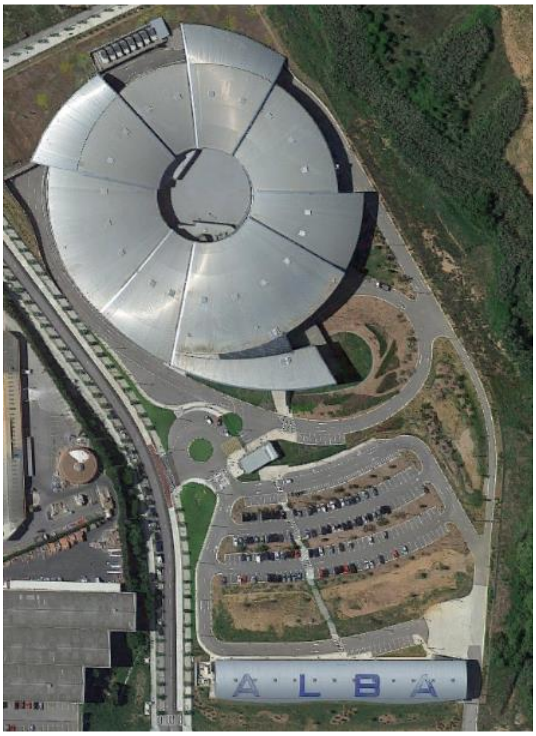

***Figure 11** – Aerial view of the ALBA synchrotron.*

The MSPD beamline has a superconducting wiggler as an insertion device and it operates at energies between 8 and 50 keV. The brilliance of MSPD at the energy of 30 keV is 1 x 10^{14} ph/s/0.1%bw within a 300 x 125 μrad^2 aperture [81]. All technical properties of the beamline are given in ***Table 5*** and an overview of the beamline is shown in ***Figure 12***.

Table 5 *- Technical Specifications of MSPD beamline.*

Photon energy range	8 – 50 keV
Flux at sample	~ 4 x 10^{12} ph/s
Photon source size (FWHM)	0.65 x 0.1 mm^2 (HxV)
Photon source divergence (FWHM)	14 x 0.18 $mrad^2$ (HxV)
Monochromator type	Si (111) double crystal with long 2nd crystal
Insertion device	Superconducting Wiggler SCW31

The MSPD beamline is equipped with a Mythen 1D position sensitive detector with 6 modules and a MAD26 high resolution detector for powder diffraction, however, for PDF and high resolution diffraction measurements the Mythen detector was used. The Mythen detector is a silicon microstrip detector and covers a solid angle of 40° in 2θ. It provides an angular resolution of 0.006° and a Q_{max} of about 26 $Å^{-1}$ at an energy of 30 keV. Besides, the detector has some extra advantages in comparison to other commonly used detectors (image plate detectors) for PDF measurements. For instance, the fluorescence signal can be discriminated in the total scattering data during measurement by changing the threshold energy of the detector. In this case during PDF data reduction the correction for fluorescence contributions is not necessary. Additionally, Compton scattering contribution to the total scattering data can be excluded by a selection of the appropriate threshold energy of the detector [82].. Consequently, these advantages improve the quality of the PDF.

High resolution XRD and PDF measurements were conducted using the energy of 30 keV and a total exposure time of 200 s. The sample to detector distance was 550 mm and the beam size was 3x1 mm^2 (HxV).

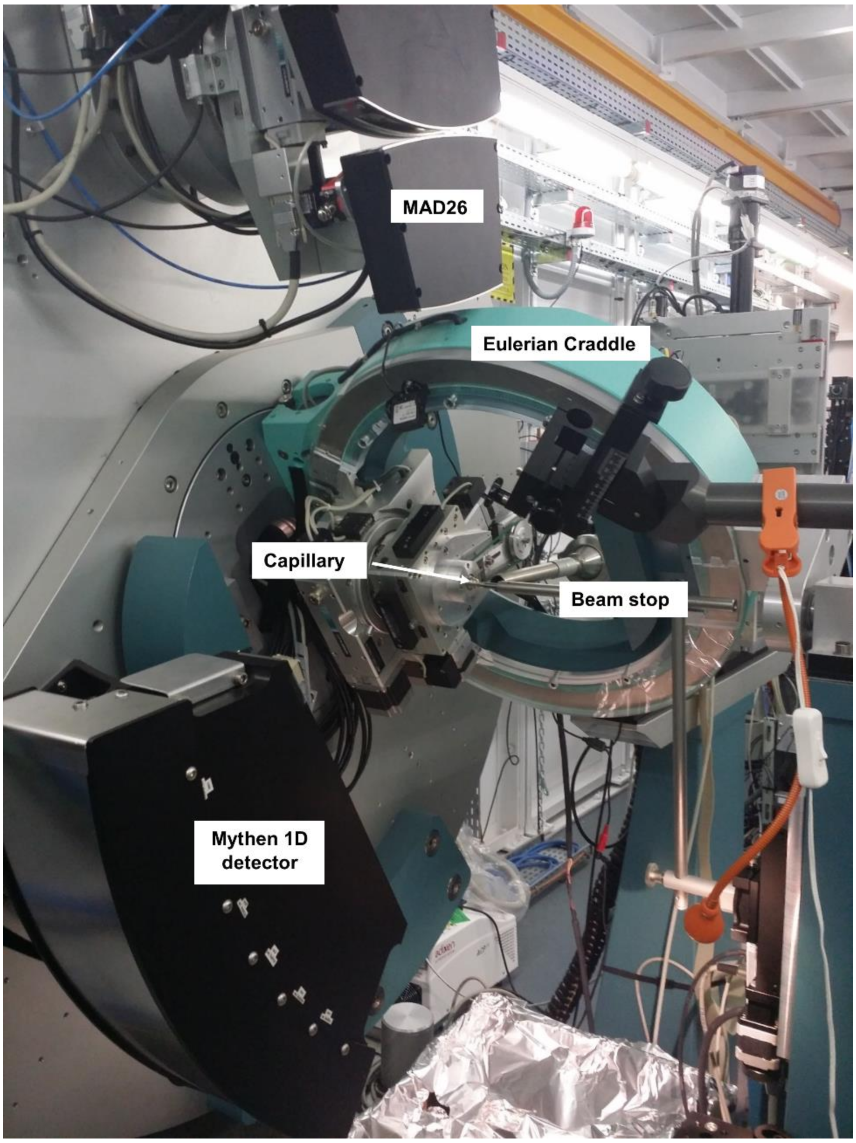

Figure 12 *– Photograph of the MSPD beamline at ALBA with MYTHEN 1D and MAD 26 Detector.*

3.2.3. High Resolution Powder Diffraction Beamline (HRPD, P02.1)

PETRA III is the 3rd generation synchrotron radiation source at DESY. It is the biggest and most brilliant storage ring in the world and has a circumference of 2.3 km. The electron energy is 6 GeV with a beam current of 100 mA.

The high resolution powder diffraction beamline P02.1 has an undulator which creates a small source with a very low divergence and high flux. The energy at the experimental station is fixed to 60 keV which yields negligible polarization effects and very low mass absorption coefficients for most elements [83].

Table 6 *- Technical Specifications of P02.1 beamline.*

Photon energy	60 keV
Flux at sample	~5 x 10^{10} ph/s
Photon source size (FWHM)	140 x 5.6 μm^2 (HxV)
Photon source divergence (FWHM)	7.9 x 4.1 μrad^2 (HxV)
Monochromator type	Double Laue monochromator with diamond (111) and Si (111) crystals
Insertion device	Undulator U23

High resolution XRD and total scattering data were collected on a 16-inch two-dimensional amorphous silicon (a-Si) flat panel detector XRD 1621 N ES (Perkin Elmer) with 2048x2048 pixels and 200x200 μm pixel size. Due to its fast read-out rates (133.2 ms), the detector is suitable for *in situ / ex situ* XRD and PDF measurements providing good statistics. The use of a two-dimensional flat panel detector for PDF analysis has been demonstrated by Chupas *et al.* [84]. The detector was mounted orthogonal to the incident beam with variable sample-to-detector distance (SDD). The data can be collected with high angular resolution at large SDD and with high momentum transfer at short SDD. The accessible Q_{max} is about 30 Å^{-1} when the detector is at SDD of 200 mm. During measurements, the beam size was set to 0.75x0.5 mm^2 (HxV).

The samples were filled in borosilicate capillaries of 0.5 mm and mounted perpendicular to the beam on a rotary holder without capillary spinning. An empty capillary of borosilicate type was measured for background corrections. A LaB_6 standard material (NIST SRM 660b) was measured at similar conditions for characterising the experimental configuration. The capillaries were mounted between adhesive PE foils in the rotary holder shown in ***Figure 13***. This holder is usually used for *in situ* experiments and described in previous papers [83,85].

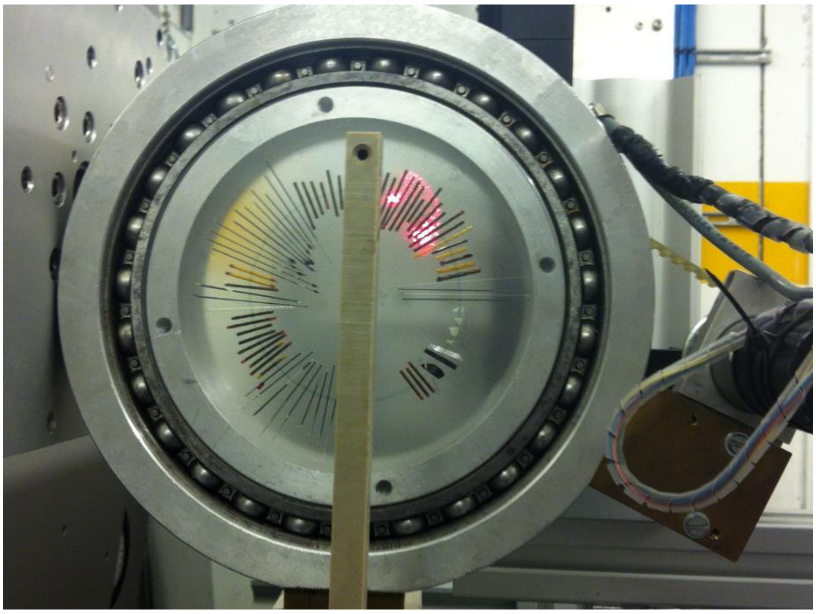

Figure 13 *- Capillaries in rotary-sample holder and with beam stop.*

3.2.3.1. *In situ* Electrochemical Experiment

In situ characterization methods allow obtaining maximum information about a variety of chemical and physical processes in a material during operation of the device. *In situ* measurements can directly link the structural response of the electrode on electrochemical charging and discharging. *In situ* investigations are of crucial importance to elucidate the processes during charging and discharging, because *ex situ* studies can give unsatisfying or even misleading information due to relaxation phenomena. In Li-ion batteries, during Li extraction or Li insertion, information such as phase transitions, lattice parameter evolution, micro strain, crystallite size, atomic positions and changes in occupation number can be obtained. The *in situ* cell as described by our colleagues was used [83]. The cell was held by a multi-cell holder with automated sample exchange between four individual cells.

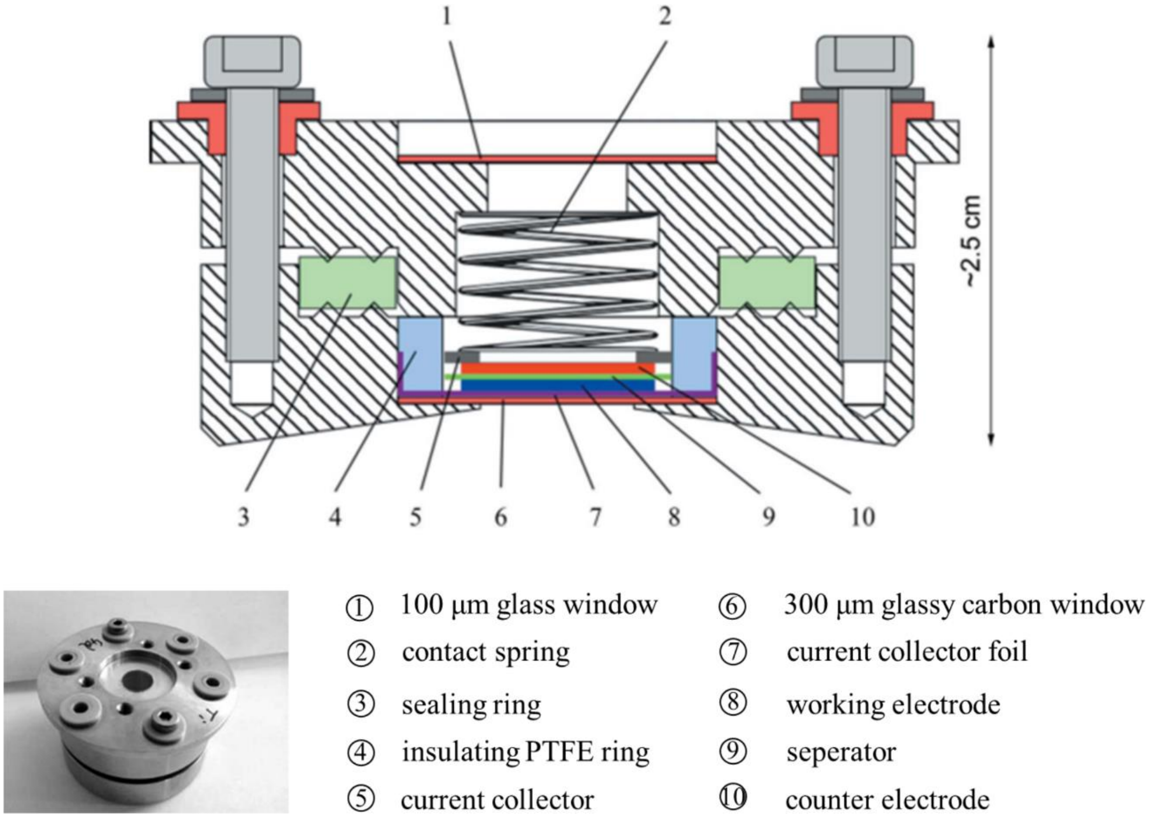

Figure 14 *- Overview of in situ cell for PDF experiments* [83].

The *in situ* cell is made of stainless steel, consists of windows, spring, current collector, working electrode, separator and counter electrode. The windows can be of different materials as glass or glassy carbon depending on the specific requirement. They´re fixed with a high-density polyethylene foil to the steel casing by a heat treatment at 180ºC. Lithium metal as a counter electrode and Whatman GF/D 2.7 µm as a separator were used. The electrical cables for both anode and cathode were contacted by screws. Galvanostatic cycling of the cell was performed with a VMP3 potentiostat (Bio-Logic, France).

3.3. Determination of Instrument Parameters

In this section three experimental setups (Alba-MSPD, Petra III-P02.1, Mo-$K_{\alpha1}$ laboratory diffractometer) were investigated to understand the effects of the instrumental configuration on the average and local structure studies.

3.3.1. Resolution of the Setups

The angular resolution of a setup plays an important role in getting accurate structure and microstructure information such as strain and apparent size. Gaussian (U, V, and W) and Lorentzian (X and Y) parameters as defined in the FullProf programme for the reflection profiles and instrument resolution function in the Rietveld refinement were determined by measuring LaB_6 (NIST 660d standard reference material). The Gaussian and Lorentzian components of full width at half maximum are described as [86–88]:

$$\mathrm{FWHM}_G^2 = U\tan^2\theta + V\tan\theta + W \tag{33}$$

$$\mathrm{FWHM}_L^2 = X\tan\theta + \frac{Y}{\cos\theta} \tag{34}$$

The instrumental angular resolution function for the different setups is shown in Figure 15. The MSPD beamline has the best angular resolution in comparison to the Mo $K_{\alpha1}$ laboratory diffractometer and the P02.1 beamline with an area detector (for SDD of 400 mm) for total scattering experiments. The data can be used to analyse the average structure with high angular resolution in a Rietveld refinement as well as in a real space PDF refinement. In fact, the P02.1 beamline with an area detector at 1600 mm has as good angular resolution as the MSPD beamline. However, the data can not be used for PDF analysis due to the limited Q-range. The Mo $K_{\alpha1}$ diffractometer can be used also for PDF analysis to some extent, but it suffers from long measuring time (~1 day) and low Q_{max}. At beamline P02.1, the angular resolution can be traded against the maximum angular range (at short SDD) by variation of the sample-to-detector distance on a motor-driven track system. High angular resolution is available at long SDD corresponding to a very limited available angular range, which again leads to a low real space resolution in the total scattering measurement. While during *ex situ* measurements the detector position can be changed between long and short SDD quickly (in ~5 min) and reproducibly, thereby adapting necessary resolution and range, this is no real option for *in situ* measurements since it causes a loss of data during changing between the different positions and some inconsistencies because combining data from different due to proceeding reactions during the time needed for this change.

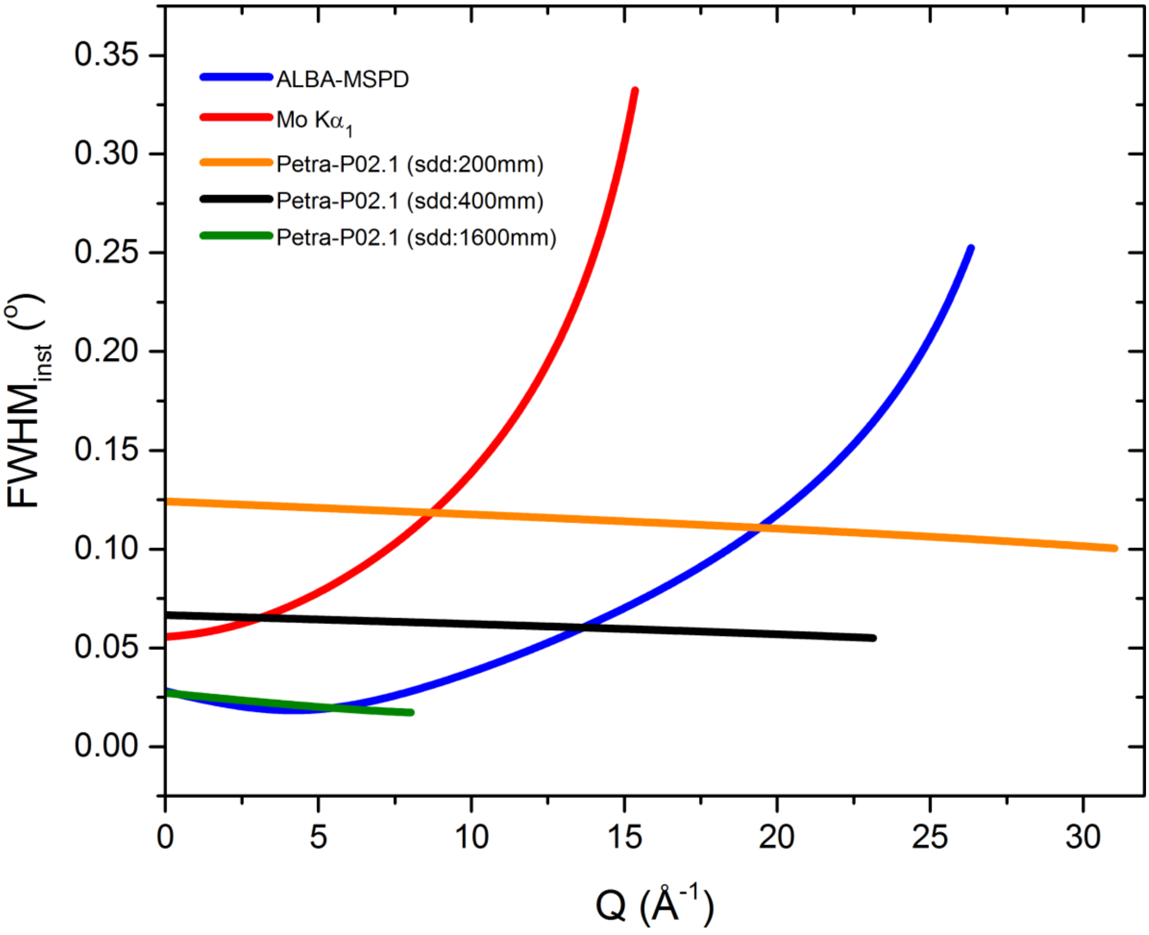

***Figure 15** – FWHM of the instrumental function of setups. The end of the respective curves also indicates the maximum available Q-range.*

The biggest advantage of the P02.1 beamline is the short exposure time with high momentum transfer at a short SDD. Its maximum usable Q_{max} is 30 Å^{-1}. The characteristics of the different setups are tabulated in ***Table 7***. High real space and angular resolution can be obtained at the MSPD beamline with a reasonable exposure time simultaneously. Note that the accessible Q_{max} is the upper limit of the instrument. However, the usable Q_{max} is an upper bound for a reliable signal from the structure in the data that does not include any noise coming from outer part of detector.

Table 7 *– Comparison between different setups for PDF measurements.*

	P02.1 (at 200 mm)	**MSPD**	**Mo K$_{\alpha 1}$**
Energy (keV)	60	30	17.5
Wavelength (Å)	0.2072	0.4133	0.7093
Detector type	2D flat panel	Mythen 6K	Mythen 1K
Accessible Q_{max} (Å^{-1})	31	27	15.85
Usable Q_{max} (Å^{-1})	30	25	~15
Real space resolution, $\Delta r \approx \pi / Q_{max}$ (Å)	0.1009	0.1193	0.1977
Angular resolution, FWHM (°)	0.0666	0.0281	0.0556
Typical exposure time for PDF	1 min	8 min	1 day

The dampening factor Q_{damp}, which is characteristic for each experimental setup, is determined by fitting envelope (Eq. 28) of the PDF peaks of an ideal crystalline material using a least-squares refinement. The dampening factors (Q_{damp}) in the PDF of LaB_6 for different setups were determined using the Gaussian envelope function (Eq. 28) as shown in ***Figure 16***, ***Figure 17*** and ***Figure 18***.

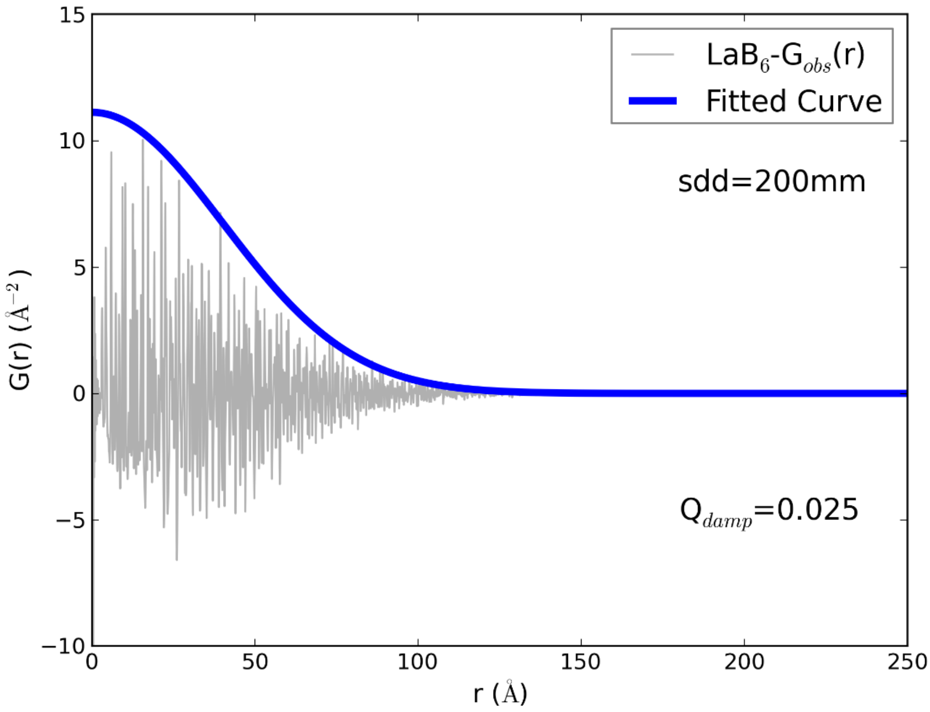

Figure 16 - *Gaussian damping envelope of LaB_6 PDF data obtained at P02.1 beamline at Petra III (SDD:200 mm). Blue line shows experimental envelope curve according to equation 28.*

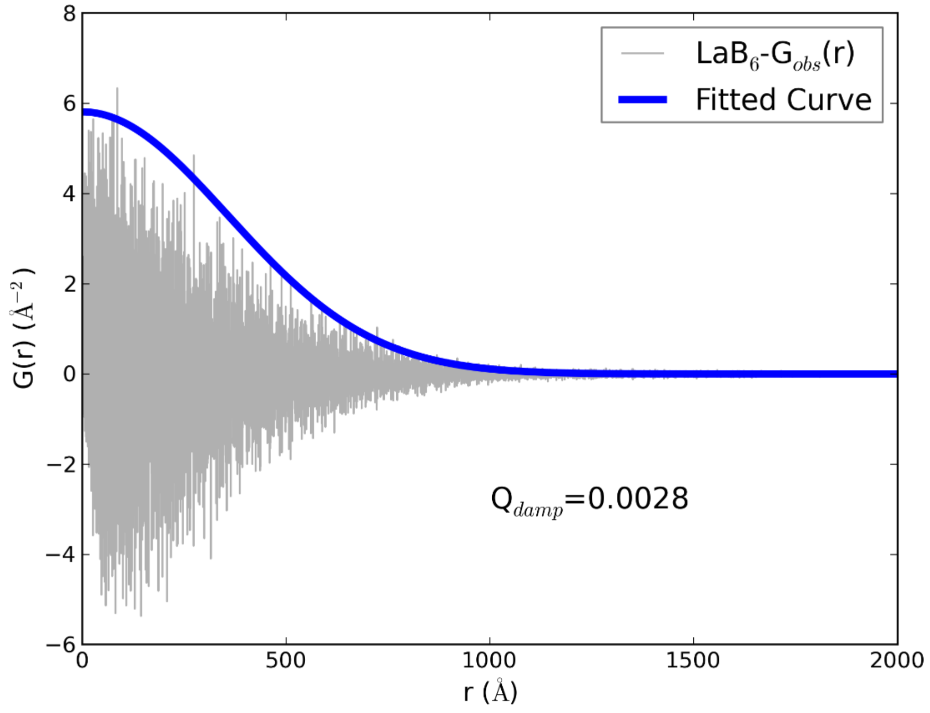

Figure 17 - *Gaussian damping envelope of LaB_6 PDF data obtained at MSPD beamline at ABLA.*

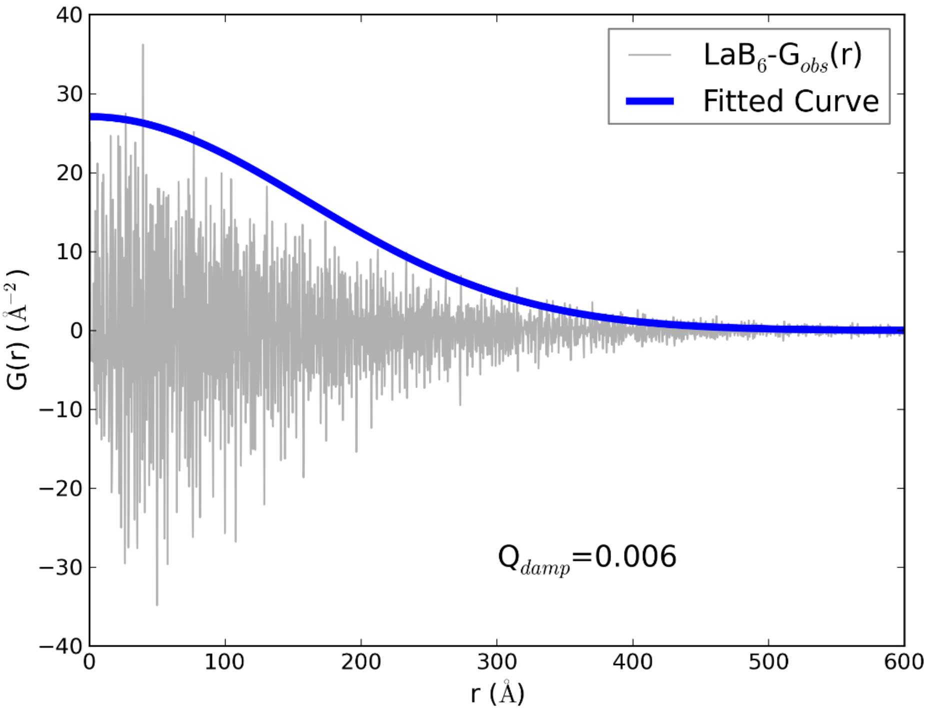

***Figure 18** - Gaussian damping envelope of LaB$_6$ PDF data obtained at Mo K$_{\alpha 1}$ diffractometer.*

The Q_{damp} values due to the limited resolution in Q-space, are 0.025, 0.0028 and 0.006 and the fits of LaB$_6$ PDF data show that the structural correlations can be detected up to 130 Å, 1150 Å, 500 Å (r_{max}) for the P02.1 beamline, the MSPD beamline and the Mo K$_{\alpha 1}$ diffractometer, respectively. The r_{max} and Q_{max} values of LaB$_6$ at the different instruments are illustrated in ***Figure 19***. These characteristic values will be used for further PDF analyses. Results indicate that the MSPD shows the best compromise between the Q_{max} (high) and detectable structural correlations region (high angular resolution). Therefore, it allows both Rietveld and PDF applications at the same time with high quality.

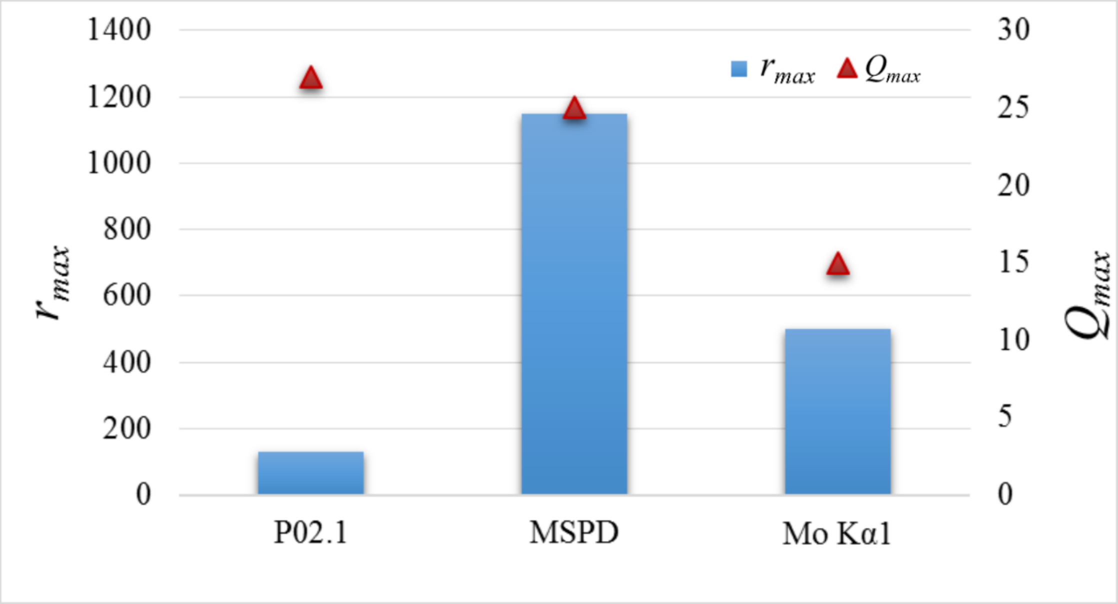

Figure 19 *– The r_{max} and Q_{max} values of LaB_6 for different setups.*

3.3.2. The Effect of SDD on PDF Data at P02.1

The Q_{damp} and Q_{max} values of the setup at beamline P02.1 were determined at different sample-to-detector distances (SDD) shown in ***Figure 20***. It is clearly seen that the Q_{max} and Q_{damp} values increase due to lower angular resolution when the detector is closer to the sample. If the correlations in the PDF are within the instrument envelope, the crystallite size can be determined directly by the peak attenuation. Note that a lower Q_{damp} value means access to a longer-range structural coherence. Therefore, it is important to determine the dampening factor (Q_{damp}) of a setup and the observable PDF correlation region before the PDF experiment. The SDD value can then be chosen accordingly for the desired type of measurement. The maximum observable correlations in the PDF within the instrument envelope at different distances are tabulated in ***Table 8***. Note that the maximum observable correlations in the PDF also depend on the setup i.e. detector resolution. For instance, for a nanocrystalline sample with 150 Å crystallite size the detector must be moved to at least 250 mm distance from the sample to determine the crystallite size. However, in order to investigate the local structure with a high real space resolution, the detector must be closer to the sample (200 mm), because high angular resolution is not necessary for PDF analysis.

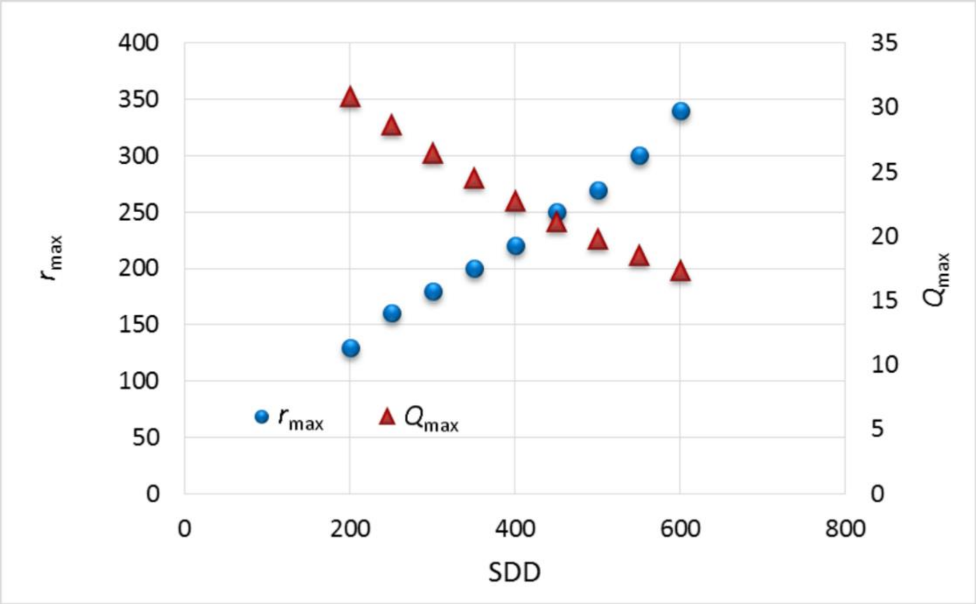

Figure 20 – The r_{max} *and* Q_{max} *values of* LaB_6 *at different sample-to-detector distances (SDD).*

Table 8 – Maximum observable correlation lengths that depend on the setup i.e. detector resolution in the PDF within the instrument envelope.

SDD (mm)	200	250	300	350	400	450	500	550	600
r_{max} (Å)	130	160	180	200	220	250	270	300	340

3.3.3. The Effect of Exposure Time on PDF Data at P02.1

For high quality PDF data high Q_{max} value, good statistics at high Q-value (which determines the width of the peaks in the PDF), sufficient flux at short wavelengths and low levels of background are necessary. The data collection time differs according to the strength of the scatterers and the sensitivity of the detector. Chupas *et al.* 2007, demonstrated that the *a*-Si flat panel detector can enable high resolution, high sensitivity and fast time-resolved PDF studies for Ni having sharp Bragg peaks and amorphous SiO_2 which has weak scattering intensity with absence of Bragg reflections [89]. Their PDF studies on Ni shows that the signal-to-noise ratio at high Q-values slightly improved with increasing exposure time and that the ripples at low-r values in the PDF from systematic errors got smaller. In the case of amorphous SiO_2 the effect of counting time is even more pronounced, so that the quality of the PDF got worse with decreasing exposure time due to declined statistics at high *Q-values*. In the case of deteriorated signal-to-noise ratio, one has to reduce the usable Q-range and this again introduces termination ripples. However, even in this situation the quality of the PDF of amorphous SiO_2 for 13s counting time by using a *a*-Si flat panel detector was good, there was no big difference to that of 80s.

The effect of exposure time on the quality of the PDF data was investigated at beamline P02.1. The high voltage lithium-ion battery cathode material $LiNi_{0.5}Mn_{0.5}O_4$ [13] was measured at a SDD of 400 mm with different exposure time (5s, 10s, 20s, 30s, and 60s). The structure functions, *S(Q)*, that oscillates around 1 at high Q are shown in ***Figure 21***. There is no significant difference between the structure functions especially in the low Q region. The signal-to-noise ratio decreases with increasing Q in *S(Q)* due to the Debye-Waller factor and it is clearly seen in the inset that the ratio gets slightly worse with decreasing exposure time. The better signal-to-noise ratio is reflected by a smoother curve.

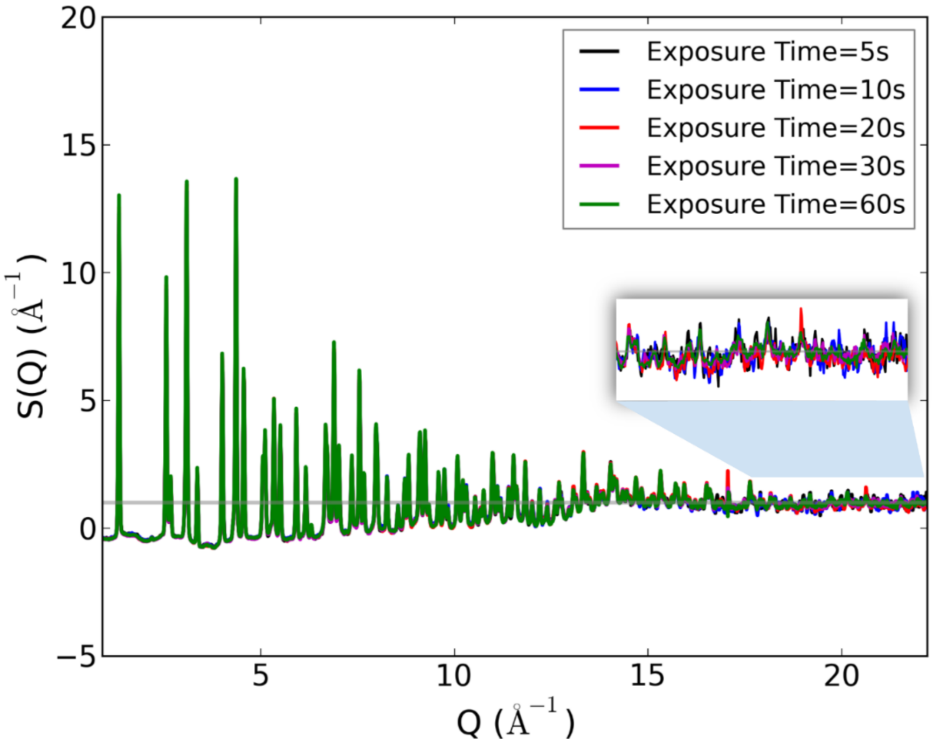

Figure 21 *– The experimental structure functions, S(Q), of* $LiNi_{0.5}Mn_{0.5}O_4$ *collected with different exposure times.*

The signal-noise ratio effect can also be seen in the reduced structure function graph, $F(Q)=Q(S(Q)-1)$, that oscillates around 0 at high Q (***Figure 22***). In spite of a lower statistics at high Q for short exposure time, the structural features in the PDF are still the same (***Figure 23***). A comparison of the PDFs recorded from 5s to 60s is illustrated in ***Figure 24***. It is clearly seen that there is no difference in the short range of the PDF which shows that a measurement time of 5s is sufficient when using a 2D flat panel detector. This indicates that fast time-resolved experiments are possible for PDF analysis.

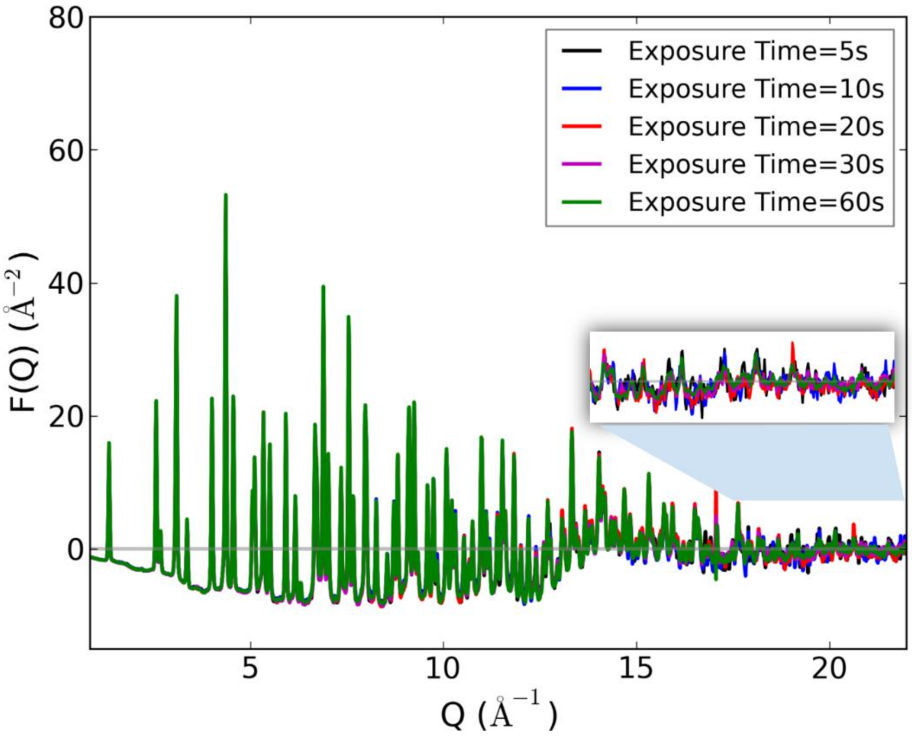

***Figure 22** – The experimental reduced structure functions, F(Q), of LiNi$_{0.5}$Mn$_{0.5}$O$_4$ collected with different exposure times.*

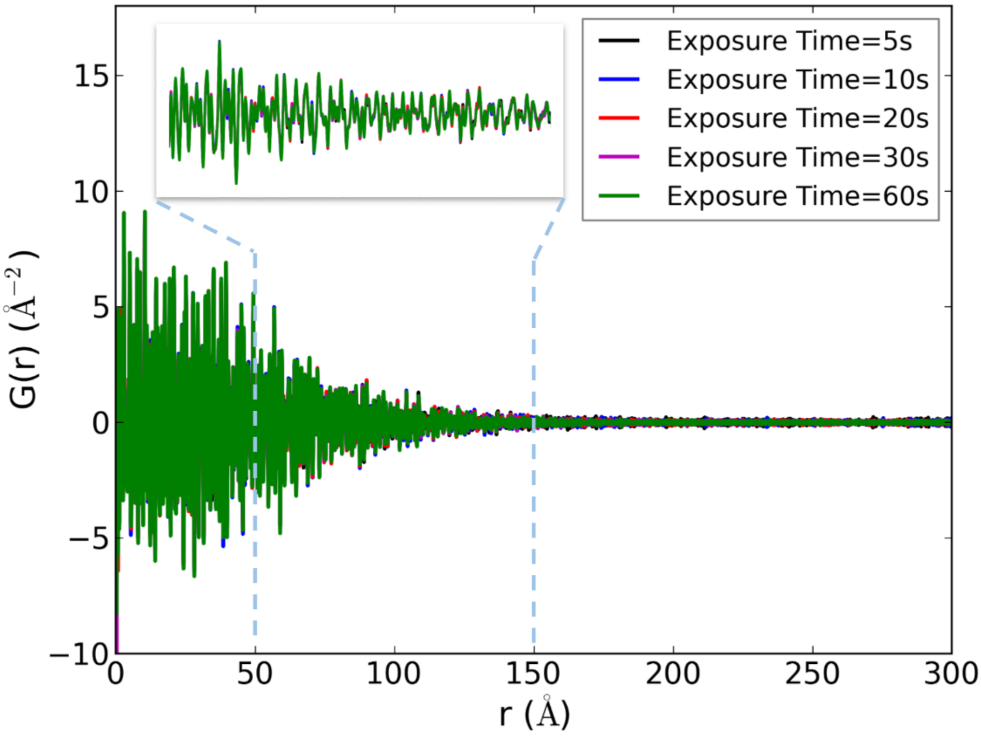

***Figure 23** - The experimental PDFs of LiNi$_{0.5}$Mn$_{0.5}$O$_4$ for different exposure times (at SDD of 400 mm in **Table 8**).*

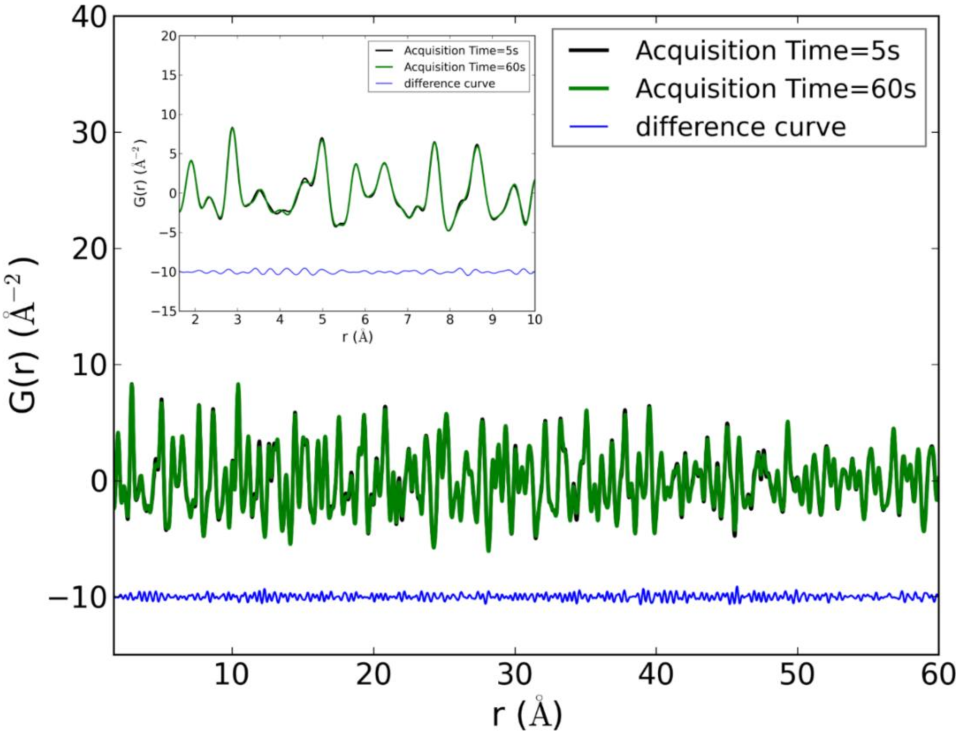

Figure 24 *- The comparison of experimental PDFs of* $LiNi_{0.5}Mn_{0.5}O_4$ *collected within 5s and 60s exposure time and associated difference curve.*

The corresponding residual values of the PDF fits performed with PDFGui [90] are very similar and above 17% with a slight decrease with increasing exposure time for these PDF refinements (***Figure 25***).

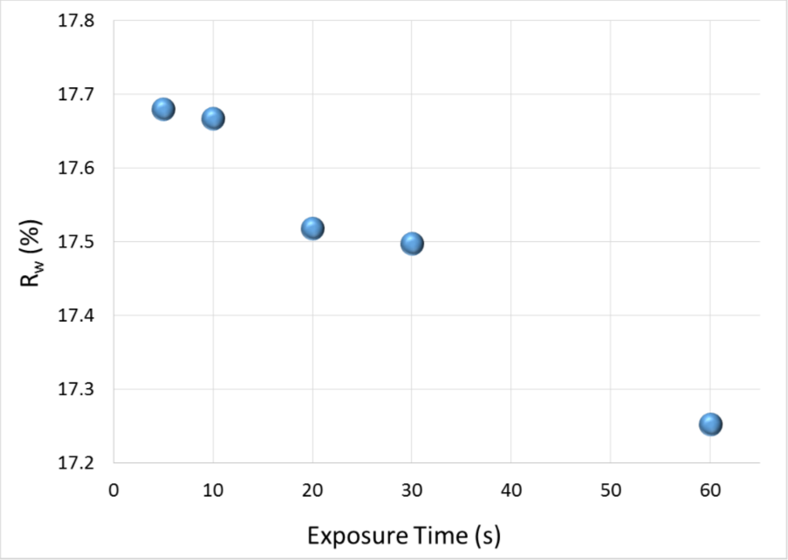

Figure 25 *- Corresponding* R_w *values of PDF fits of* $LiNi_{0.5}Mn_{0.5}O_4$*.*

3.4. Data Processing

3.4.1. 2D Data Integration

The detector calibration and the two-dimensional image integration were performed with the X-ray image processing software FIT2D [91]. The correct sample-detector distance, the center of the Debye-Scherrer rings on the detector and the detector tilt angles were found in FIT2D by measuring a LaB_6 standard sample. Artefacts as the shadow of the beam-stop or dead pixels are masked in the software and excluded from further data treatment shown in ***Figure 26***. The unmasked area was then used to extract the diffraction intensity. After masking, appropriate start values for sample-to-detector distance (in milimeters), wavelength (in Ångstroms), horizontal and vertical pixel size of the detector (in microns) have to be given as shown in ***Figure 27***.

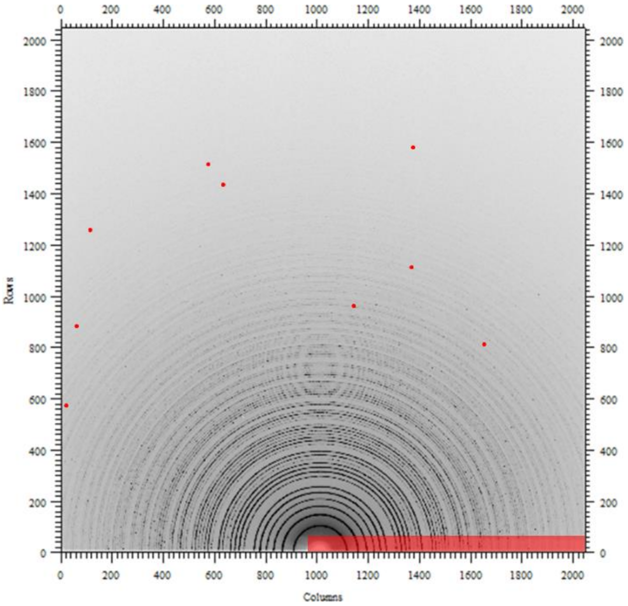

Figure 26 *- Masked area on a two-dimensional diffraction image of* LaB_6*.*

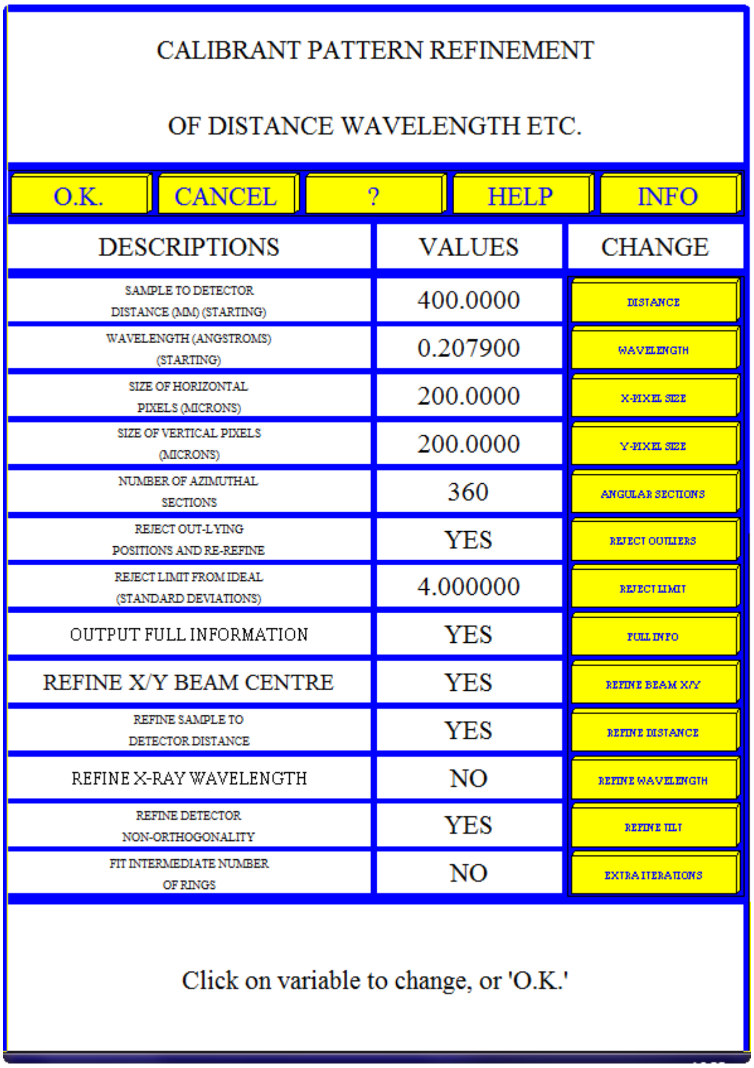

CALIBRANT PATTERN REFINEMENT

OF DISTANCE WAVELENGTH ETC.

DESCRIPTIONS	VALUES	CHANGE
SAMPLE TO DETECTOR DISTANCE (MM) (STARTING)	400.0000	DISTANCE
WAVELENGTH (ANGSTROMS) (STARTING)	0.207900	WAVELENGTH
SIZE OF HORIZONTAL PIXELS (MICRONS)	200.0000	X-PIXEL SIZE
SIZE OF VERTICAL PIXELS (MICRONS)	200.0000	Y-PIXEL SIZE
NUMBER OF AZIMUTHAL SECTIONS	360	ANGULAR SECTIONS
REJECT OUT-LYING POSITIONS AND RE-REFINE	YES	REJECT OUTLIERS
REJECT LIMIT FROM IDEAL (STANDARD DEVIATIONS)	4.000000	REJECT LIMIT
OUTPUT FULL INFORMATION	YES	FULL INFO
REFINE X/Y BEAM CENTRE	YES	REFINE BEAM X/Y
REFINE SAMPLE TO DETECTOR DISTANCE	YES	REFINE DISTANCE
REFINE X-RAY WAVELENGTH	NO	REFINE WAVELENGTH
REFINE DETECTOR NON-ORTHOGONALITY	YES	REFINE TILT
FIT INTERMEDIATE NUMBER OF RINGS	NO	EXTRA ITERATIONS

Click on variable to change, or 'O.K.'

Figure 27 *- Calibrant pattern refinement parameters for measured LaB_6 sample with a 16-inch two-dimensional flat panel detector of the XRD 1621 N ES Series (Perkin-Elmer).*

After giving the appropriate initial parameters, three or more points are selected on the inner diffraction ring. The program then defines an initial beam centre and refines the refineable parameters.

To get a one-dimensional pattern with intensity vs. 2θ, the image has to be integrated. This can be done in different ways such as partial integration, often called ‘cake integration’ [83]. In the cake integration, the integrated region is defined by a graphical coordinate input for the starting azimuth, end azimuth and inner and outer radii of the integrated area. In this case, the integrated region lies completely on the detector. For full integration, a rectangular area is used for integration. As a consequence some of the data in the rectangle lies outside the detector or the rectangle has to be chosen small enough so that all points are within the measured area thereby wasting a considerable amount of intensity. The full and cake integration of a 2D diffraction image of LaB_6 are shown in ***Figure 28*** and their integrated 1D diffraction patterns in ***Figure 29***. In the image integration processing, the software takes the intensities in the detector pixels and assigns them to the correct bins of the 1D array [92]. In the upper right image in ***Figure 29***, at higher *Q*-values the signal of the full integration becomes compromised near the detector edge that adds noise to the obtained PDF. However with the cake integration, these challenges can be solved.

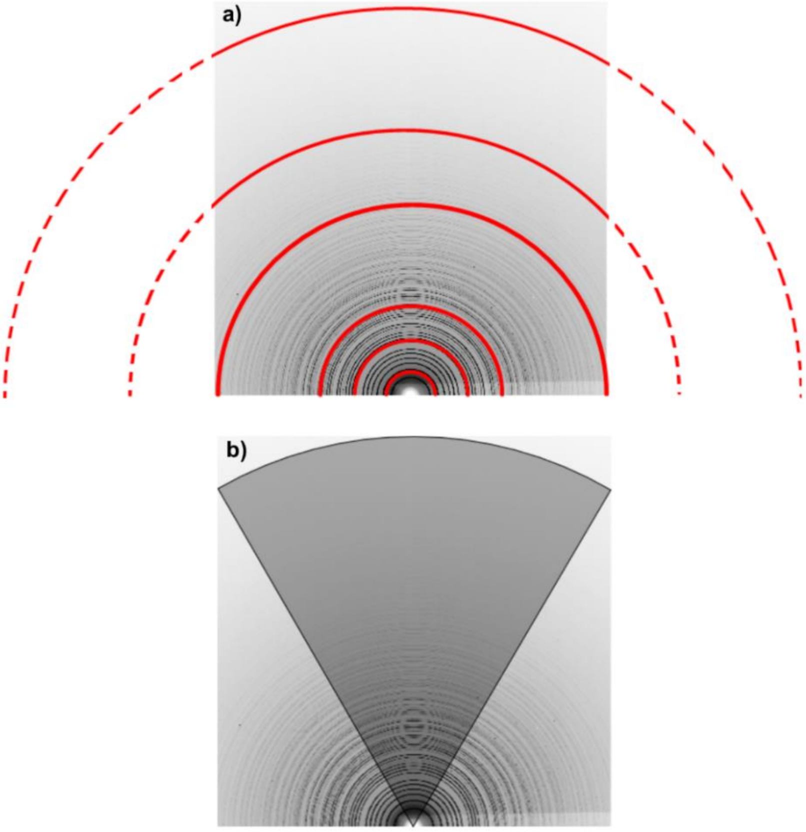

Figure 28 - *Illustrating the full integration (a) and cake integration (b) on the two-dimensional diffraction image of LaB_6.*

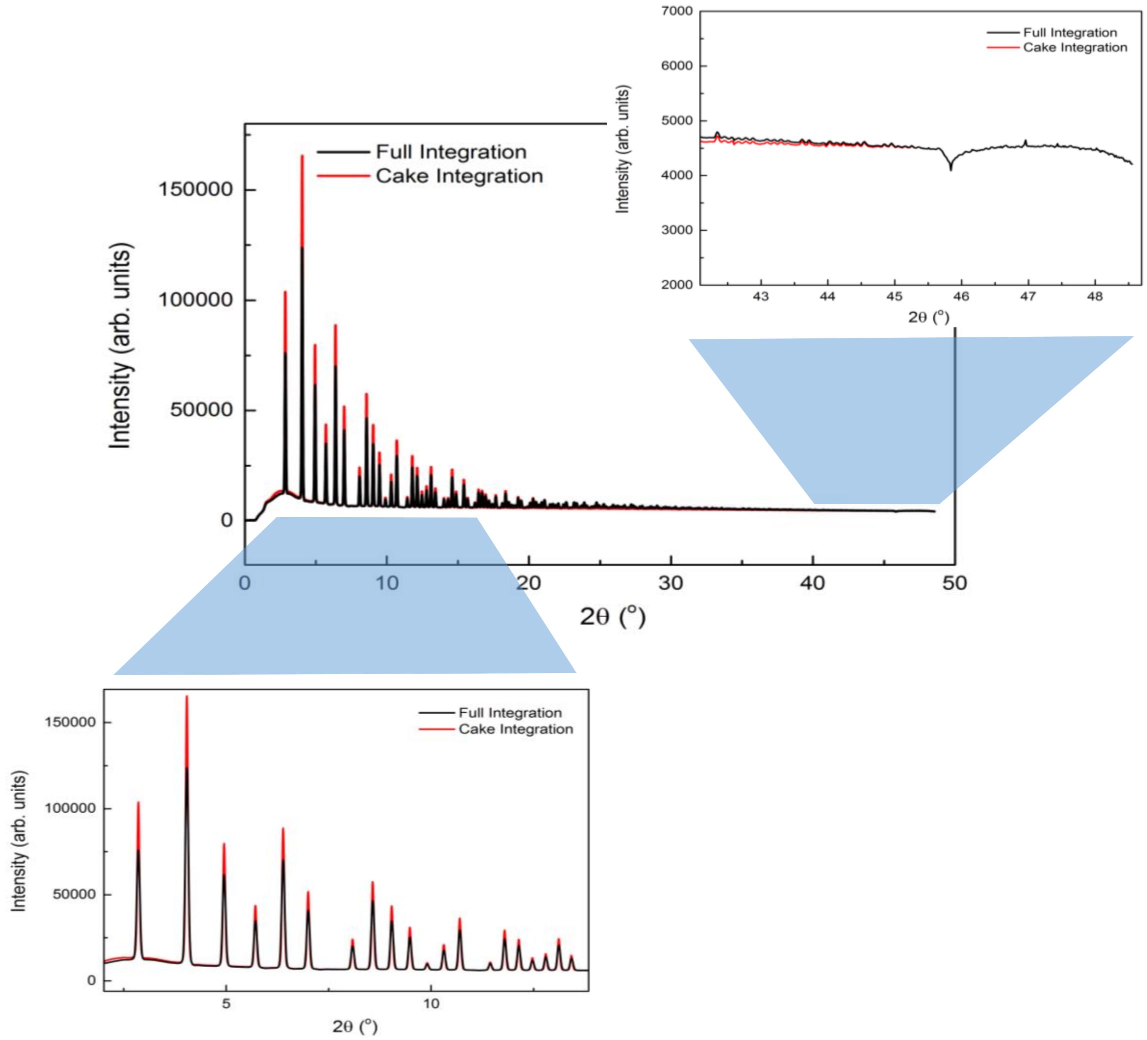

Figure 29 - The full and cake integrated 1-D diffraction patterns of LaB_6*.*

3.4.2. Rietveld Refinement

The structure analysis based on the diffraction pattern was performed with the Rietveld method using the Fullprof software package [68]. Lattice constants, phase fractions, microstructural parameters, distances, atomic coordinates and occupancy parameters can be extracted using a least squares procedure, in order to minimize the difference between the calculated and the experimental diffraction data. The instrumental resolution function was obtained using a LaB_6 standard from NIST.

3.4.3. PDF Data Reduction

Before PDF analysis some corrections such as background subtraction, sample absorption, polarization, multiple and Compton scattering have to be applied to the total scattering data. This can be done using the PDFGetX2 [93] or PDFGetx3 [94] software.

3.4.3.1. PDF Data Reduction – PDFGETX2

X-ray PDF data of samples and standard materials from beamline P02.1 and Mo Kα_1 laboratory source were processed using the PDFGetX2 software [93], which is a user-friendly graphical user interface (GUI) software to perform standard corrections such as background subtraction, sample absorption, polarization, multiple and Compton scattering and then to obtain the pair distribution function (PDF) from the measured X-ray powder diffraction data by performing a Fourier transformation.

The measured intensities consist of additive components such as coherent, incoherent and background scattering, and multiplicative components such as normalization, multiple scattering, absorption and polarization [93,95]. It is described below.

$$I_{measured} = NMAP\left(I_{coh} + I_{incoh}\right) + I_{bkg} \tag{35}$$

where \`$N$´ is the normalization factor (normalization by the average atomic scattering power), \`M´ is the multiple scattering, \`$A$´ is the sample self-absorption correction, \`P´ is X-ray polarization correction, \`$I_{coh}$´ is the coherent intensity, \`I_{incoh}´ is the incoherent intensity and \`I_{bkg}´ is the background.

3.4.3.1.1. Background Subtraction

Intensity of background comes from the sample container (e.g. glass capillary, Kapton foil or empty sample can) and air. It is better to measure the sample without a background contribution to the total scattering for increased accuracy [8]. An empty borosilicate capillary with low absorption coefficient was measured to estimate the contribution of the sample container to the background in the *ex situ* measurements. An empty *in situ* battery cell with glass and glassy carbon windows, separator and electrolyte were used for background estimation in the *in situ* battery measurement. The intensity of the measured background scattering consists of around 75.6% air scattering and 24.4% empty capillary as shown in ***Figure 30***.

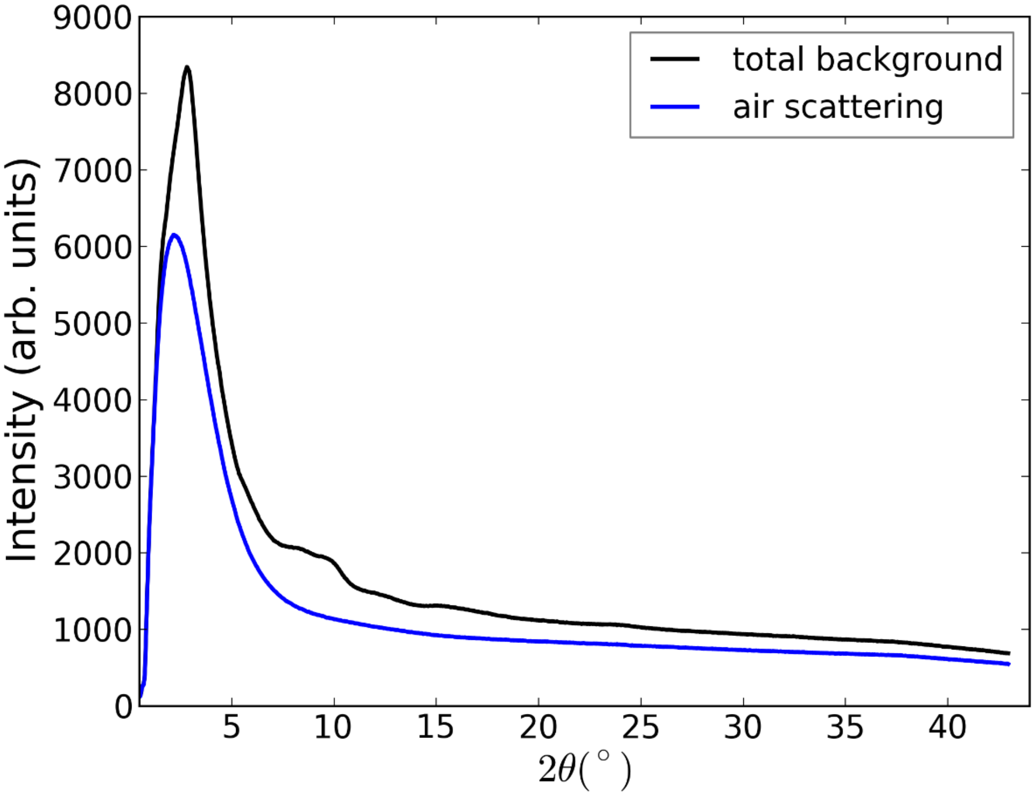

Figure 30 *- Total background intensity (black) and intensity from air scattering (blue). The measurements were carried out at a sample-to-detector distance of 400 mm at the High Resolution Powder Diffraction beamline (P02.1) at PETRA-III, DESY, using 60 keV X-rays.*

3.4.3.1.2. Incoherent Intensity Subtraction

All relevant scattering processes after the collision between the X-ray photon and the electrons surrounding the atomic nuclei can be categorized as in ***Table 9***.

Table 9 *– Different scattering processes relevant in a total scattering measurement.*

Scattering Processes	
Coherent elastic	Bragg scattering
Incoherent elastic	Laue monotonic diffuse scattering
Coherent inelastic	Phonons (vibrational waves), magnons (spin waves) and thermal diffuse scattering
Incoherent inelastic	Compton scattering

The incoherent and inelastic scattering mainly consists of Compton scattering and contributes to the background intensity in the X-ray diffraction pattern. The incoherent scattering has no structural information due to lack of interference of the scattered waves. For that reason, it has to be removed from total scattering. Particularly, at high Q-values, the Compton scattering becomes larger than the elastic scattering and it can be corrected using the Breit-Dirac recoil factor (R) (see Equation 36) [96]. The Compton scattering intensities, which are tabulated in the International Tables of Crystallography C, are multiplied by the Breit-Dirac recoil factor before being subtracted from the data.

$$R = \left(\frac{\lambda}{\lambda'}\right)^2 = \frac{1}{(1 + \frac{2h}{mc}\frac{\sin^2\theta}{\lambda})^2} \tag{36}$$

where λ and λ´ are the wavelength of incident and Compton scattered beam. After subtraction of the Compton scattering using the Breit-Dirac recoil factor from the total scattering, if the data still contains the Compton scattering in mid-low Q-region, additional corrections are necessary such as the Ruland window function [97].

3.4.3.1.3. Absorption Correction

Beside contributions from the sample container, the absorption in the sample itself has to be considered. It affects the measured intensity which is the essential information in the scattering curve. It is determined during the data treatment using chemical composition, sample thickness, the packing fraction and the linear attenuation coefficient (μ) of the sample.

3.4.3.1.4. Multi Scattering Correction

Multiple scattering is only calculated up to double scattering that is often the dominant contribution to the intensity of multiple scattering. This multiple scattering depends on experiment geometry and absorption coefficient and is corrected using the double scattering ratio, which is given by Warren and Mozzi [98]. This correction is only significant when the sample is rather absorbing or in the case of high energy. For non-strong absorbing samples, it can be neglected.

3.4.3.1.5. Polarization Correction

The monochromatic incident beam of synchrotron radiation is theoretically linearly full polarized in the horizontal plane, however, in practice, the beam is not completely polarized (95% polarized) and for that reason, small corrections might be necessary. The polarization correction factor, P, using a crystal monochromator is given by Eq. 37 [8,99].

$$P = \frac{\left(1 + x\cos^2 2\theta\right)}{1 + x} \tag{37}$$

where 2θ is the scattering angle and x is the constant which depends on the degree of polarization of the incident beam. x is given by $x=(1-f)/(1+f)$, where f is the polarization rate of the incident radiation in the direction perpendicular to the scattering plane. Using Eq. 37 the polarization correction factor is calculated as shown in ***Figure 31***.

If the radiation is unpolarized, f=0 and x=1

If the radiation is fully polarized, f=1 and x=0.

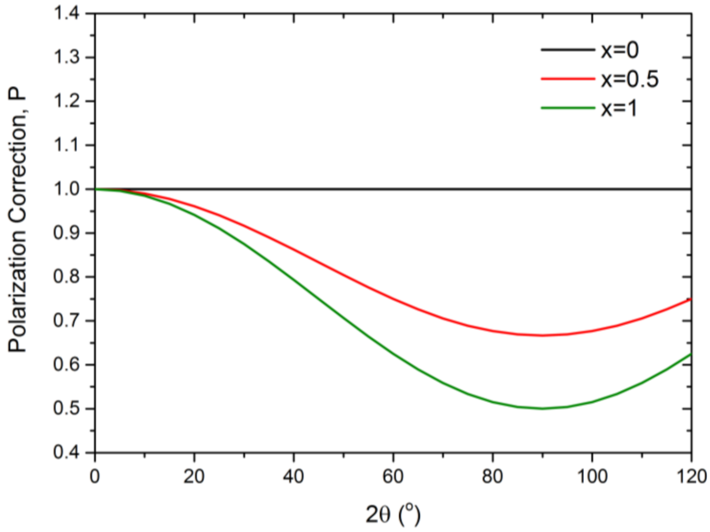

***Figure 31** – Polarization factor vs. scattering angle (2θ) for monochromator that is located in the incident beam. The black and green lines correspond to the fully polarized beam and unpolarized beam, respectively.*

3.4.3.1.6. Anomalous Scattering and Absorption Correction

In the last step to obtaining the corrected PDF the determined *S(Q)* has to be divided by the mean-square average atomic scattering factor <f(Q)>^{2}, which is defined as

$$\langle f(Q)\rangle^2 = \left[\sum_a c_a(f_a^0 + f_a' + if_a'')\right]^2 = \left[\sum_a c_a(f_a^0 + f_a')\right]^2 + \left[\sum_a c_a f_a''\right]^2 \qquad (38)$$

where c_a is the concentration of the atom species, $f_a^0(Q)$ is the Q-dependent atomic form factor of a species, f_a' and f_a'' are the real and imaginary terms of the energy-dependent anomalous scattering, respectively. Anomalous scattering occurs whenever the energy of the incident radiation is close to an absorption edge of the scatterer. The anomalous scattering corrections can be neglected if the incident X-ray energy is not close to an absorption edge of one of the elements.

3.4.3.2. PDF Data Reduction – PDFGETX3

Another software for data reduction is PDFGetx3, which allows to processes several hundred data sets in a few minutes. The reduced structure function is corrected using an eighth-degree polynomial approximation that is for rapid acquisition PDF data. PDF data of *in situ* measurements and measurements from the MSPD beamline were processed using PDFgetX3 [94].

3.4.4. The Difference between Rietveld and PDF Analyses

There are some differences between the Rietveld and PDF methods. While Rietveld refinement makes use of reciprocal space data I(Q) or I(2θ), a PDF refinement is applied to in real space data after Fourier transformation. Additionally, in the Rietveld method both instrumental and sample contributions affect the intensity profiles. However, the PDF method does not use any instrument profile. In this case, the Rietveld method gives lattice parameters with better accuracy than the PDF method. For that reason, in comparison of cell parameters of PDF and Rietveld analyses, there is a systematic offset. Another difference is that the PDF method allows analysing specific ranges in real space and to refine all parameters with respect to the selected length scale such as local, medium or long-range scale.

3.4.5. PDF Data Analysis

In a PDF refinement, the structural parameters are modelled to the data in real space. The modelled and the experimental data are compared and the difference between both is described by the goodness-of-fit parameter. The PDF data can be analysed by using a ‘small-box modelling’ or a ‘big-box modelling’. In the small box approach, a unit cell is defined, which is periodically repeated in space. This unit cell contains all structural information including deviations from ideal symmetry. The structural parameters of this cell are then refined based on the experimental PDF data. By this way more than one crystallographic phase can be treated. In a big-box approach on the other hand, the structure is described using a ‘big box of atoms’, e.g. a 10x10x10 supercell that describes either a complete nanoparticle or at least a large volume fraction of the material. All structural parameters in this supercell, as for instance atomic positions, can then in principle be refined. The other difference between small-box and big-box modelling is that in the big-box approach only interatomic distances within the one big box are considered, while in the small box also interatomic distances between neighboured boxes are taken into account.

3.4.5.1. Small-Box Modelling

The program PDFGui [90] was used for extracting structural information from the total scattering diffraction data in real space using small-box modelling. The small-box modelling approach implies the refinement of one unit cell with periodic boundary conditions using a least-squares procedure to minimize the residual intensity between measured and modelled data. The main difference to conventional Rietveld refinement is that the local structure which is not considered in the average structure is being fit [100]. The results of the real space refinement in PDFGui (and also in DISCUS [101]) can be compared quantitatively with that of conventional Rietveld refinements. The advantage of PDFGui is that the PDF can be modelled quickly and simply for defined ranges r_{min}-r_{max} in real space. PDFGui is a user-friendly graphical user interface built on the PDFfit2 engine and it allows fitting of multiple phases.

During PDF refinement, the sample dependent parameters such as unit cell parameters, atomic fractional coordinates, correlated atomic motion parameter and atomic displacement parameters are refined and dampening of PDF peaks that is the experimental parameter (Q_{damp}) was fixed.

In this refinement, the residual functions, which are a measure of the disagreement between the calculated and experimental PDF, are equivalent to that of conventional Rietveld refinements. The weighted disagreement factor, R_w, is defined as:

$$R_w = \sqrt{\frac{\sum_{i=1}^{N} w(r_i)[G_{obs}(r_i) - G_{calc}(r_i)]^2}{\sum_{i=1}^{N} w(r_i) G_{obs}^2(r_i)}} \tag{39}$$

where w is the same weighting factor as in the Rietveld refinement, $w(r_i)=1/\sigma^2(r_i)$, where σ is the estimated standard deviation on the ith data point at position r_i. The chi-square goodness of fit for a PDF refinement is given by

$$\chi^2 = \frac{R_w}{N - P} \tag{40}$$

where P is the numbers of parameters and N is the total number of points used in the PDF refinement an N is equal to;

$$N = \frac{(r_{max} - r_{min})}{\Delta r} = \frac{(r_{max} - r_{min}) Q_{max}}{\pi} \tag{41}$$

From the PDF refinement unit cell parameters, atomic fractional coordinates, atomic displacement parameters, bond lengths and angles, partial PDFs describing the pair correlations between certain atoms in the material and differential PDFs, which are the pair correlation between specific atoms and all other atoms, can be obtained.

3.4.5.2. Big-Box Modelling

Another approach of analysing the total scattering data in a big box is the so-called Reverse Monte Carlo (RMC) method. The RMC modelling technique was first developed by Mc Greevy and Pusztai in 1988 [102] and allows to extract the structural information from neutron, X-ray and extended X-ray absorption fine structure (EXAFS) measurements [103]. RMC modelling is used in the program package DISCUS [101] which is a useful tool for defect structure simulations and for the analysis of diffuse scattering.

The RMC method is a variation of the standard Metropolis Monte Carlo (MMC) method [103,104]. MMC is a statistical approach and produces randomly an ensemble of atoms with a Boltzmann distribution of energies. While MMC is usually used to minimize the energy of a system in order to generate a disordered structure until reaching minimum energy, RMC minimizes the difference between calculated and observed data within its errors until obtaining an acceptable agreement [105]. The principle of RMC modelling is illustrated in ***Figure 32***. Firstly, it starts with a reasonable initial structure configuration and calculates the diffraction pattern and pair distribution function of the generated structure. Then the goodness of fit parameter χ^2 is calculated as given in (Eq. 42).

$$\chi^2 = \sum_{i=1}^{N} \frac{|I_{obs}-I_{calc}|^2}{\sigma^2} \quad \text{or} \quad \chi^2 = \sum_{i=1}^{N} \frac{|G_{obs}-G_{calc}|^2}{\sigma^2} \qquad (42)$$

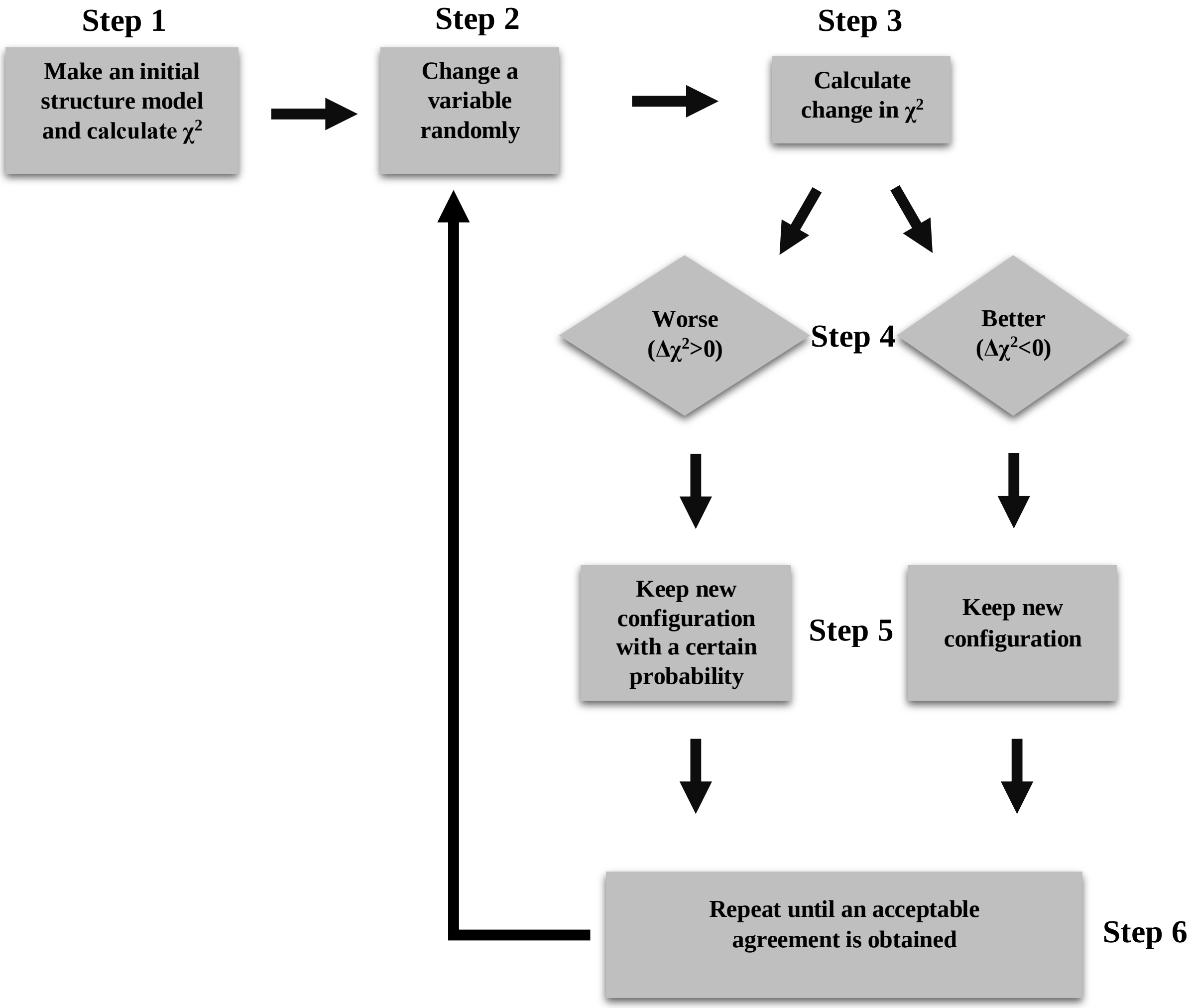

Figure 32 *– The algorithm of Reverse Monte Carlo (RMC) modelling.*

Step 2 is to change a variable in a random direction (move an atom or swap atoms) and then the data and the χ^2 of the new configuration are recalculated. The change of χ^2 is given by $\Delta\chi^2= \chi^2_{(new)}- \chi^2_{(old)}$. After a parameter shift and if $\Delta\chi^2<0$, then the movement is accepted and it will improve the fit; otherwise, if the movement results in a poorer fit ($\Delta\chi^2>0$) it is accepted with a probability, P, which is given by Equation (43). The parameter σ controls how many bad moves will be accepted. This probability tries that the model converges on the global minimum rather than being trapped in a local minimum.

$$P = \exp\left(-\Delta\chi^2 / 2\right) \tag{43}$$

This process is continued by returning to step 2 and repeated until an acceptable agreement is obtained. In order to ensure that only physically and chemically reasonable structures are obtained, some constraints may be defined. For instance, minimum bond length and bond angle may be restricted and/or specific atoms may be allowed to move only in specific regions of the configuration (restriction of coordinates).

3.5. Sample Synthesis and Preparation

3.5.1. $Al_{0.57}Sn_{0.43}O_{1.71}$

The $Al_ySn_{1-y}O_{2-y/2}$ (y = 0.57) material was prepared by co-precipitation method. In this technique the cation sources are dissolved in an aqueous solution and mixed with a solution of precipitation agent. After the filtration of the precipitates the final crystalline oxide is obtained by calcining the precipitates at various temperatures [106]. $Al_{0.57}Sn_{0.43}O_{1.71}$ was obtained by using $Al(NO_3)_3.9H_2O$ and $SnCl_4.5H_2O$ as precursors. The final product was obtained at different calcination temperatures: 40°C and 550°C after 5 h heating in air [67].

3.5.2. $LiMn_2O_4$

Commercial $LiMn_2O_4$ spinel powder from Alfa Aesar was used. The $LiMn_2O_4$ electrode mixture was prepared from an 80:10:10 (wt. %) mixture of the active material, polyvinylidene difluoride (PVdF) as a binder and super P carbon as a conduction material. These three components were ground in mortar by hand for around 5 minutes and the mixture was pressed with an 8mm diameter pressing tool by applying 2 tons to get a pellet. Finally an *in situ* cell was prepared with this pellet.

Chapter 4 - RESULTS AND DISCUSSIONS

4.1. $Al_{0.57}Sn_{0.43}O_{1.71}$

Issac *et al.* investigated the local environment of $Al_{0.57}Sn_{0.43}O_{1.71}$ by ^{27}Al and ^{119}Sn Magic Angle Spinning (MAS) NMR spectroscopy as well as Sn Mössbauer spectroscopy [67]. ^{27}Al MAS NMR data clearly indicate that the Al^{3+} and Sn^{4+} ions are randomly distributed on the cation sites and the oxygen vacancies are randomly distributed on the anion sites. ^{119}Sn MAS NMR and Sn Mössbauer spectroscopy show that local structural distortions occur on the octahedral site around the Sn^{4+} ions. Such distortions have also been observed for pure (undoped) SnO_2 by ^{119}Sn MAS NMR and Sn Mössbauer spectroscopy when the particle size is reduced to a few nanometers and they have been ascribed to the presence of large amounts of Sn in surface-near regions [107].

4.1.1. $Al_{0.57}Sn_{0.43}O_{1.71}$ calcined at 550°C

4.1.1.1. Rietveld Analysis

The aristotype rutile structure of $Al_{0.57}Sn_{0.43}O_{1.71}$ has a body-centred tetragonal unit cell with a=4.738 Å, 4.738 Å and c=3.186 Å in space group of $P4_2/mnm$ [108] and it consists of edge-sharing SnO_6 octahedra. Each Sn atom (*2a* Wyckoff site) is coordinated to 6 oxygen atoms (*4f* Wyckoff site) and each edge-shared oxygen octahedron is corner-shared with an adjacent infinite chain as illustrated in ***Figure 33***.

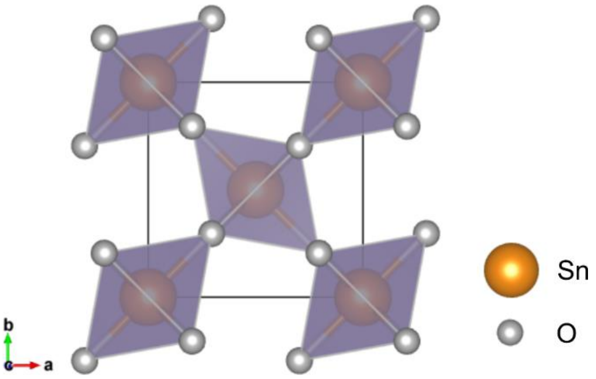

***Figure 33** – Crystal structure illustration of rutile type SnO_2.*

$Al_{0.57}Sn_{0.43}O_{1.71}$ with 0.57 mol Al and 0.43 mol Sn crystallizes in the tetragonal space group *P4₂/mnm*. 14.25% of oxygen is removed to maintain charge balance due to the substitution of 57% Sn^{4+} by Al^{3+}. Al and Sn atoms are randomly distributed on the cation sites (*2a* Wyckoff site) and the oxygen vacancies are randomly distributed on the anion sites (*4f* Wyckoff site).

The Rietveld refinement of the structure parameters based on the synchrotron diffraction pattern of $Al_{0.57}Sn_{0.43}O_{1.71}$ from which the empty capillary measurement had been subtracted, which was measured with SDD of 400 mm at P02.1 beamline at Petra III, was performed with space group *P4₂/mnm*. During Rietveld refinement of tetragonal $Al_{0.57}Sn_{0.43}O_{1.71}$, background points referring to diffuse scattering in our case (29 background points), cell parameters, isotropic thermal displacement parameters and the positions of O atoms were refined with an R_{wp}-value of 3.76 %.

The refinement of the model and structure parameters based on the synchrotron diffraction pattern is shown in ***Figure 34***. According to the micro-strain analysis, the average crystallite size is 14 (±3) Å. The first neighbour distances of metal-oxygen (Al/Sn-O) are 2.042 Å and 2.058 Å in a unit cell of 4.749(9) Å (a=b) and 3.164(8) Å (c) as tabulated in ***Table 10***.

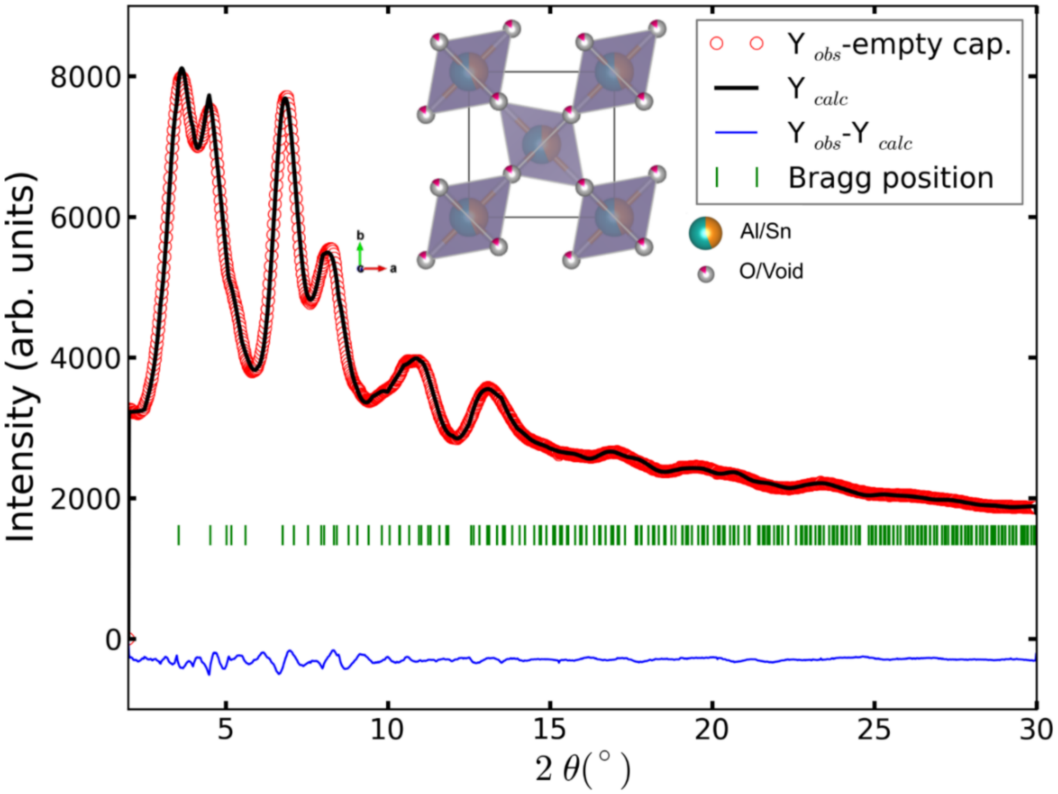

Figure 34 *- Synchrotron diffraction pattern of* $Al_{0.57}Sn_{0.43}O_{1.71}$ *nanoparticles calcined at 550°C and measured in a 0.5 mm capillary at a wavelength of 0.2079 Å.*

Table 10 *- Rietveld results of* $Al_{0.57}Sn_{0.43}O_{1.71}$ *nanoparticles calcined at 550°C.*

Unit cell parameters	a=b=4.749(9) Å and c=3.164(8) Å
Temperature parameters	Al=Sn=0.1(1) Å^2 and O=1.9(9) Å^2
Metal-Oxygen distances*	2.042 Å and 2.058 Å
Average crystallite size	14 (±3) Å

*Note that bond lengths from Rietveld method represent the distances between the average atomic positions.

4.1.1.2. PDF Data Reduction

During PDF data processing using the PDFGetX2 software, all necessary corrections were adequately achieved for background subtraction, absorption, polarization, multiple and Compton scattering. As shown in ***Figure 35*** only the background from the glass capillary gives a considerable contribution. Another high contribution to total scattering data is the inelastic and incoherent Compton scattering that becomes stronger at high *Q*-values.

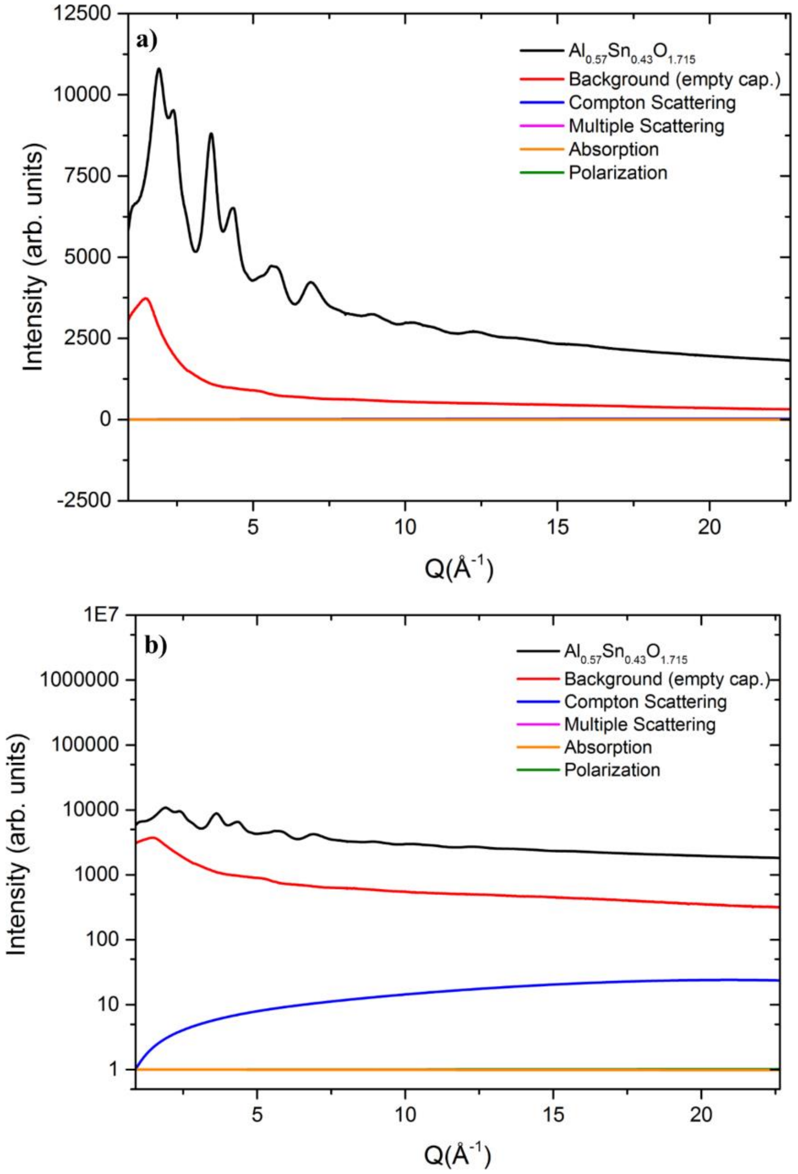

Figure 35 *- XRD pattern of $Al_{0.57}Sn_{0.43}O_{1.71}$, empty capillary measurement and corrections in linear scale (a) and in log scale (b). Q_{max} is 22.6 $Å^{-1}$. Some curves are not visible, because they virtually overlap at nearly zero contribution.*

4.1.1.3. Small-Box Modelling

The challenges of a Rietveld refinement for a nanostructured material are significant owing to the broad Bragg reflections. Nanostructures can be better elucidated from total scattering data, which includes both Bragg and diffuse scattering using PDFGui [90,109] with a small-box modelling approach or DISCUS [101] with a big-box modelling approach. While the small-box modelling approach implies the refinement of one unit cell with periodic boundary conditions using a least-squares procedure, the big-box modelling approach means that up to many thousands of atoms in a big box are individually shifted using an RMC algorithm, in order to get a good fit to the experimental data.

Despite the broad and overlapping peaks in the diffraction pattern, sharp peaks are evident in the PDF for distances up to about 20 Å, which gives the average crystallite size (***Figure 36***). No structural correlations exist beyond this distance. As given in ***Table 8***, the maximum range for observable features in the PDF is up to 220 Å for a SDD of 400 mm, Q_{max}=22.6 Å^{-1}. In this case, the structural correlations in the PDF are within the instrument envelope and the peak attenuation gives directly the crystallite size.

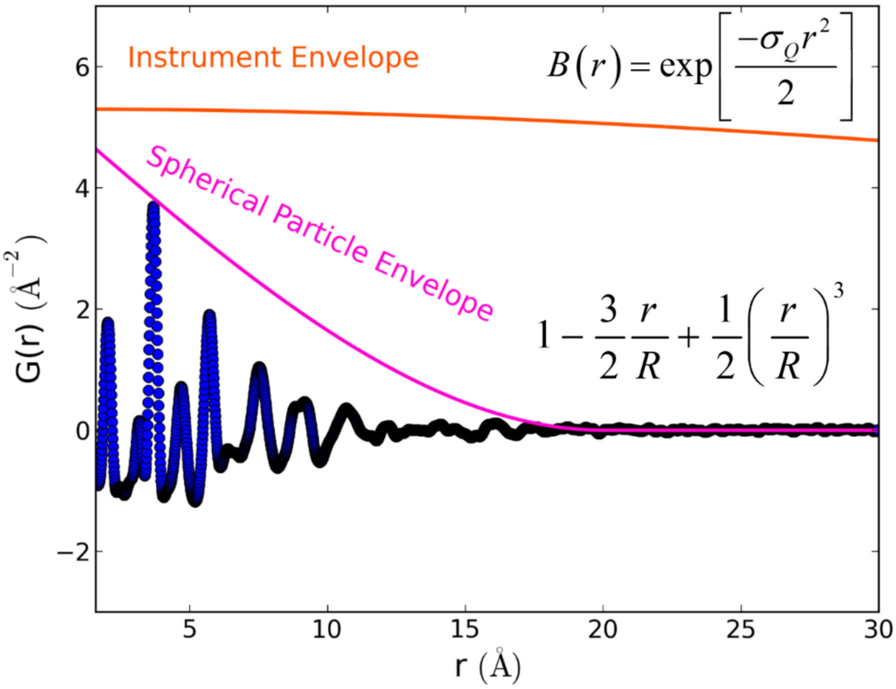

***Figure 36** - Experimental PDF of $Al_{0.57}Sn_{0.43}O_{1.71}$ and illustration of envelopes where σ_Q is the dampening factor and R is the crystallite size.*

The results of the PDF refinement in PDFGui, are given in ***Figure 37***. The results of the conventional Rietveld refinement were used as starting parameters. During PDF refinement of $Al_{0.57}Sn_{0.43}O_{1.71}$ nanoparticles, cell parameters, thermal displacement parameters, the positions of O atoms and atomic correlation parameter (which is a parameter related to the correlated motion of atoms) were refined with an agreement value of R_w of 29.75 %.

The results of the PDF and Rietveld refinements are listed in ***Table 11***. The crystallite size is about 20 Å which is in good agreement with earlier TEM investigations on the same sample [67].

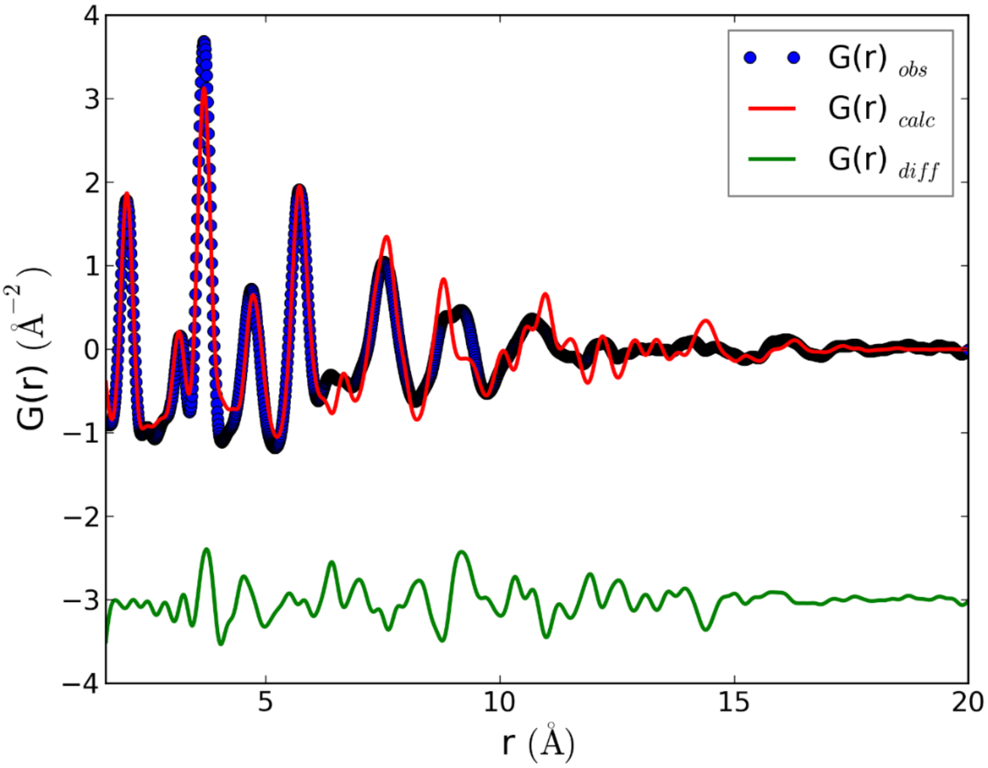

***Figure 37** - PDF refinement of $Al_{0.57}Sn_{0.43}O_{1.71}$* calcined at 550 °C.

Table 11 *- Refinement results from both the PDF and the Rietveld analysis for* $Al_{0.57}Sn_{0.43}O_{1.71}$.

	PDF	**Rietveld**
Atom Distances (Å)		
Sn-O/Al-O	1.96177(1)	2.042
Sn-O/Al-O	2.08921(1)	2.058
O-O	2.86589(1)	2.899
Cell Parameters (Å)		
a=b	4.711630(4)	4.749(9)
c	3.154860(5)	3.164(8)
R_{wp}(%)	29.75	3.76

The cell parameters of $Al_{0.57}Sn_{0.43}O_{1.71}$ (4.711 Å, 4.711 Å, 3.155 Å; from PDF refinement) are smaller than that of the aristotype rutile structure of SnO_2 (4.738 Å, 4.738 Å, 3.186 Å [108] due to the presence of oxygen vacancies and Al^{3+} ions instead of Sn^{4+} ions whose ionic radii's are 0.535 Å and 0.69 Å, respectively [110].

The cell parameters obtained from the Rietveld analysis depend on the type of peak profile as well as the calibration of the instrument constants. A comparison of the PDF and Rietveld analyses shows a systematic offset in the cell parameters in PDF. The interatomic distances of the PDF and the Rietveld analyses are slightly different due to size effects and the fact that the Rietveld refinement describes the local distortions as an increase in the Debye-Waller factor [111]. Therefore, the Rietveld refinement does not result in a good fit. An estimation of the validity of the Scherrer equation is given in [112] for an upper crystallite size of l00-200 nm and in [113] for a lower limit of 3 nm, in this case the overlapped XRD peaks become so broad and low that they are difficult to be distinguished from the background. Moreover, due to the concurrence of disorder inside the $Al_{0.57}Sn_{0.43}O_{1.71}$

nanoparticles and the small crystallite size (~2 nm), the Scherrer equation is less accurate [114].

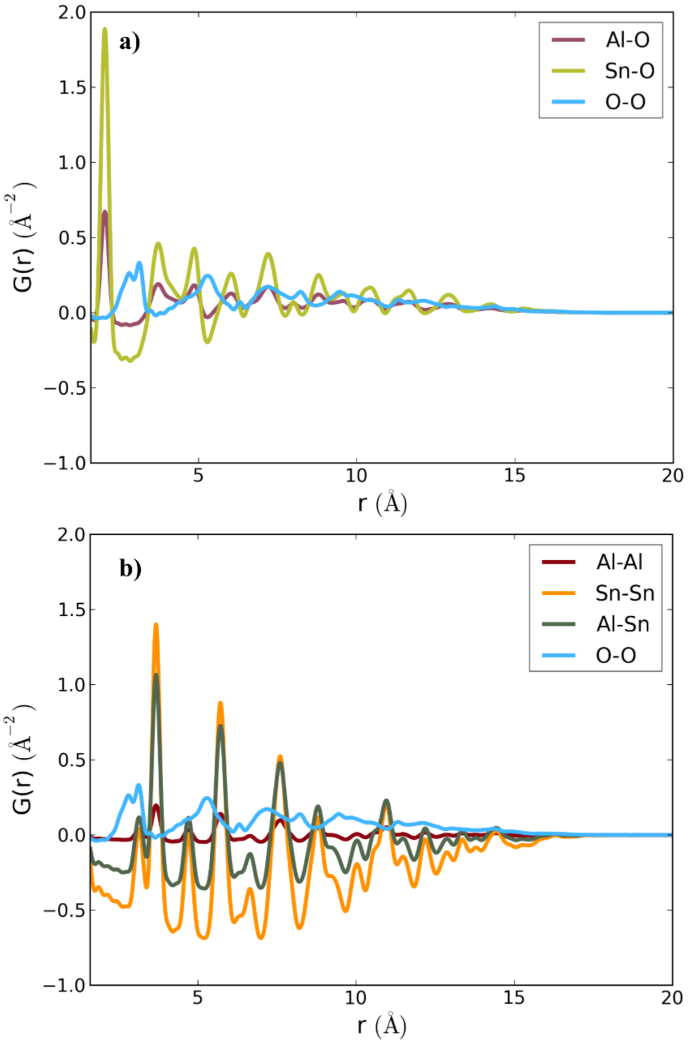

Figure 38 *- Partial PDF of* $Al_{0.57}Sn_{0.43}O_{1.71}$.

After PDF refinement weighted partial PDFs can be obtained as shown in ***Figure 38***. The first peak in the PDF indicates the nearest neighbour distances of metal and oxygen at 1.96177(1) Å and 2.08921(1) Å. The nearest neighbor distances of metal-metal are 3.154860(5) Å, 3.686190(4) Å and 4.711640(4) Å which are indicated by green, yellow and brown arrows, respectively (***Figure 39***).

The PDF peak width is a measure for the amplitude of the relative motions of the atom pairs [115]. In a correlated motion next-neighbor atoms tend to move in-phase with each other, whereas far-neighbor atoms move more independently. At low r-values the correlated motion sharpens the PDF peaks. The PDF refinement of $Al_{0.57}Sn_{0.43}O_{1.71}$ resulted in a large atomic correlation parameter (3.56).

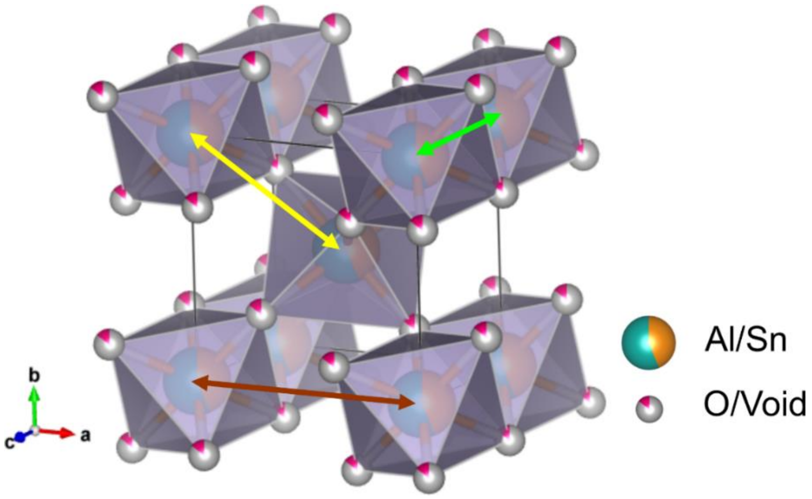

Figure 39 *- Aristotype rutile structure of* $Al_{0.57}Sn_{0.43}O_{1.71}$.

4.1.1.4. Big-Box Modelling

In order to investigate the structure of the nanoparticle with the big-box modelling approach, one has to create a nanoparticle first. Then two different RMC operation modes are used which consist of swapping atoms and displacing the atom positions.

4.1.1.4.1. Nanoparticle Modelling

Firstly a 7x7x7 supercell of the aristotype rutile structure of SnO_2 as the initial structure in $P4_2/mnm$ space group was generated. Then a 20 Å diameter nanoparticle was cut out of the box shaped ensemble and all atoms outside the particle were purged and a SnO_2 nanoparticle with 349 atoms was obtained (***Figure 40***).

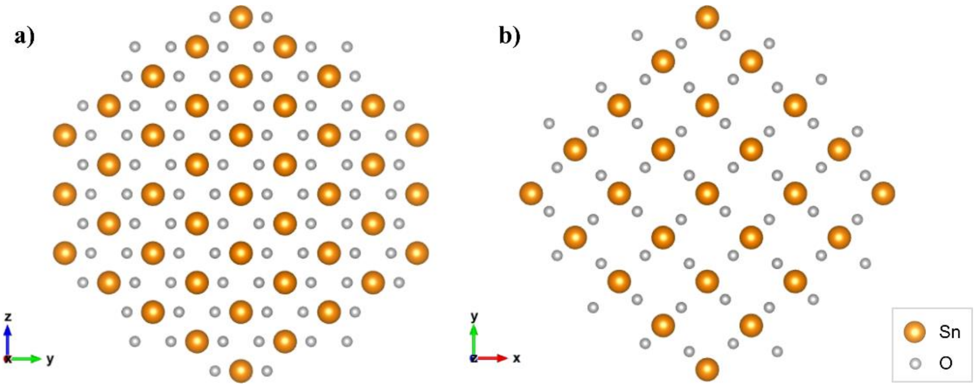

Figure 40 *– Crystal structure of the SnO_2 nanoparticle viewed along the a-axis (a) and the c-axis (b).*

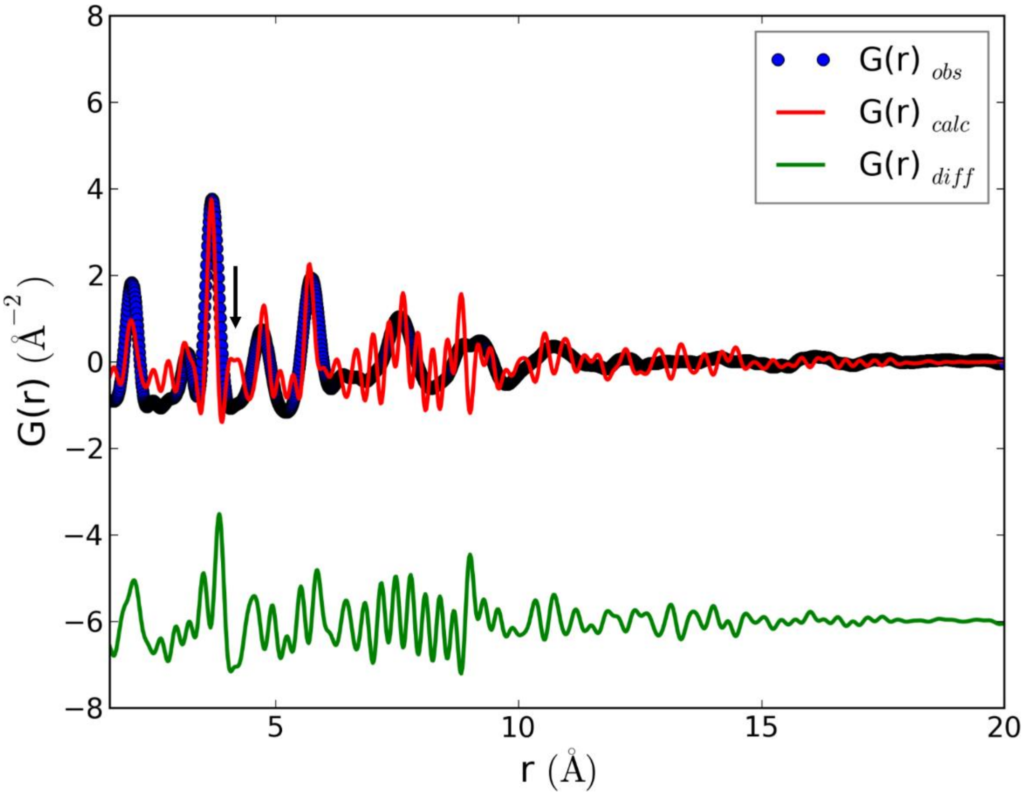

Figure 41 *- Comparison of experimental and calculated PDF of $Al_{0.57}Sn_{0.43}O_{1.71}$ calcined at 550°C modelled as SnO_2 nanoparticle.*

The PDF of the modelled nanostructure was obtained using sample specific and instrument dependent parameters such as finite size, Q_{damp} and Q_{max}. As it is seen in ***Figure 41***, the fit is not in good agreement due to different compositions. The first peak which gives the first nearest-neighbour pair of metal-oxygen atoms is slightly mismatched and around 4.2

Å an extra peak appears which belongs to the metal-oxygen and oxygen-oxygen pair correlations.

In order to obtain the $Al_{0.57}Sn_{0.43}O_{1.71}$ nanoparticle with correct stoichiometry, 57% Sn atoms were randomly replaced by Al atoms and 14.25% of oxygen was removed to maintain charge balance using the initial SnO_2 nanostructure.

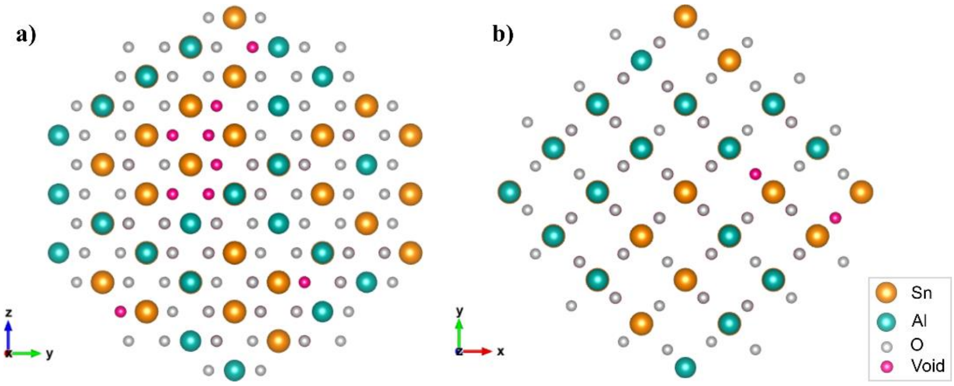

Figure 42 *- Crystal structure of $Al_{0.57}Sn_{0.43}O_{1.71}$ nanoparticle viewed along the a-axis (a) and the c-axis (b).*

After replacing the Sn atoms by Al atoms, the first peak is still mismatched. However, its intensity increased due to lower average number density and the extra peak around 4.2 Å is still visible (***Figure 43***). Additionally, there is a difference between the experimental and calculated width of the PDF peak at 3.7 Å which belongs to the metal-metal pairs and might be due local distortions around the metal atoms.

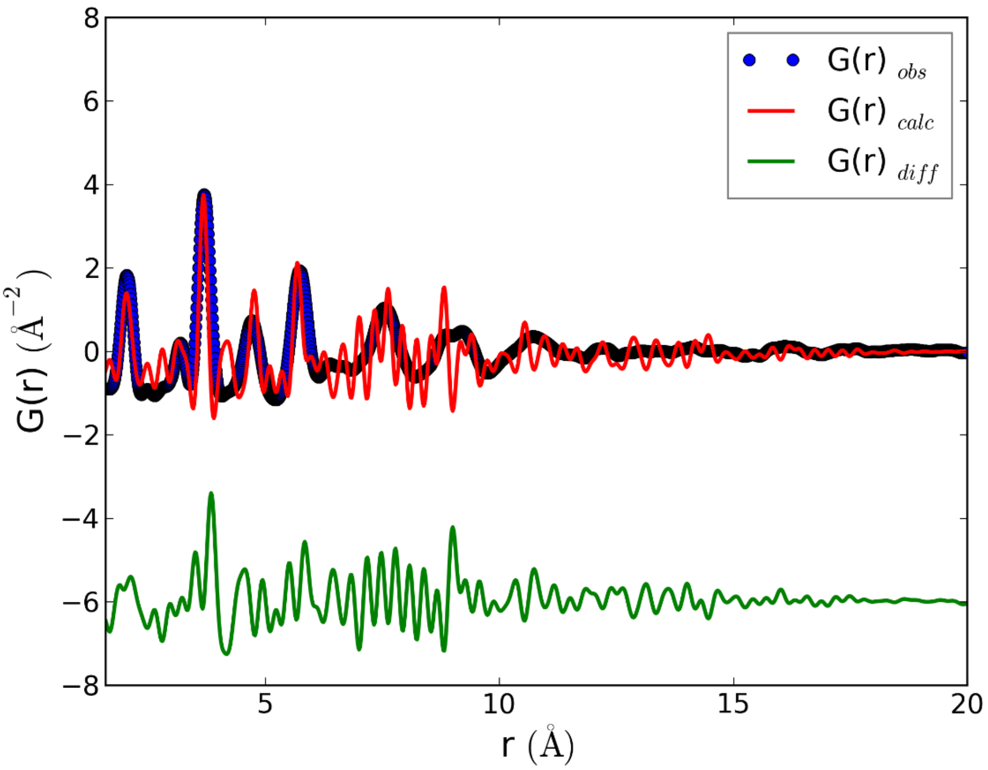

Figure 43 *- Comparison of experimental and calculated PDF of* $Al_{0.57}Sn_{0.43}O_{1.71}$ *nanoparticle.*

4.1.1.4.2. RMC Models

RMC modelling was applied in three steps using a structure model and the experimental PDF data. In a first step, aluminium and tin atoms were randomly swapped in each step of the RMC refinement with 25 iterations. In a second step, oxygen ions and oxygen vacancies were randomly swapped using the resulting structure model of the first step (***Figure 44***). In a third step, atoms were displaced within the nanoparticle using the resulting structure model of the second step.

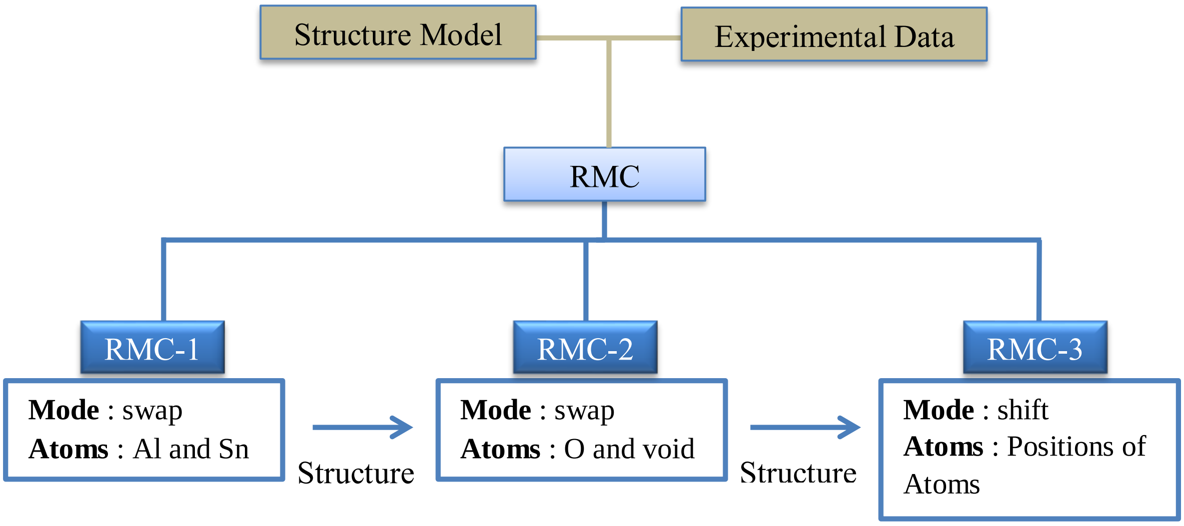

***Figure 44** – Process diagram of RMC modelling of $Al_{0.57}Sn_{0.43}O_{1.71}$.*

After swapping Al and Sn atoms in the structure, the initial goodness-of-fit parameter (χ^2) of 0.188 slightly decreased to 0.178 and the calculated intensity of the first peak matched better with the experimental data (***Figure 45***).

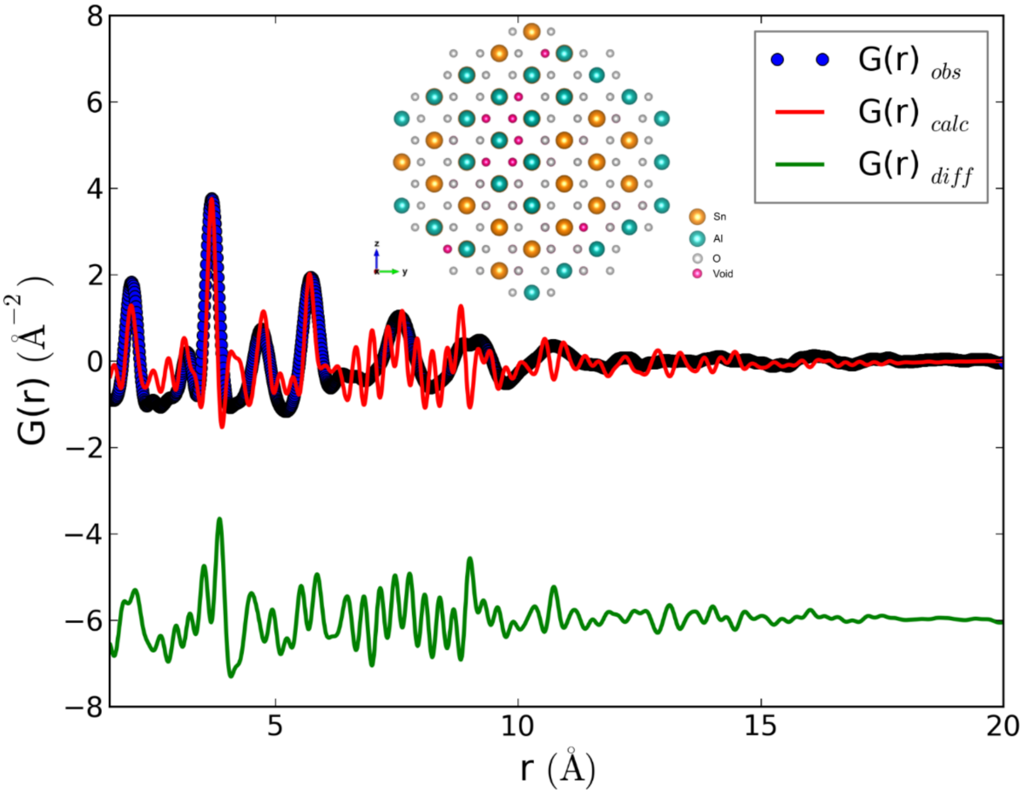

Figure 45 - RMC refinement after swapping of Al and Sn atoms.

The oxygen atoms and the corresponding vacancies within the structure were swapped using the resulting structure of RMC-1. Note that the algorithm treats oxygen vacancies (voids) as atoms which have zero scattering power. The χ^2 value of this RMC modelling again slightly decreased from 0.178 to 0.177. The comparison between the experimental and calculated PDF is shown in ***Figure 46***.

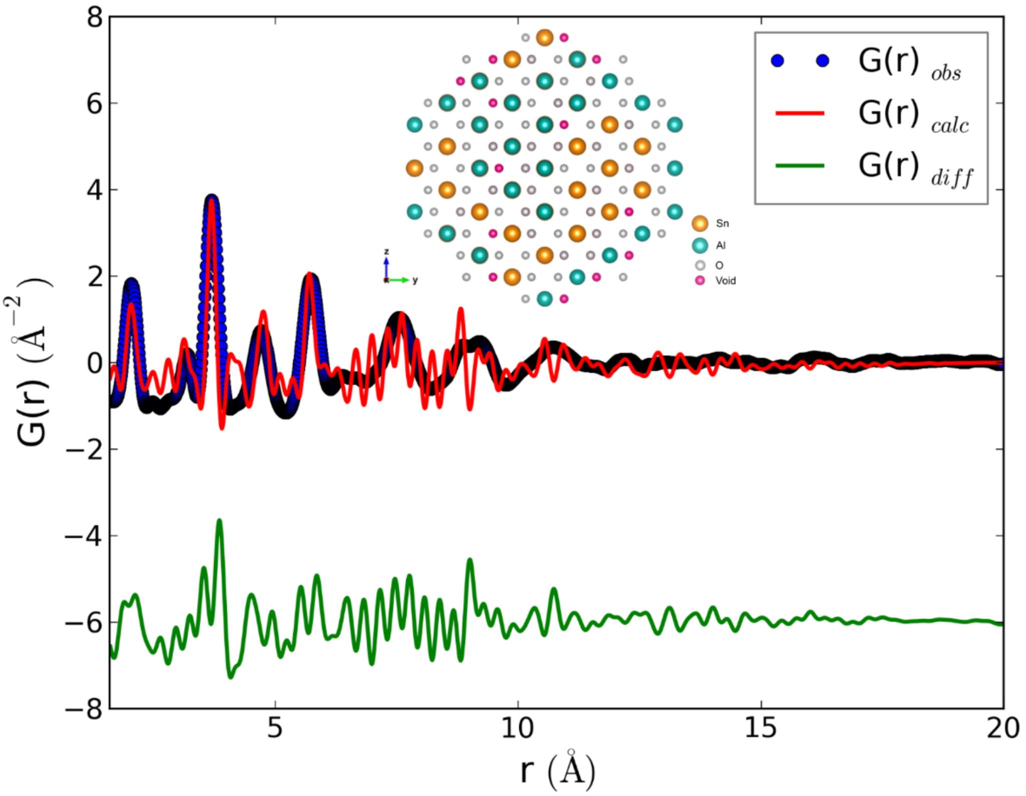

Figure 46 - *RMC refinement after swapping of O atoms and vacancies.*

In a third step, atoms were displaced within the crystal using the resulting structure model of the second step (RMC-2) with 500 iterations. In order to obtain a physically and chemically realistic structure, the maximum value for an atom displacement was constrained to 0.02, 0.02, 0.02 Å (x,y,z) for each selected atom in a single step. Additionally, the minimum bond lengths were constrained to 1.7 Å for metal (Al,Sn)-oxygen, 2.9 Å for metal-metal and 2.6 Å for oxygen-oxygen distances within the range of the PDF from 1.6 to 20 Å.

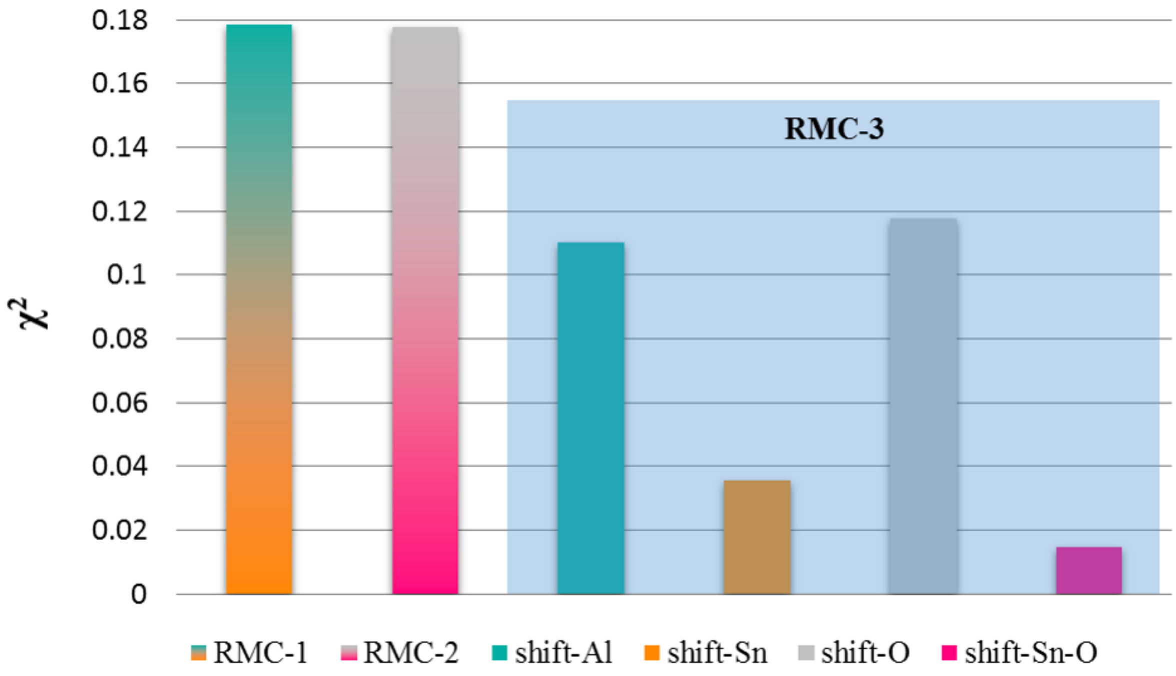

Figure 47 *- The goodness-of-fit for the different RMC refinement steps. RMC-1 is swapping Al and Sn ions. RMC-2 is swapping O ions and vacancies. RMC-3 is the refinement of selected atom positions.*

The goodness-of-fit parameter for each RMC refinement step is given in ***Figure 47***. In the third step of the RMC modelling (RMC-3), the positions of Al, Sn, O as well as both Sn and O atoms were refined individually to get a good fit. The simultaneous refinement of both Sn and O atoms resulted in the largest improvement of the fit. To check the stability of the final result, different RMC modelling routes were tried like;

- RMC-1, RMC-2, RMC-3 (with Sn and O positions), RMC-1 or
- RMC-1, RMC-2, RMC-3 (with Sn and O positions), RMC-2.

However, the same results were obtained at the end showing that Al substitution induces a local distortion around the Al and Sn atoms. The fact of a local distortion around Sn is supported by ^{119}Sn MAS NMR and Mössbauer spectroscopy [67]. The details of RMC-3 models are given in the sections below.

The PDF refinement in PDFGui results in a large atomic correlation parameter. Therefore, occupational correlations of atoms were investigated after RMC modelling in DISCUS. The occupational chemical correlations of the $Al_{0.57}Sn_{0.43}O_{1.71}$ nanoparticle in ***Figure 48*** and correlations of the RMC-1 and RMC-2 models are shown in ***Figure 49***. The correlations show the following terms:

if the correlation parameter (c_{ij}) is negative, i and j sites tend to be occupied by different atoms.

if the correlation parameter (c_{ij}) is positive, i and j sites tend to be occupied by the same atoms.

a zero value of c_{ij} describes a random distribution.

c_{ij} is the value of a parameter that is defined in a respective direction. c_{10} and c_{11} define <10> and <11> directions, respectively. The <10> direction has four symmetrical equivalents such as c_{10}, $c_{\bar{1}0}$, c_{01} and $c_{0\bar{1}}$.

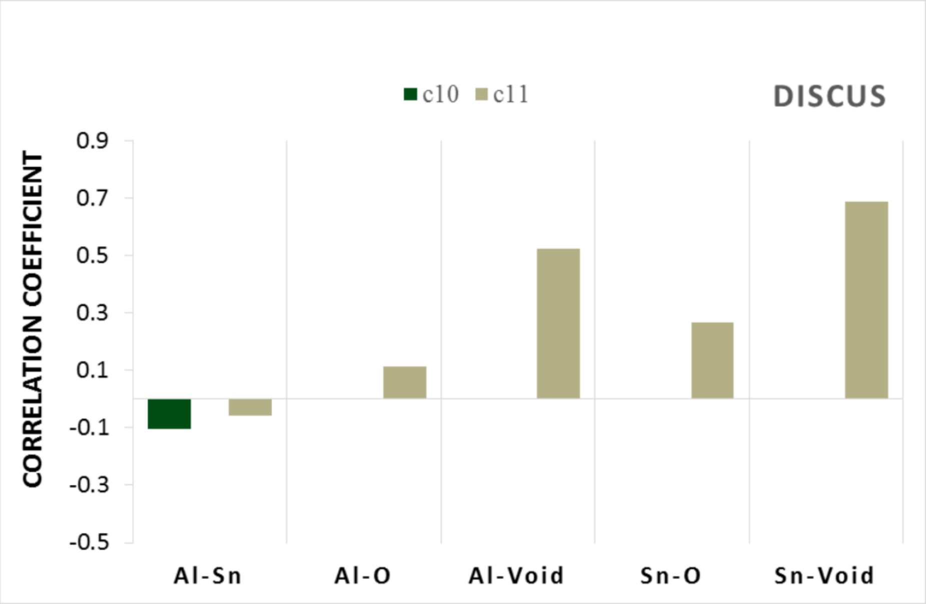

Figure 48 *- Occupational correlations in the initial structure of* $Al_{0.57}Sn_{0.43}O_{1.71}$ *nanoparticle from DISCUS after replacing.*

After swapping of Al and Sn atoms as in RMC-1, the correlation parameter between Al and Sn atoms increase along the <10> direction which indicates an ordering of the same type atoms (clustering). However, along the <11> direction, the correlation between Al and Sn atoms decreases to negative values, indicating that c_{11} is occupied by different types of atoms.

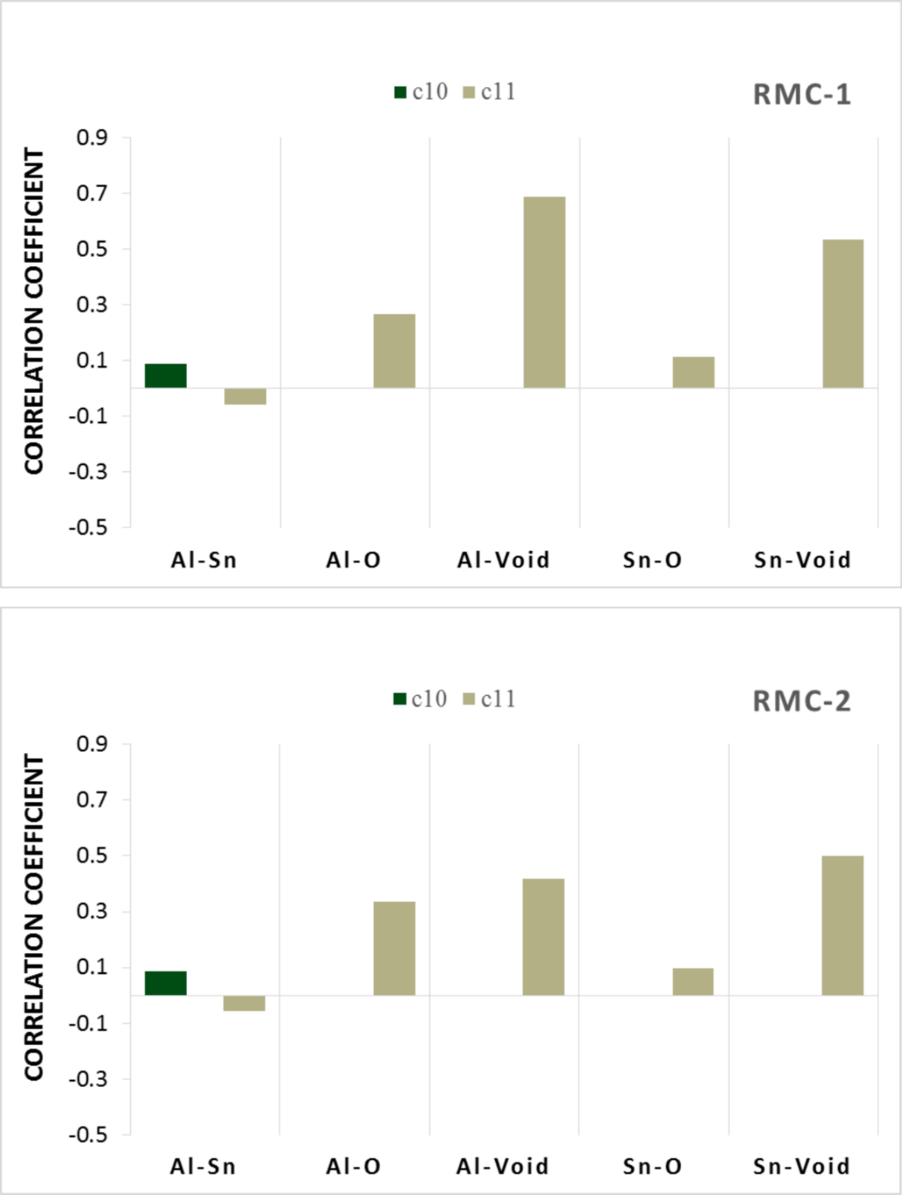

Figure 49 *- Occupational correlations of RMC-1 and RMC-2 models.*

The analysis of the occupational correlation of the RMC-2 model shows that the Sn-void and Al-void correlations decrease along the <11> direction.

4.1.1.4.2.1. RMC-3 shift-Al

After refining the positions of the Al atoms, the χ^2 value decreases from 0.177 to 0.011 (***Figure 50***). However, the width of the first calculated PDF peak is narrower than the observed one. Additionally, an extra peak can be seen at 4.2 Å and peaks around 9 Å are mismatched with the observed ones.

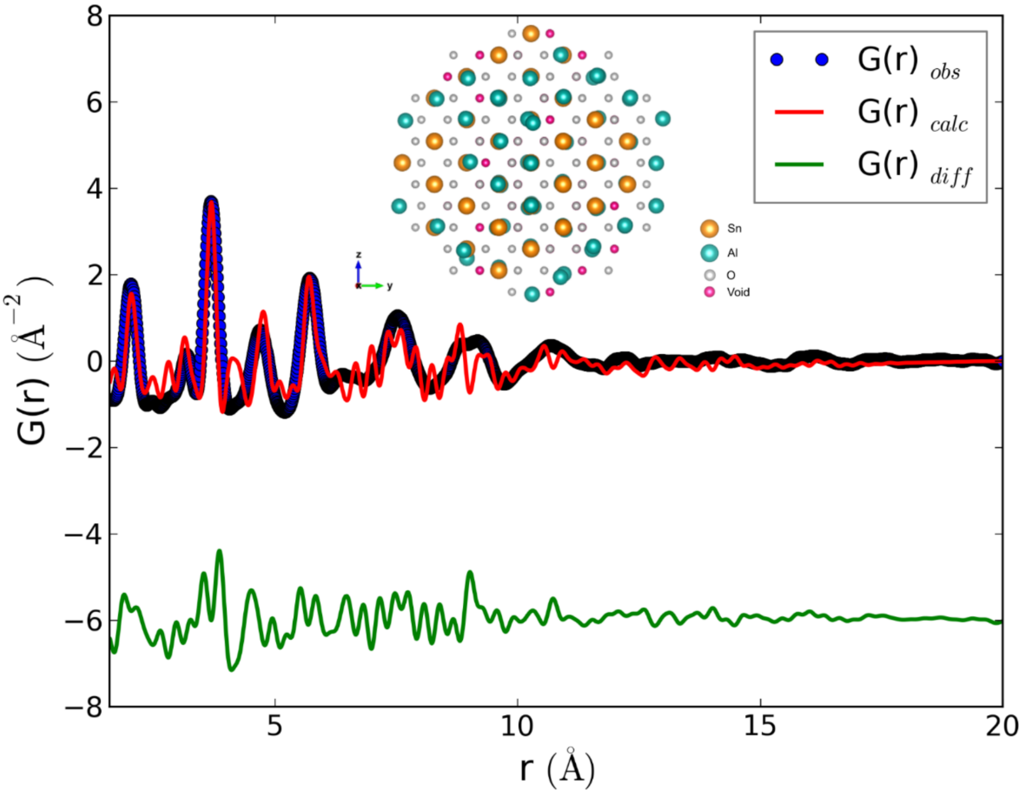

Figure 50 *- RMC refinement after refining the atomic position of the Al atoms.*

4.1.1.4.2.2. RMC-3 shift-Sn

The refinement of the positions of the Sn atoms reduces the χ^2 value from 0.177 to 0.035 (***Figure 51***). A comparison with the previous RMC-3 modelling with shifted Al atoms show that the fit is in fairly good agreement. On the other hand, there are some mismatches due to the metal-oxygen and oxygen-oxygen pairs.

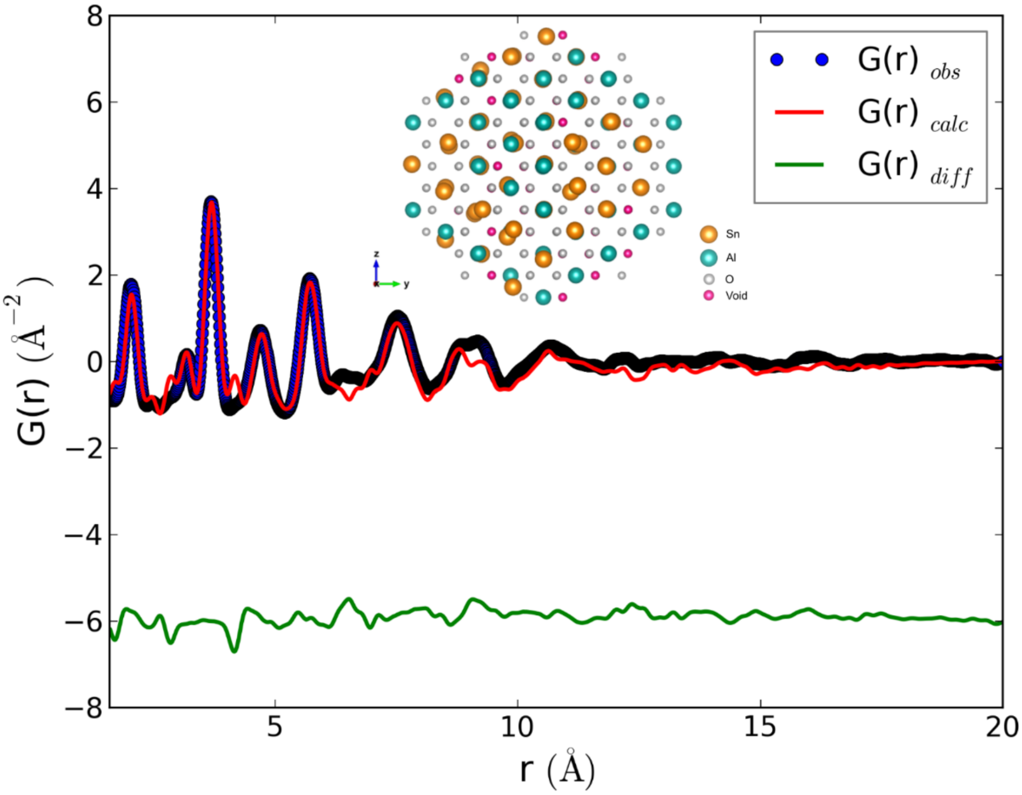

Figure 51 *- RMC refinement after refining the atomic position of the Sn atoms.*

4.1.1.4.2.3. RMC-3 shift-O

In this model, the O atoms were displaced within the nanoparticle and the χ^2 value decreases from 0.177 to 0.117. The refinement of the O atom positions demonstrates that the nanostructure has not only oxygen distortion but that also local distortions around the metals exist. This can be seen clearly in ***Figure 52***, particularly in the first peak which belongs to metal-oxygen pairs. Moreover, the calculated peak around 5.7 Å, which belongs to the metal-metal and oxygen-oxygen pairs has a higher intensity than the observed one. Additionally, some mismatched peaks around 9 Å can be seen clearly.

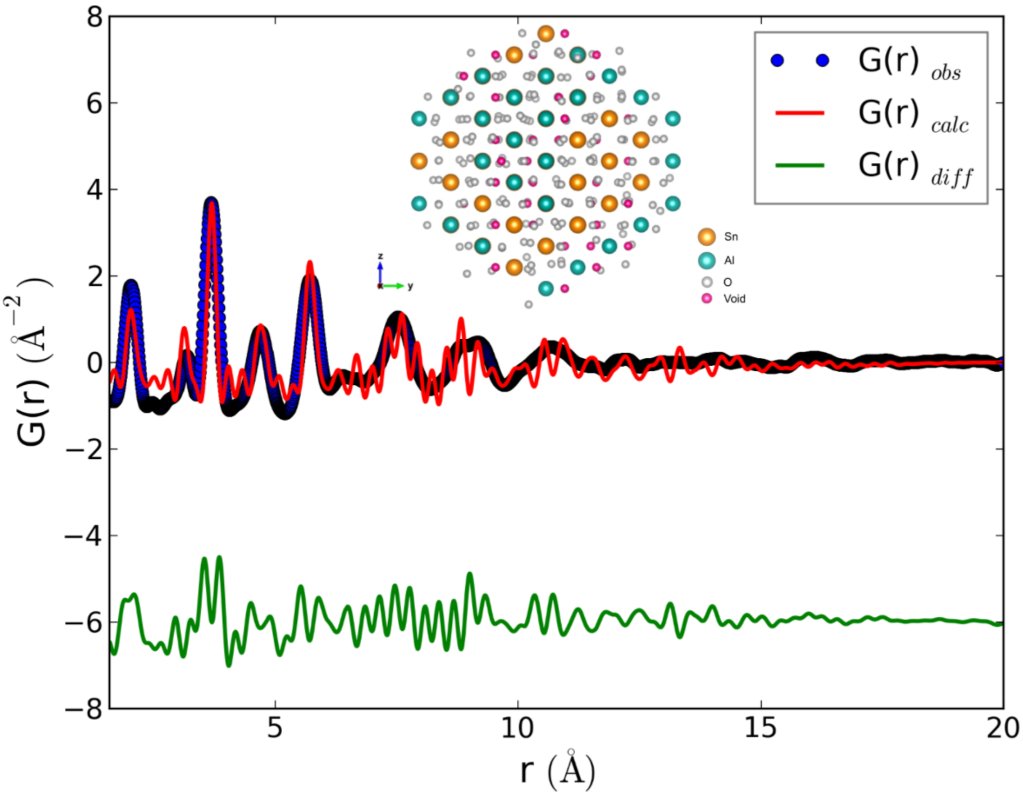

Figure 52 - *RMC refinement after refining the atomic position of O atoms.*

4.1.1.4.2.4. RMC-3 shift Sn and O

The simultaneous refinement of the Sn and O positions leads to a χ^2 value of 0.014 which is the best fit in all RMC models used. All peaks are matched in good agreement shown in ***Figure 53***.

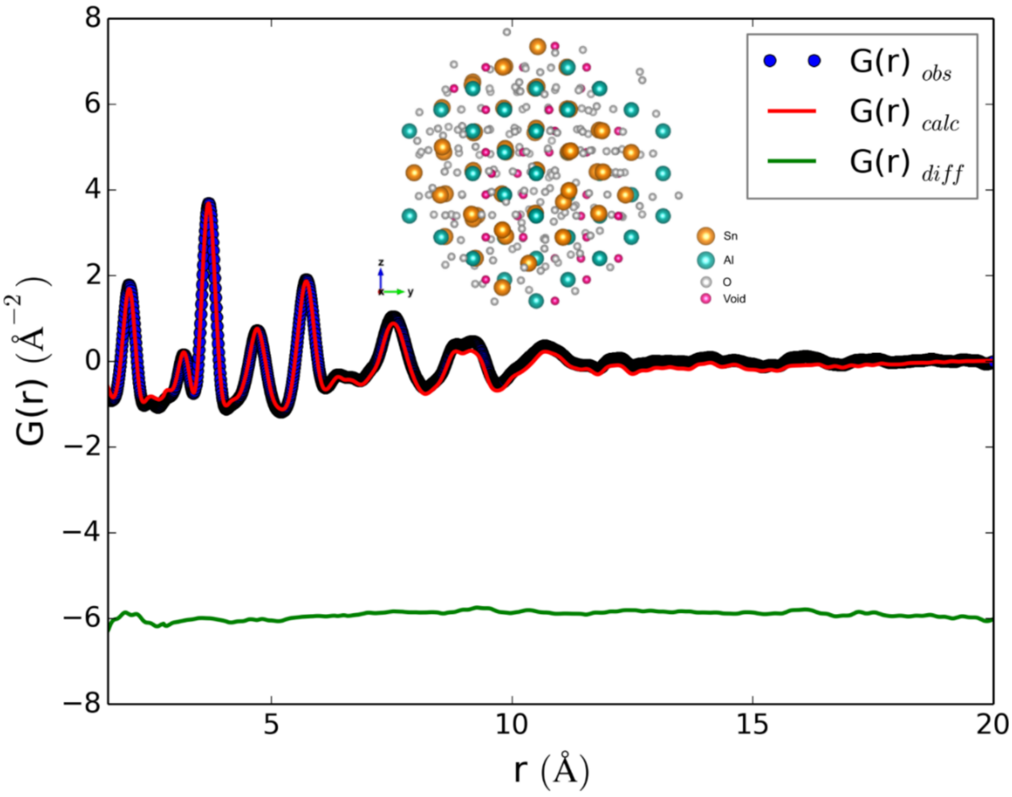

***Figure 53** - RMC refinement after refining the atomic position of Sn and O atoms.*

The total PDF is a weighted sum of the partial PDFs. For this system it is given as:

$$G_{\mathrm{AlSnO}}(r) = 9.13G_{\mathrm{Sn-Sn}} + 2.37G_{\mathrm{Al-Sn}}(r) + 1.46G_{\mathrm{Sn-O}}(r) + 0.62G_{\mathrm{Al-Al}}(r) + 0.38G_{\mathrm{Al-O}}(r) + 0.23G_{\mathrm{O-O}}(r) \tag{44}$$

where the weighting factor (Eq. 26) of each pair were obtained from the DISCUS simulation. The program PDFGui and DISCUS give the weighted partial PDFs. However, in the case of different scattering powers and concentrations, the weighted partial PDFs have to be divided by the respective weighting factors. So, the partial PDFs can be compared. The weight-independent partial PDFs are illustrated in ***Figure 54*** and ***Figure 55***.

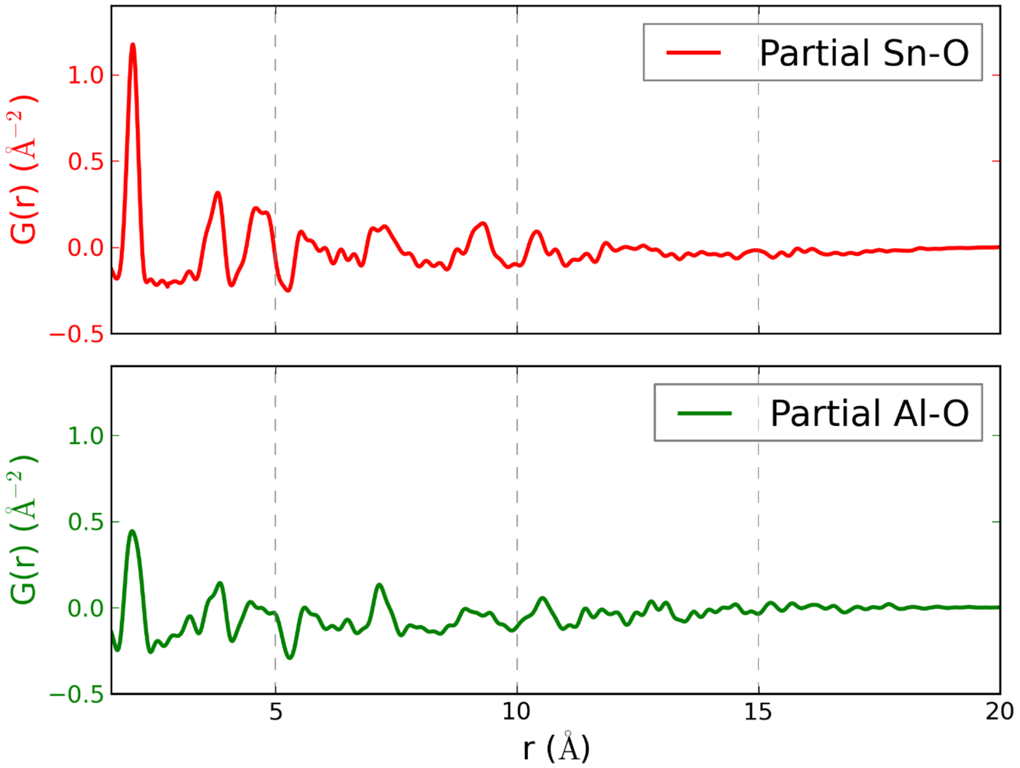

Figure 54 *- Weight-independent partial PDFs of the metal-oxygen pairs.*

In ***Figure 54***, the intensity of the first peak at ~2 Å of Sn-O is higher than that of Al-O showing a higher coordination number. This indicates that oxygen vacancies are mostly located around Al atoms. This result is consistent with ^{119}Sn MAS NMR data of Issac *et al.* [67]. ***Figure 55*** shows that the intensity of the peak at ~3.7 Å for Al-Al pairs is higher than that of Sn-Sn pairs, which points out a clustering of Al atoms in the nanoparticle.

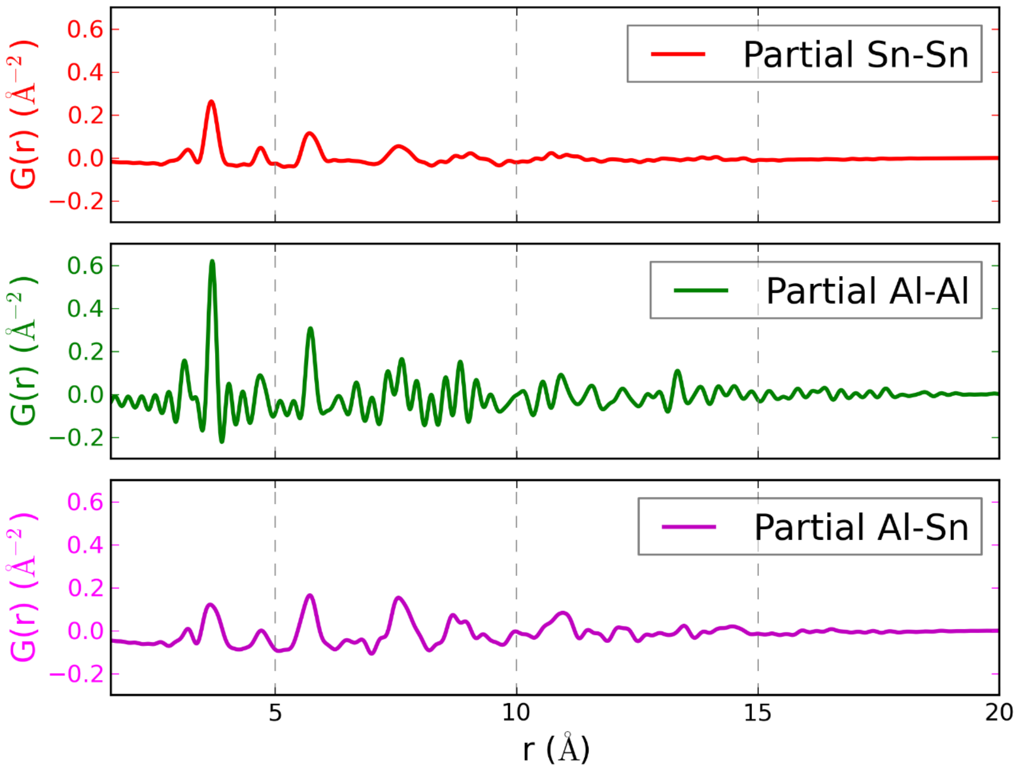

Figure 55 *- Weight-independent partial PDFs of the metal-metal pairs.*

The occupational correlations of the atoms after RMC modelling are shown in ***Figure 56***. Note that the <10> direction contains Al and Sn atoms and that the <11> direction contains Al, Sn and O atoms. After RMC modelling, the correlation parameter of the Al and Sn atoms reduced to negative values along the <10> direction which means that Al and Sn atoms are distributed with different types of atoms as a sequence of Al-Sn-Al-Sn *etc.*. However, they tend to be distributed with the same type of atoms along the <11> direction, in other words, they are partly ordered. The probability of having Al-Sn pairs and the corresponding correlation coefficient c_{10} are tabulated in ***Table 12***, where the probability of having Al-Sn pairs along the <10> direction is 73 % indicating distribution with different type of atoms. The occupational correlation parameter of Al-O is zero along the <11> direction which indicates that Al and O atoms are randomly distributed in this direction (***Figure 56***).

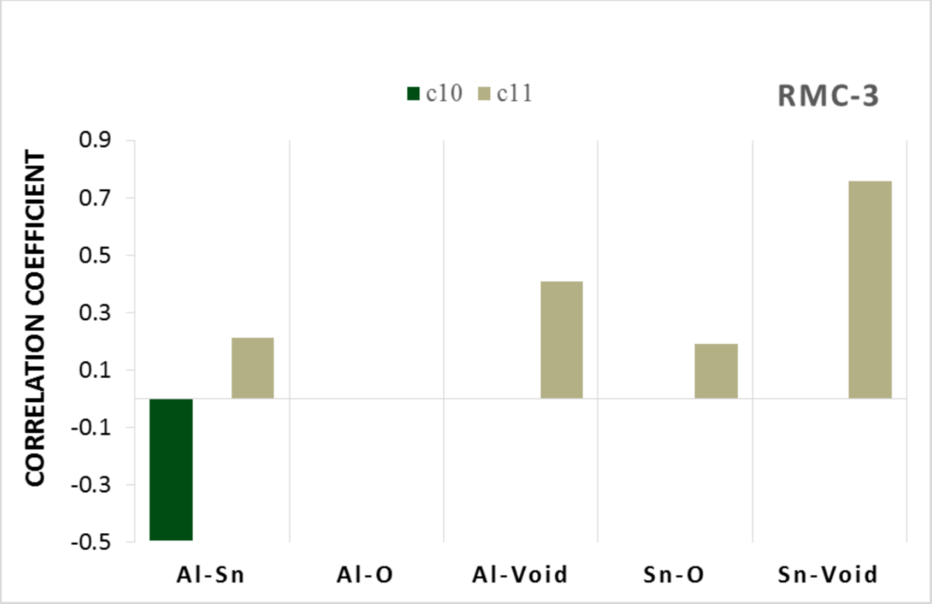

Figure 56 *- Occupational correlations of RMC-3 (refinement of the positons of Sn and O).*

Table 12 *– The probability and corresponding c_{10} of Al-Sn for RMC-2 and RMC-3.*

RMC type	**Al-Al (%)**	**Al-Sn (%)**	**Sn-Sn (%)**	**Correlation Coefficient**
RMC-2	15	42.5	42.5	0.09
RMC-3	20	73	7	-0.49

Additionally, the occupational correlation parameter of Sn-void of RMC-3 is slightly changed compared to that of RMC-2 along the <11> direction. The correlation of the Sn-void pairs increases from 0.5 to 0.76 due to the ordering of voids (***Table 13***).

Table 13 *– The probability and corresponding c_{11} of Sn-Void for RMC-2 and RMC-3.*

RMC type	**Sn-Sn (%)**	**Sn-Void (%)**	**Void-Void (%)**	**Correlation Coefficient**
RMC-2	37.50	25	37.50	0.5
RMC-3	35	12	53	0.76

In order to understand the local environment of the Al and Sn atoms, the first peaks of the weight-independent partial PDFs of Al-O and Sn-O were analysed in more detail (***Figure***

57). They were modelled with a Gaussian distribution. Egami & Billinge, 2003, explained that the PDF peaks actually consist of non-Gaussian distributions due to thermal and zero-point motion of the atoms and any static displacements from ideal position [8]. However, the deviation from a Gaussian is negligibly small. The width of the first PDF peak of Sn-O is narrower than that of Al-O. This observation is induced by local structural distortions on the octahedral site mostly around the Al atoms in comparison to the Sn atoms due to a structural relaxation (***Table 14***). In the ideal aristotype rutile structure of SnO_2, an octahedron has two short vertical and four long horizontal bonds. The area of the PDF peak is related to the coordination number. ***Figure 57*-a** shows that the number of long horizontal bonds is higher than that of the short vertical bonds. However, ***Figure 57*-b** shows the other way round, the number of short bonds is higher than the number of long bonds due to structural relaxation, which results in the fact that local distortions are mostly around the Al atoms. Moreover, the center of the individual peaks of Sn-O are consistent with the results of the small-box modelling (***Table 11***). However, the center of peak 2 of the two Al-O bonds shows a slightly higher r-value than in the small-box modelling (2.08921(1) Å) (as tabulated in ***Table 11***) due to the existence of more oxygen vacancies around Al which are not considered in the small-box modelling.

Table 14 *- Peak characteristics of the fitted first peak belonging to the Al-O and Sn-O pairs of the weight-independent partial PDFs.*

	Al-O		**Sn-O**	
	Peak 1	Peak 2	Peak 1	Peak 2
Peak Center (Å)	1.97	2.16	1.97	2.08
Peak Area	0.15	0.11	0.15	0.20
Area Ratio (%)	58	42	42	58
FWHM (Å)	0.23	0.22	0.19	0.2

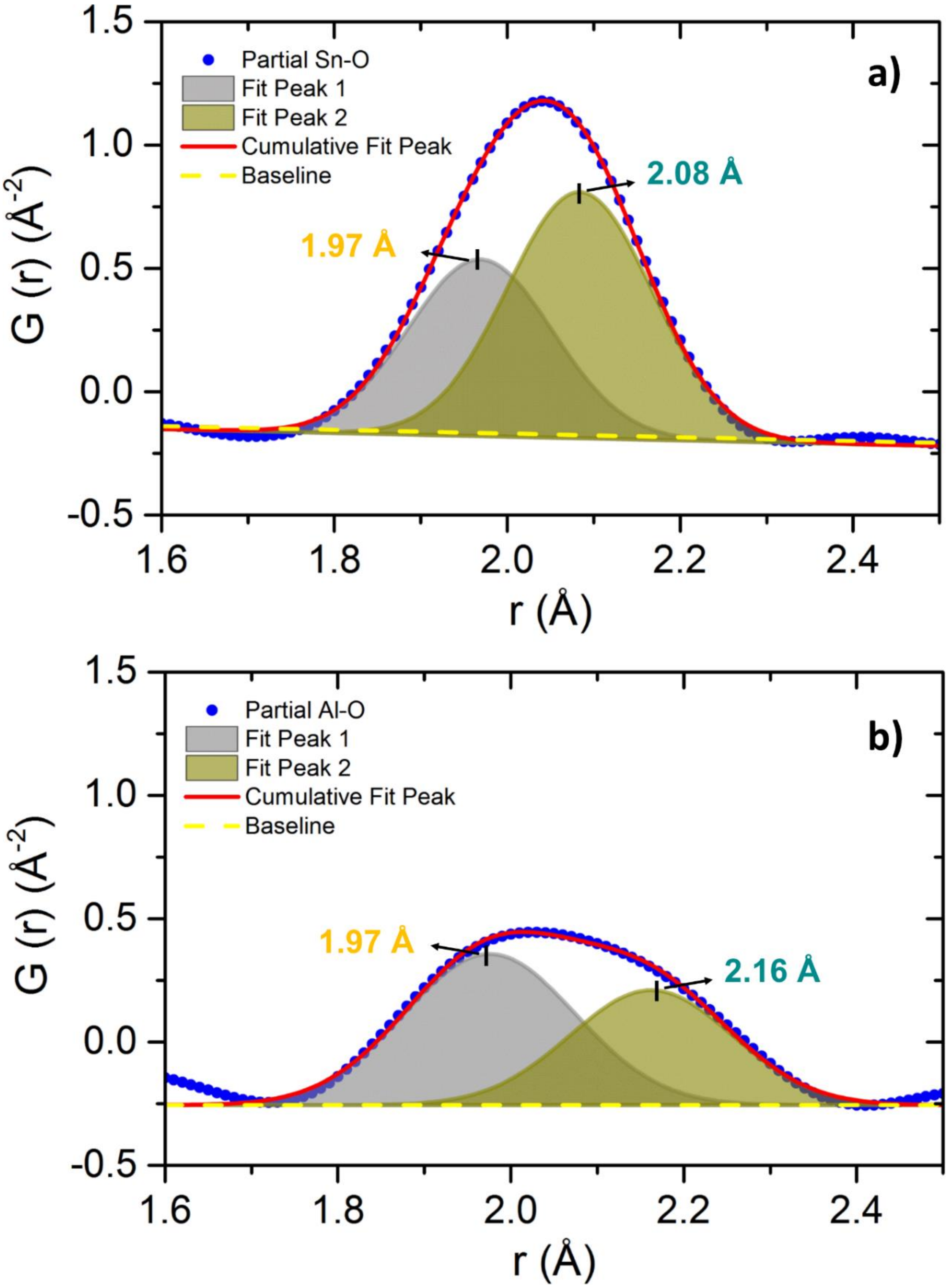

Figure 57 *- Gaussian fits of the first peaks of the weight-independent partial PDFs belonging to a) Sn-O and b) Al-O. The baselines are related to the average number density of scatterers.*

4.1.2. $Al_{0.57}Sn_{0.43}O_{1.71}$ calcined at 40ºC

4.1.2.1. Rietveld Analysis

The refinement of the model and structure parameters based on the synchrotron diffraction pattern is shown in ***Figure 58***. The micro-strain analysis resulted in an average crystallite size of 11 (±2) Å. The first neighbour distances of metal-oxygen (Al/Sn-O) are 2.01Å and 2.09 Å in a unit cell of 4.75(1) Å (a=b) 3.191(8) Å (c) as tabulated in ***Table 15***.

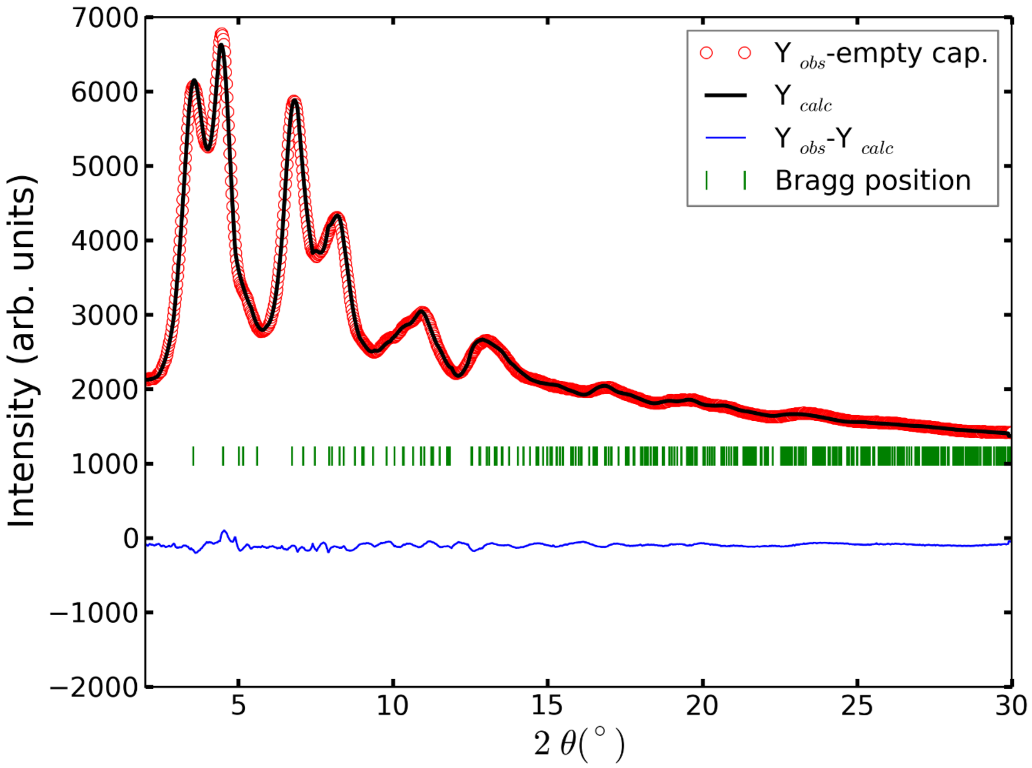

Figure 58 *- Synchrotron diffraction pattern of* $Al_{0.57}Sn_{0.43}O_{1.71}$ *nanoparticles measured in a 0.5 mm capillary at 0.2079 Å.*

Table 15 - Rietveld results of $Al_{0.57}Sn_{0.43}O_{1.71}$ nanoparticles (calcined at 40°C).

Unit cell parameters	a=b=4.75(1) Å and c=3.191(8) Å
Temperature parameters	Al=Sn=0.6(3) $Å^2$ and O=1.99(±1.08) $Å^2$
Metal-Oxygen distances*	2.01 Å and 2.09 Å
Average crystallite size	11 (±2) Å

*Note that bond lengths from Rietveld method represent the distances between the average atomic positions

4.1.2.2. Small-Box Modelling

The PDF refinement in PDFGui is given in ***Figure 59*** and R_{wp} is 33.9 %.

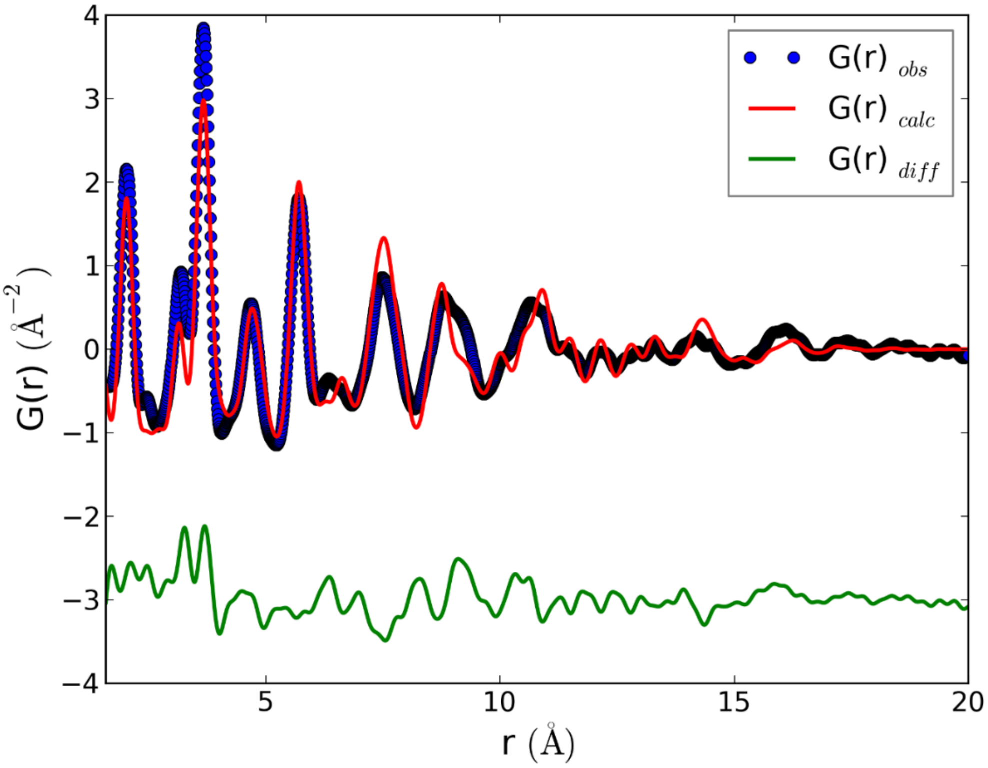

Figure 59 - *PDF refinement of $Al_{0.57}Sn_{0.43}O_{1.71}$* calcined at 40°C.

The comparison of results between PDF and Rietveld refinement are listed in ***Table 16***. The cell parameters of $Al_{0.57}Sn_{0.43}O_{1.71}$ (4.69 Å, 4.69 Å, 3.15 Å) from the PDF refinement are slightly different than that of the Rietveld refinement (4.75 Å, 4.75 Å, 3.19 Å) due to the systematic offset in the cell parameter. The average crystallite size from the PDF refinement is 11 (±2) Å.

Table 16 *- Refinement results from both the PDF and the Rietveld analysis for $Al_{0.57}Sn_{0.43}O_{1.71}$ calcined at 40°C.*

	PDF	**Rietveld**
Atom Distances (Å)		
Sn-O/Al-O	1.96092(2)	2.01
Sn-O/Al-O	2.07721(2)	2.09
O-O	2.85657(3)	2.90
Cell Parameters (Å)		
a=b	4.690420(5)	4.75(1)
c	3.147600(6)	3.191(8)

After PDF refinement, the weighted partial PDFs were extracted and are shown in ***Figure 60***. The first PDF peak is the nearest neighbour metal-oxygen pair. The first nearest neighbour of oxygen-oxygen shows up around 2.9 Å. The PDF refinement resulted in a large atomic correlation parameter (3.55).

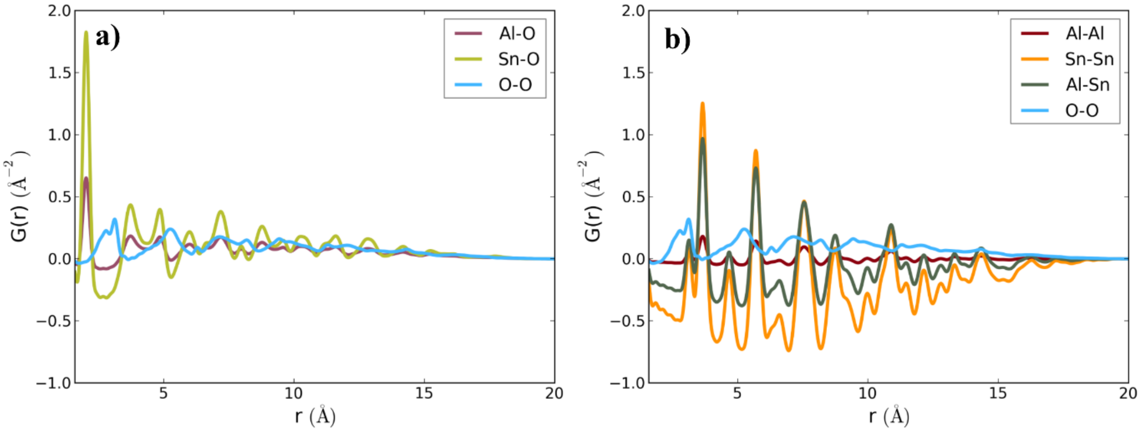

Figure 60 *- Partial PDFs of $Al_{0.57}Sn_{0.43}O_{1.71}$ calcined at 40°C.*

4.1.2.3. Big-Box Modelling

The local structure of $Al_{0.57}Sn_{0.43}O_{1.71}$ calcined at 40°C was investigated by using the big-box modelling similar to the nanoparticles calcined at 550°C. First, the nanoparticle was modelled according to the stoichiometry and then the structure was solved using the RMC modelling.

4.1.2.3.1. Nanoparticle Modelling

The aristotype rutile structure of SnO_2 was used for modelling and then 0.57 % of Sn was substituted by Al. PDF comparison of the modelled nanoparticle of 20 Å in diameter is shown in ***Figure 61***.

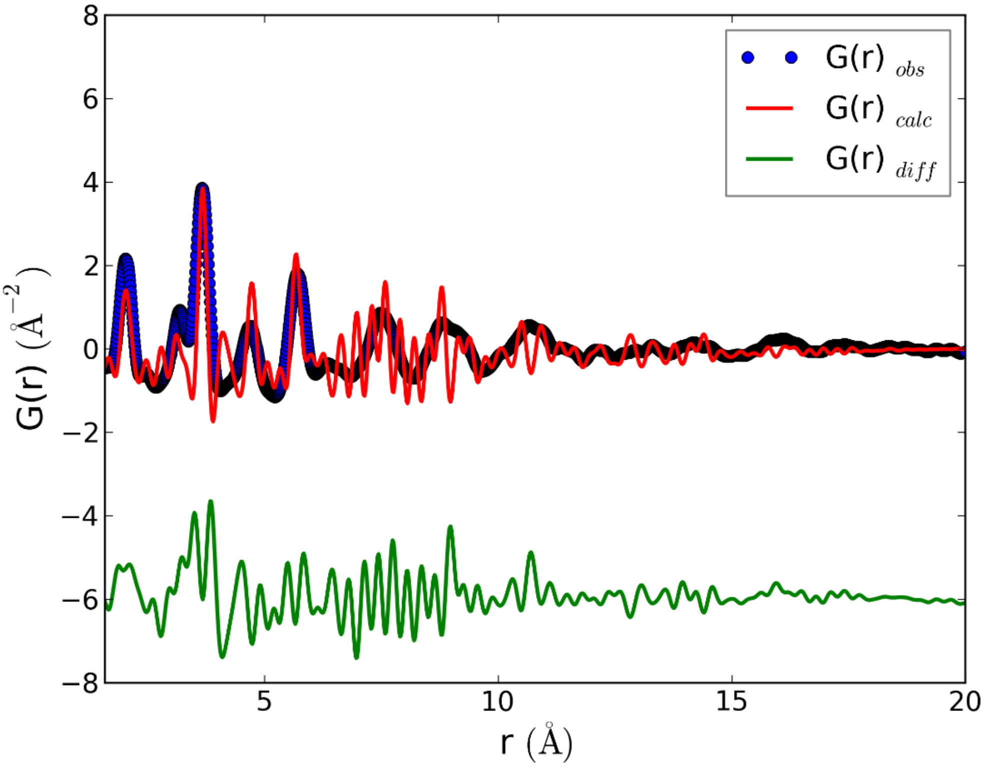

Figure 61 *- Comparison of experimental and calculated PDF of* $Al_{0.57}Sn_{0.43}O_{1.71}$ *nanoparticle.*

4.1.2.3.2. RMC Models

The RMC modelling was applied using the structure model of the $Al_{0.57}Sn_{0.43}O_{1.71}$ and the experimental PDF data. The modelling was performed in three steps as explained in section of 4.1.1.4.2. First, Al and Sn atoms in the structure were swapped (RMC-1). The goodness-of-fit parameter of 0.21 slightly decreased to 0.20.

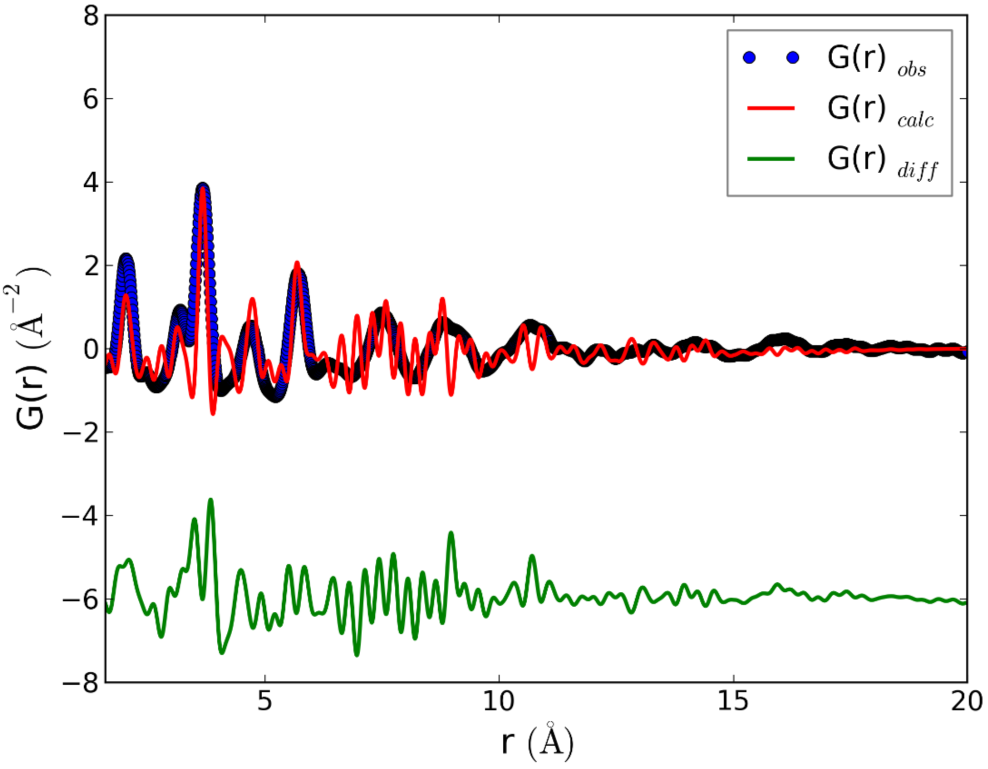

Figure 62 *– RMC refinement after swapping of Al and Sn atoms.*

In a second step, oxygen atoms and its vacancies within the structure were swapped using the resulting structure of RMC-1. This swapping slightly improved the χ^2 value (0.196). The comparison between experimental and calculated PDF after RMC-2 is illustrated in ***Figure 63***.

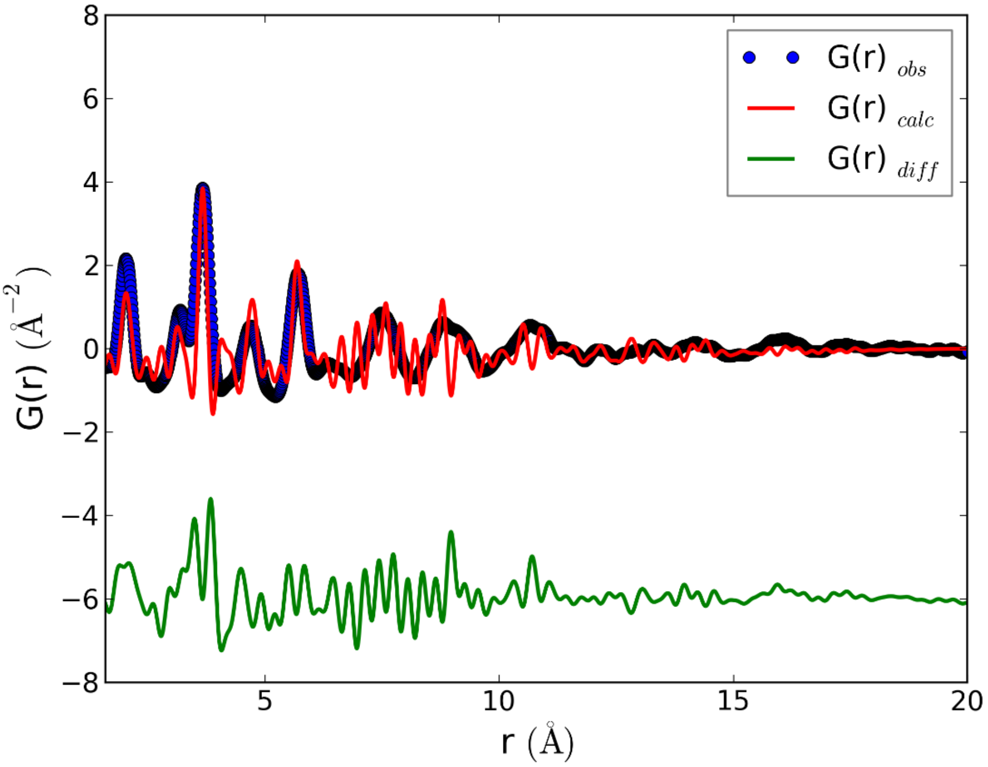

***Figure 63** – RMC refinement after swapping O and vacancies atoms.*

In a third step, to minimize the difference between experimental and calculated PDFs, atoms were displaced within the crystal with 500 iterations. The PDFs of the structure were analysed within a range of 1.6 to 20 Å.

The goodness-of-fit parameter for each RMC refinement step is given ***Figure 64***. A good fit was obtained with the refinement of only Sn atoms, which exhibits the local distortion around Sn. However, the largest improvement of the fit was obtained in the simultaneous refinement of Sn and O atoms.

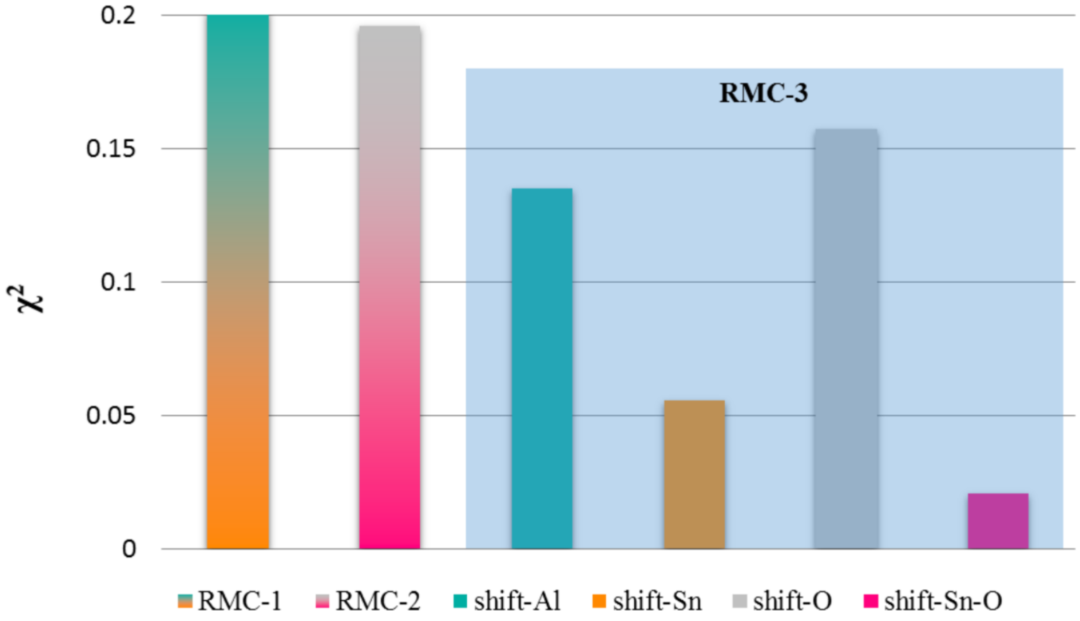

Figure 64 *- The goodness-of-fit for each RMC refinement.*

To understand which kind of atomic correlation exists in the nanoparticle, occupational correlations of atoms were investigated after RMC modelling. The occupational correlation parameters from Discus after RMC-1 and RMC-2 modelling of the $Al_{0.57}Sn_{0.43}O_{1.71}$ nanoparticle calcined at 40°C are given ***Figure 65*** and ***Figure 66***.

Figure 65 *- Occupation correlation of $Al_{0.57}Sn_{0.43}O_{1.71}$ nanoparticle calcined at 40°C.*

After simulation of the nanoparticle, the correlation coefficient of Al and Sn atoms is positive along the <10> direction, in other words they are partly ordered. After application of the RMC-1 and RMC-2 models, the correlation parameter is negative which reveals in this case alternating of atoms along the <10> direction. However, the correlation coefficients of other atom pairs along the <11> direction are also positive. This indicates that the ordering occurs along the <11> direction (***Figure 66***).

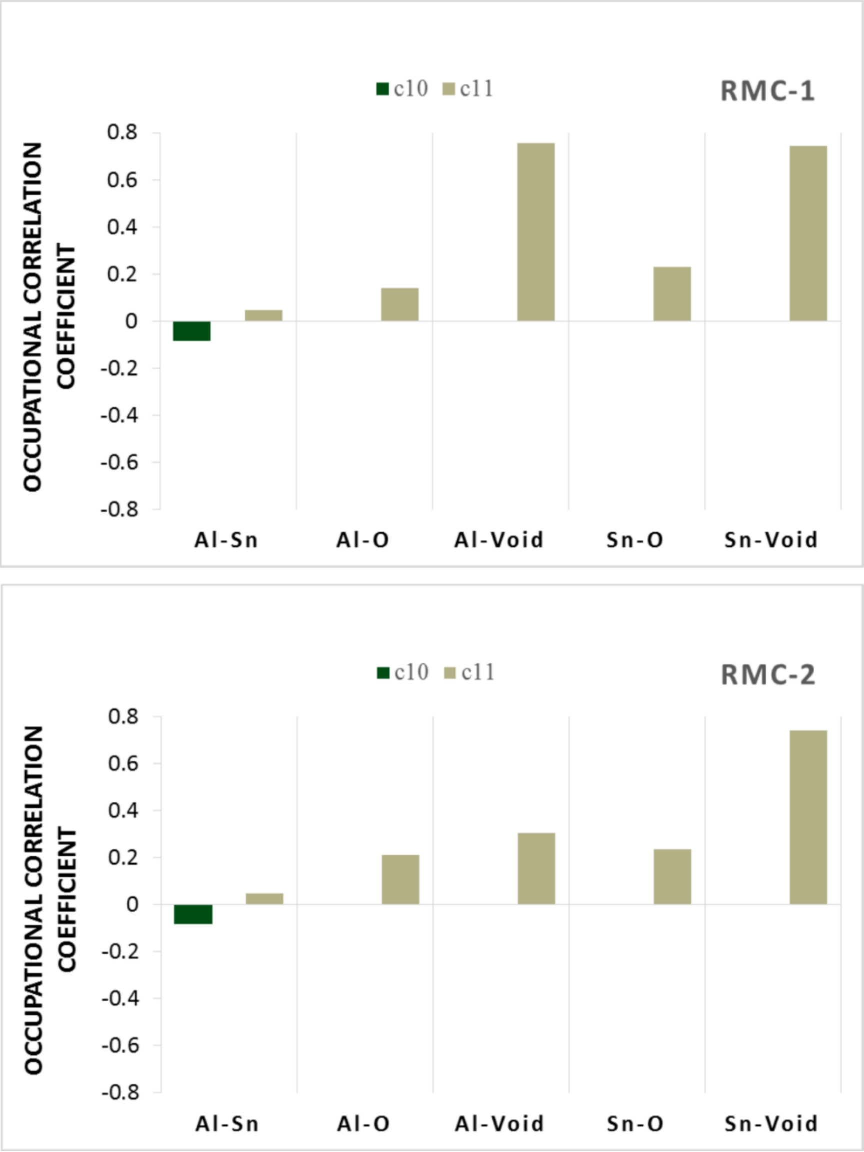

***Figure 66** - Occupational correlations of RMC-1 and RMC-2 models.*

4.1.2.3.2.1. RMC-3 shift-Al

The initial χ^2 value after RMC-2 is 0.21 but after displacement of the Al atom positions χ^2 reduced to 0.202. The fit is slightly improved. The first peak and the peak at 3.18 Å in particular are mismatched. The calculated peak positions are different and their intensities are lower than the observed ones.

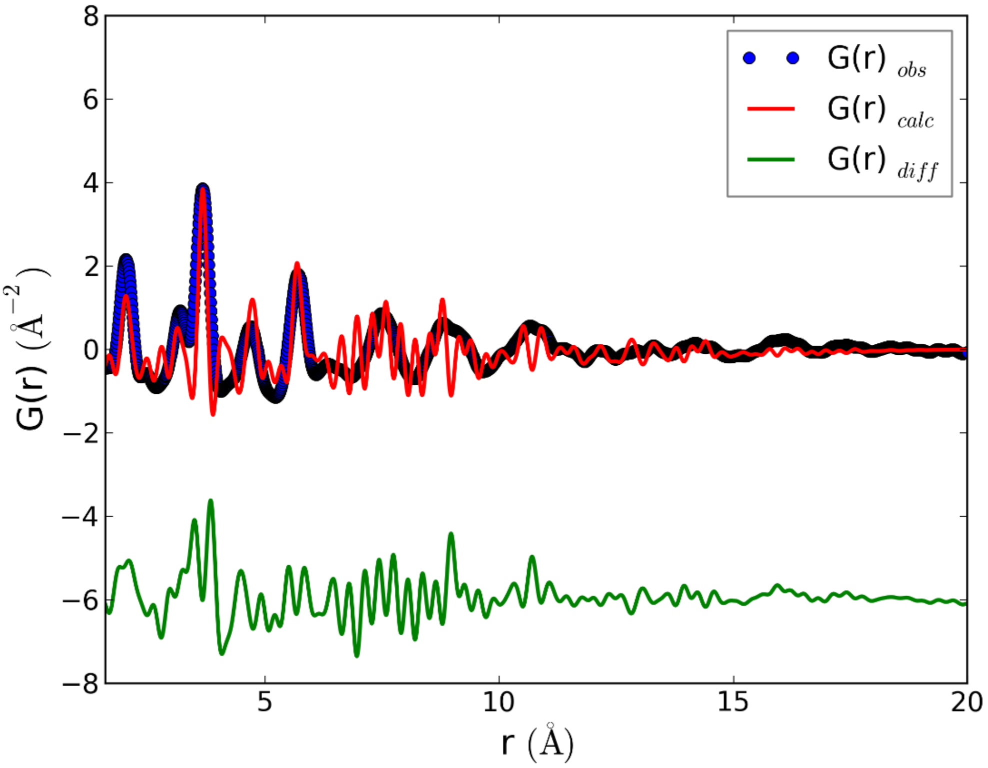

Figure 67 *- RMC refinement of $Al_{0.57}Sn_{0.43}O_{1.71}$ calcined at 40°C after refining the atomic position of Al atoms.*

4.1.2.3.2.2. RMC-3 shift-Sn

Using the resulting structure model of the RMC-2, Sn atoms were displaced and the χ^2 value decreased to 0.196. After the displacement of Sn atoms, the fit is still not in good agreement (***Figure 68***).

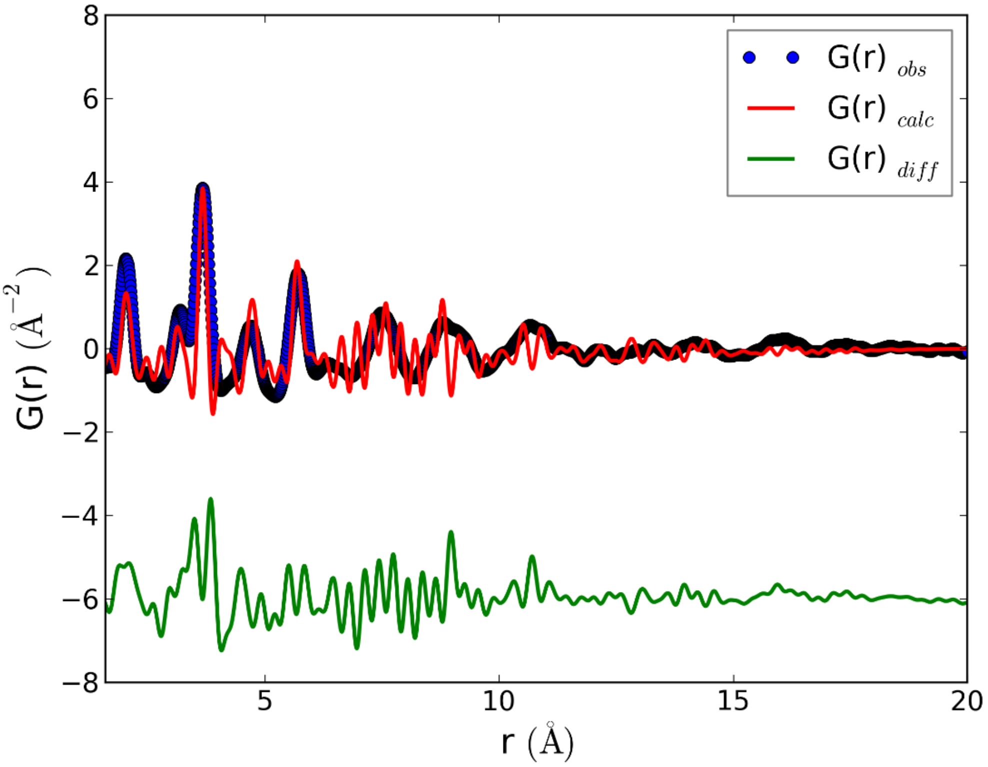

Figure 68 *- RMC refinement of* $Al_{0.57}Sn_{0.43}O_{1.71}$ *calcined at 40°C after refining the atomic position of Sn atoms.*

4.1.2.3.2.3. RMC-3 shift-O

The nanoparticle has 196 oxygen atoms. Despite the many refined parameters (196*3=588 parameters), the PDF peaks are still mismatched after the refinement of the O atom positions. The χ^2 value is 0.157 (***Figure 69***). The experimental and calculated PDF peaks of the nearest neighbour of metal-oxygen and metal-metal atom pairs notably don´t match well.

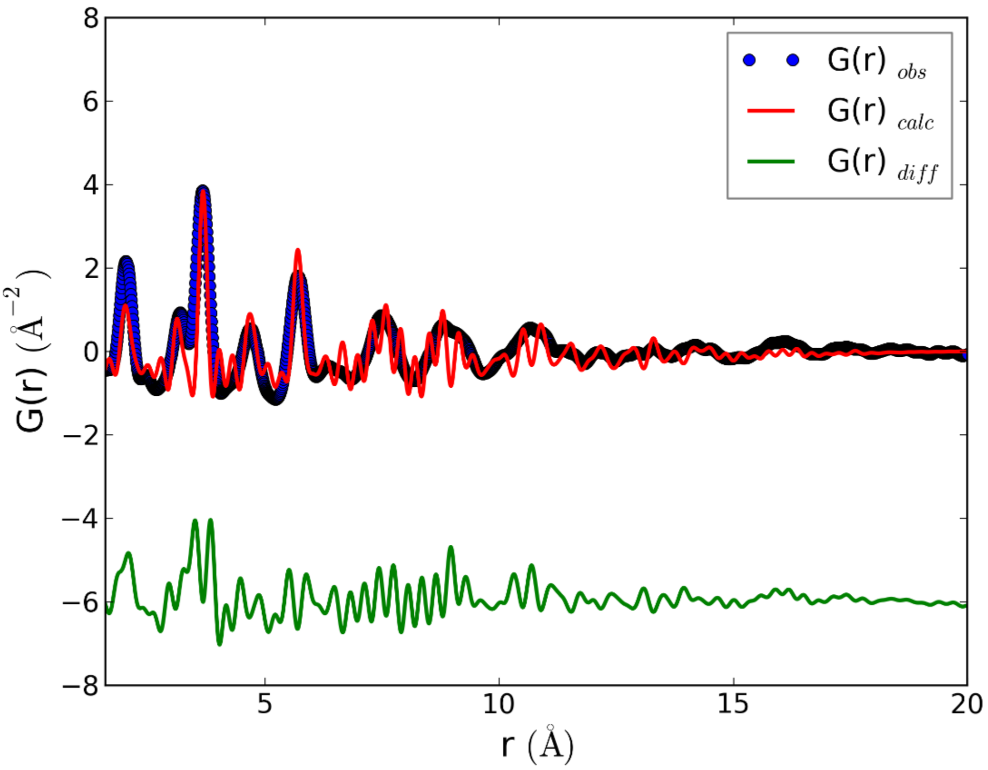

Figure 69 *- RMC refinement of $Al_{0.57}Sn_{0.43}O_{1.71}$ calcined at 40°C after refining the atomic position of O atoms.*

4.1.2.3.2.4. RMC-3 shift-Sn and O

The best fit was obtained after displacement of the Sn and O atom positions simultaneously. The experimental and calculated PDF peaks match well and the χ^2 value of the RMC-3 model decreased to 0.021 (***Figure 70***). After RMC-3 refinement, weight-independent partial PDFs of metal-oxygen and metal-metal pairs were extracted and are illustrated in ***Figure 71*** and ***Figure 72***, simultaneously.

In ***Figure 71***, the intensity of the first peak of Sn-O is higher than that of Al-O, which is a result of the oxygen vacancies around the Al atoms. The width of the first peak of the Al-O pairs is wider than that of Sn-O due to the occurrence of local distortions and oxygen vacancies around the Al atoms.

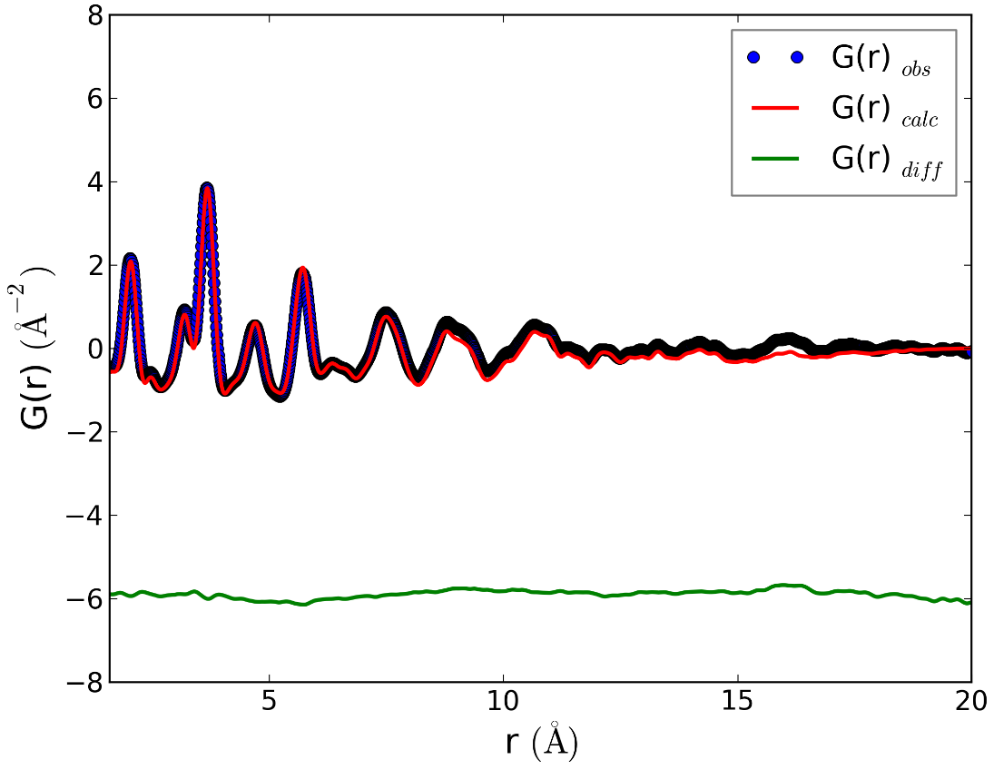

Figure 70 - *RMC refinement after refining the atomic position of Sn and O atoms.*

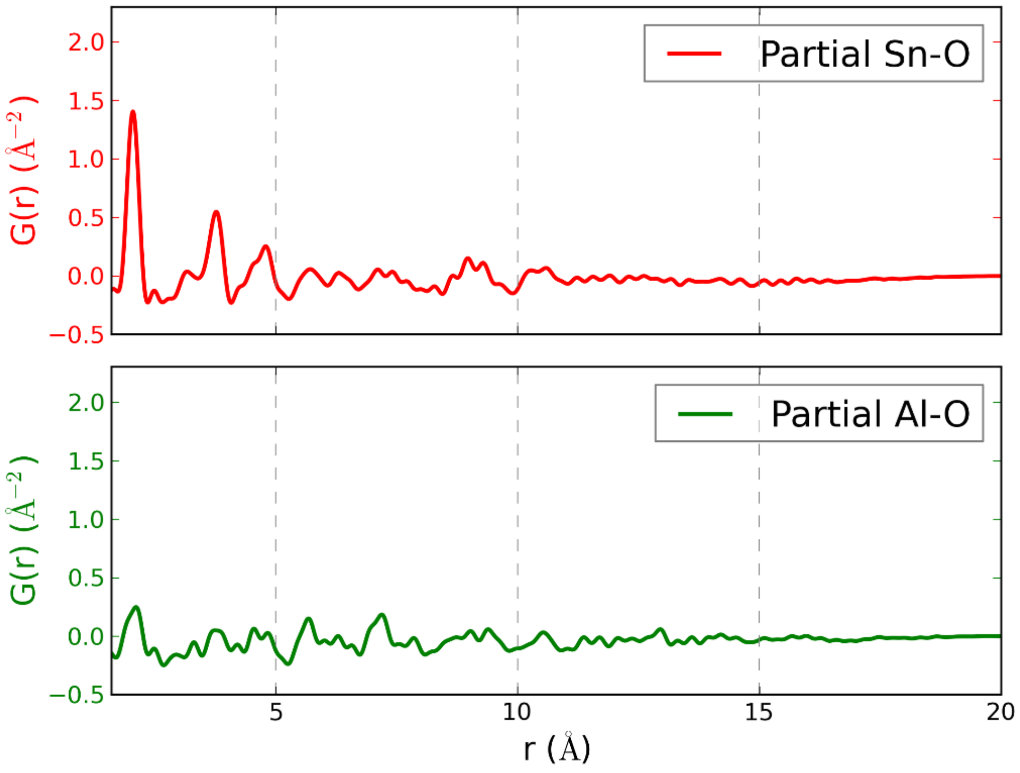

Figure 71 - *Weight-independent partial PDFs of metal-oxygen pairs.*

By comparing the first and second peaks of the metal-metal pairs it can be seen that the intensity of the Al-Al pairs is higher than that of others. This indicates a clustering of Al atoms in the nanoparticles.

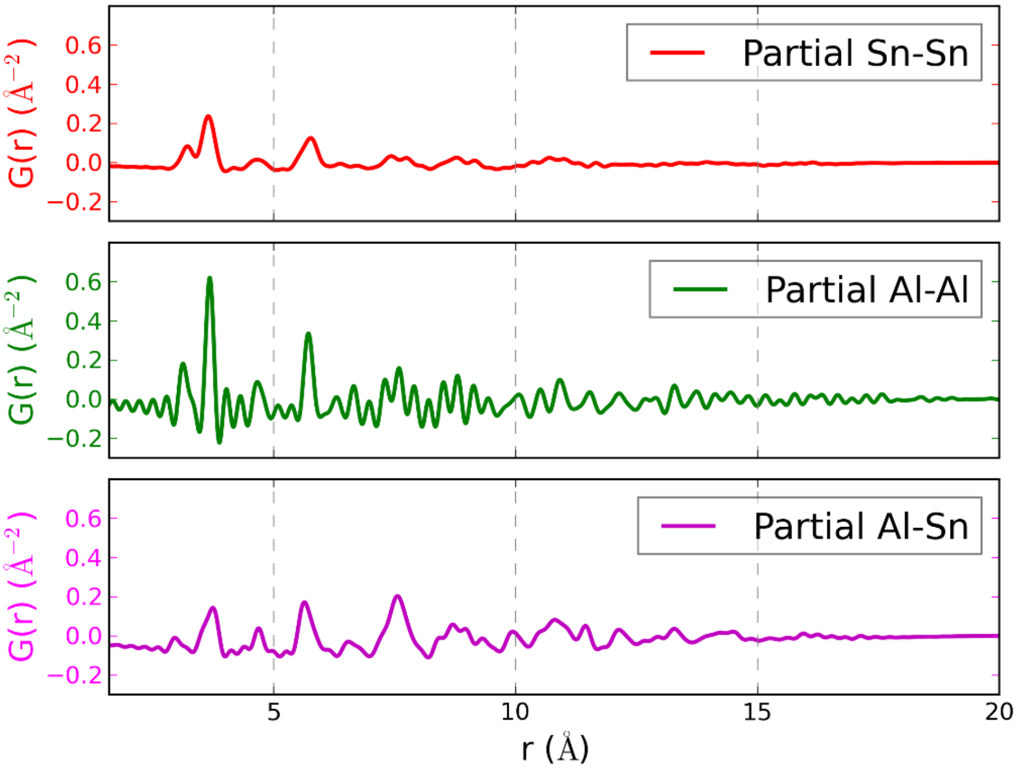

Figure 72 - *Weight-independent partial PDFs of metal-metal pairs.*

The occupational correlations of the atoms after application of the RMC-3 model were analysed. The occupational correlations of atom pairs are shown in ***Figure 73*** and all correlation coefficients are negative. For Al-Sn pairs the coefficient is negative in the <10> direction where the Al and Sn atoms tend to be occupied by different atom types. More information about the individual probabilities of Al-Sn pairs along the <10> direction is given in ***Table 17***. The probability of having Al-Sn pairs is 67%.

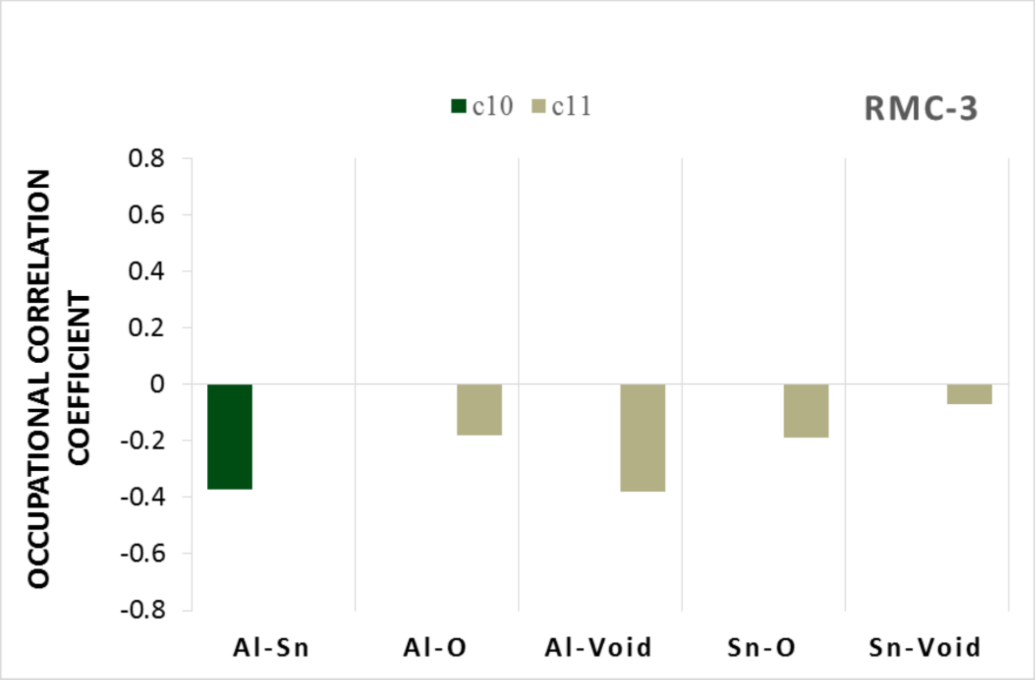

Figure 73 *- Occupational correlations of RMC-3 model.*

Table 17 *– The probability and corresponding c_{10} of Al-Sn for RMC-2 and RMC-3.*

RMC type	Al-Al (%)	Al-Sn (%)	Sn-Sn (%)	Correlation Coefficient
RMC-2	27	54	19	-0.08
RMC-3	25	67	8	-0.37

The first peaks of the weight-independent partial PDFs belonging to the Sn-O and Al-O pairs were analysed using a Gaussian fit ***Figure 74***. The width of the first PDF peak of Sn-O is narrower than that of Al-O. This is caused by local structural distortions on the octahedral site around the Al atoms. In ***Figure 74*****-a,** the PDF peak (Sn-O) consists of two peaks having four short horizontal and two long vertical bonds. However, the peak (Al-O) has two short vertical and four long horizontal bonds in ***Figure 74*****-b.** The peak characteristics of the fitted first peaks of the weight-independent partial PDFs are tabulated in ***Table 20***.

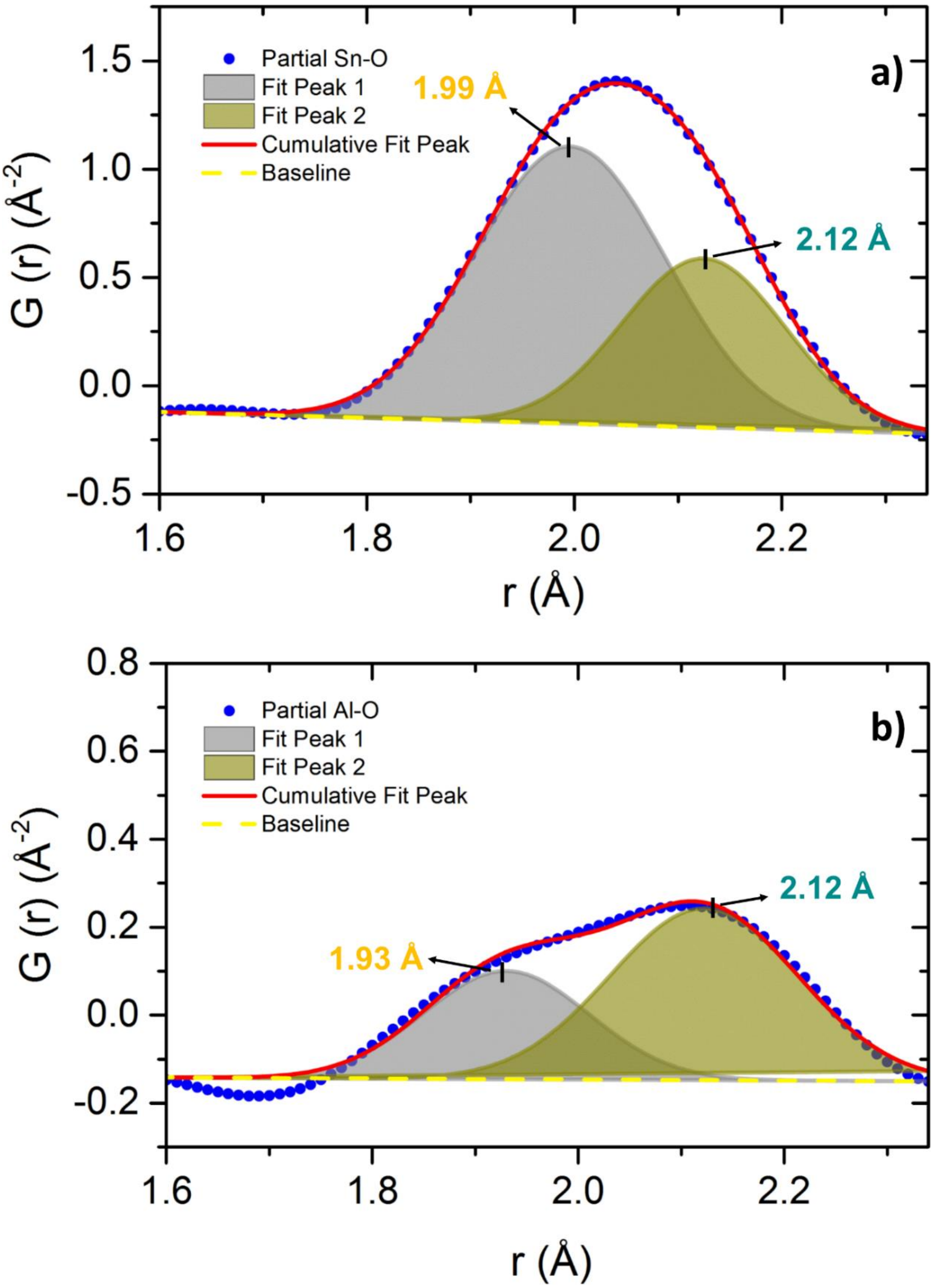

Figure 74 *- Gaussian fits of the first peaks of weight-independent partial PDFs belong to a) Sn-O and b) Al-O.*

***Table 18** - Peak characteristics of fitted first peaks of weight-independent partial PDFs of Al-O and Sn-O.*

	Al-O		**Sn-O**	
	Peak 1	Peak 2	Peak 1	Peak 2
Peak Center (Å)	1.93	2.12	1.99	2.12
Peak Area	0.05	0.09	0.15	0.29
Area Ratio (%)	35.7	64.3	65.8	34.2
FWHM (Å)	0.19	0.22	0.22	0.18

4.1.3. DISCUSSION

Conventional Rietveld refinements usually fail for nanostructured complex materials because of the small size of nanoparticles and the increased contribution from surface atoms compared to the bulk. Therefore, the average structure investigation of disordered nanoparticles gives slightly different results compared to the PDF analysis. The PDF method that makes use of the Fourier transform of the total scattering signal depicts a complementary approach to structure determination of nanosized complex materials. It allows for the investigation of the short-range ordering and the cation/anion/vacancy arrangements on the different crystallographic sites in the nanoparticles. In particular, the crystallite size of $Al_{0.57}Sn_{0.43}O_{1.71}$ nanoparticles determined from the peak attenuation in the PDF refinement is about 20 Å for both samples. The average crystallite sizes from Rietveld refinement for the samples are 14 (±3) Å and 11 (±2) Å. This demonstrates again that the use of the Scherrer-type 1/cosθ dependent reflection broadening estimate of the crystallite size is less accurate in the case of both, very small nanocrystals and disorder. The crystallite sizes of $Al_{0.57}Sn_{0.43}O_{1.71}$ nanoparticles from the PDF refinement are about 20 Å which is in good agreement with earlier HRTEM investigations (~20 Å) on the same sample [67]. The cell parameters obtained from the PDF refinement of $Al_{0.57}Sn_{0.43}O_{1.71}$ nanoparticles calcined at 550ºC and 40ºC are smaller than that of the aristotype structure of SnO_2 due to the presence of oxygen vacancies and Al^{3+} ions instead of Sn^{4+} ions ***Table 19***.

Table 19 *- Comparison of PDF refinement results of* $Al_{0.57}Sn_{0.43}O_{1.71}$ *nanoparticles.*

	$Al_{0.57}Sn_{0.43}O_{1.71}$ calcined at 550ºC	$Al_{0.57}Sn_{0.43}O_{1.71}$ calcined at 40ºC
Atom Distances (Å)		
Sn-O/Al-O	1.96177(1)	1.96092(2)
Sn-O/Al-O	2.08921(1)	2.07721(2)
O-O	2.86589(1)	2.85657(3)
Cell Parameters (Å)		
a=b	4.711630(4)	4.690420(5)
c	3.154860(5)	3.147600(6)

For the sample calcined at 550ºC, since Al has 73 oxygen-vacancy ‘bonds’ and Sn only 23, the weight-independent partial PDFs of the cation-anion pairs for both samples indicate that oxygen vacancies are located mostly around the Al ions. Moreover, in the case of the sample calcined at 40ºC, Al has 91 oxygen-vacancy bonds and Sn 12 (***Figure 75***). Additionally, the partial PDFs of the cation-cation pairs for both samples illustrate a clustering of Al atoms.

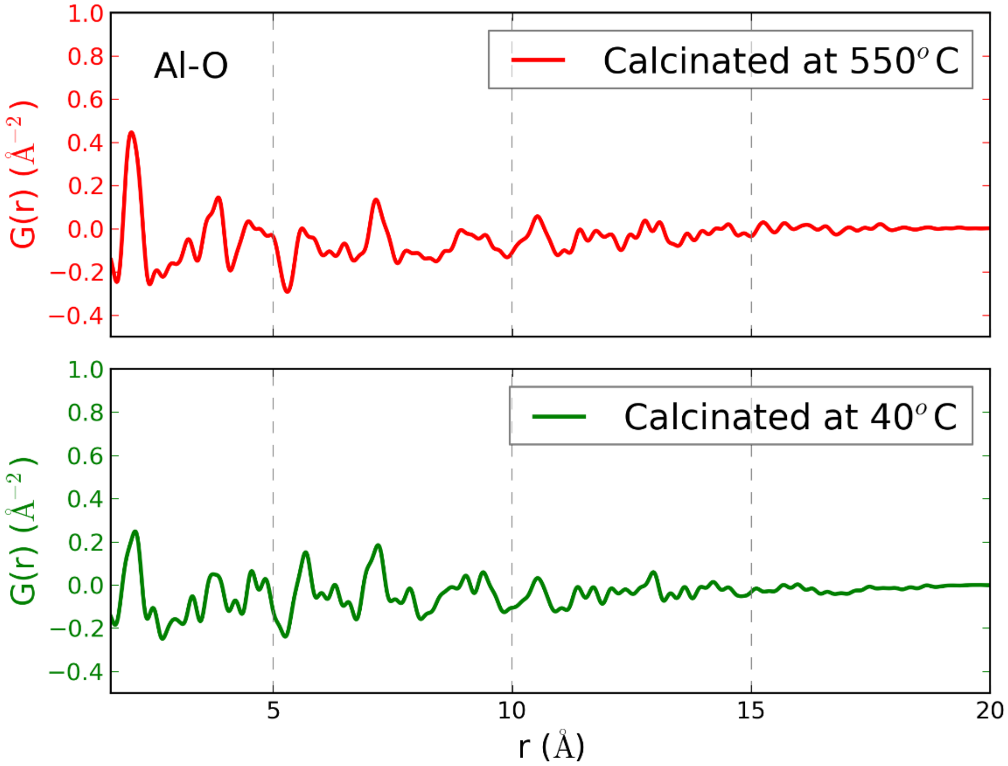

Figure 75 *- Comparison of weight-independent partial PDFs of Al-O pairs of nanoparticles calcined at 550°C and 40°C.*

The PDF peak-shape of the Al-O and Sn-O partial PDFs gives the atomic probability distribution in $Al_{0.57}Sn_{0.43}O_{1.71}$ nanoparticles. The maximum distortion around the aluminium and tin ions is about 0.1 Å for both samples. In the case of the sample calcined at 550°C, while the oxygen octahedra around Sn are rather compressed along the ‘vertical’ axis, they are elongated for the Al-O octahedra (***Figure 76-a and -b***). However, in the case of the sample calcined at 40°C, the oxygen octahedra around Sn are elongated along the ‘vertical’ axis and the Al octahedra are compressed (***Figure 76-c and -d***).

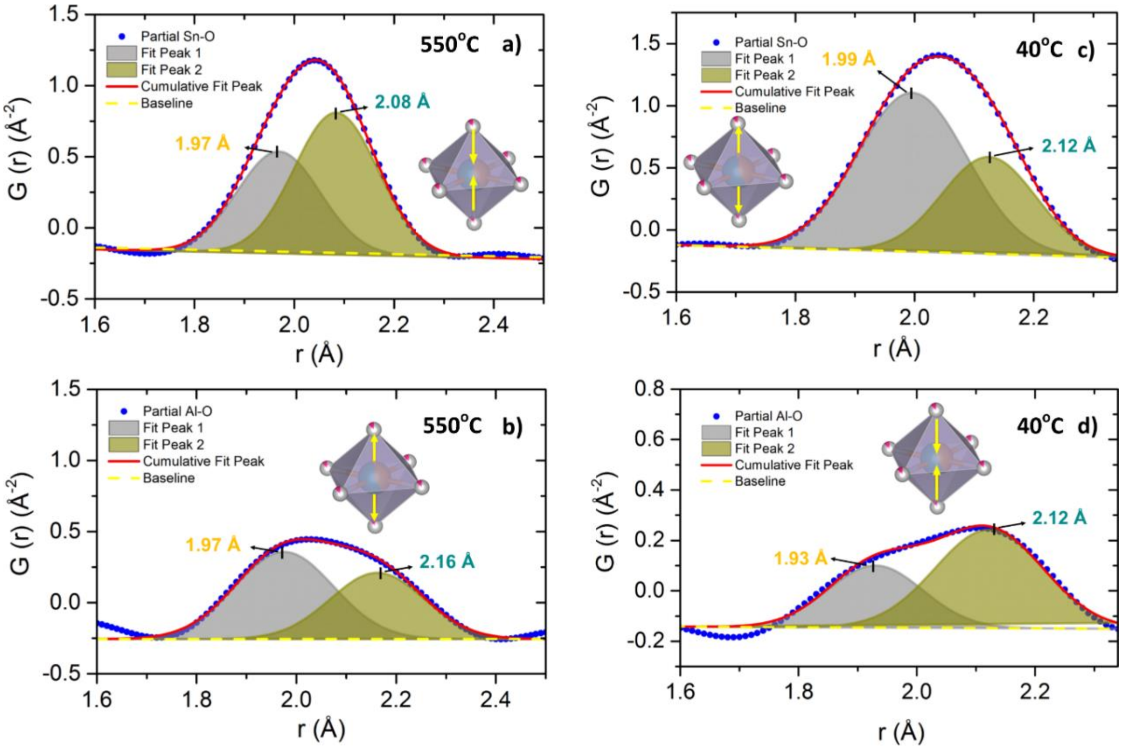

***Figure 76** - Comparison of fitted PDFs of the weight-independent partial PDFs of the metal-oxygen pairs of nanoparticles calcined at 550°C (a,b) and 40°C (c,d).*

The electrochemical properties of $Al_{0.57}Sn_{0.43}O_{1.71}$ nanoparticles were investigated by S. M. Becker [52]. The voltage profile during galvanostatic cycling of $Al_{0.57}Sn_{0.43}O_{1.71}$ shows that Sn is the electrochemically active element at about 0.9 V. The volume changes during Li-Sn alloying/dealloying can be attuned by a Li-Al-O matrix that is a stable buffer and so a better cycling stability is obtained. In comparison of the samples calcined at different temperatures, the best performance was achieved for the sample calcined at 550°C.

The elongated Al octahedra may help to construct a large enough matrix to compensate for the volume changes during electrochemical cycling. Therefore, the $Al_{0.57}Sn_{0.43}O_{1.71}$ nanoparticle calcined at 550 °C exhibits better electrochemical performance than at calcined 40 °C. As a conclusion, the small particle size and the presence of Al enhances the electrochemical stability and thereby strongly improves the electrochemical performance of $Al_{0.57}Sn_{0.43}O_{1.71}$ [52,67].

4.2. $LiMn_2O_4$

$LiMn_2O_4$ is a well-known positive electrode material for Li-ion batteries and adopts the cubic spinel structure with $Fd\bar{3}m$ space group (a=8.248 Å) [116]. Lithium ions occupy the tetrahedral *8a* sites while manganese atoms are situated on the *16d* site surrounded by oxygen on a *32e* site. $LiMn_2O_4$ has Jahn-Teller type local atomic distortion that are strongly dependent on the local distribution of Mn^{3+}/Mn^{4+} on the *16d* site [44,117]. Since X-ray diffraction provides spatially and time-averaged information on the structures, any information on disorder is seriously restricted by this averaging. However, exploring the total scattering data in real space, information about average structure, manifested in the Bragg reflections, and about local structure distortion, manifested in the diffuse scattering, can be extracted.

4.2.1. *Ex situ* X-ray Rietveld and PDF Analysis of $LiMn_2O_4$

Rietveld and PDF analysis based on *ex situ* synchrotron diffraction data are performed to examine the local structural distortion and to show the electronic structure of $LiMn_2O_4$.

4.2.1.1. Average Structure Analysis of $LiMn_2O_4$

The average structural refinements were carried out using the Rietveld method based on the synchrotron diffraction pattern, which was measured with SDD of 400 mm at P02.1. During refinement, background points referring to diffuse scattering, cell parameters, overall temperature parameters and the positions of oxygen atoms, were refined with a final an R-value of 4.69 %. The Rietveld refinement is shown in ***Figure 77***. $LiMn_2O_4$ powder crystallizes in the space group $Fd\bar{3}m$ No: 227 (origin choice 2) with a=8.2426(2) Å. The sample contained small amounts of Mn_3O_4 impurity (4 %). The results of the Rietveld refinement are listed in ***Table 20***.

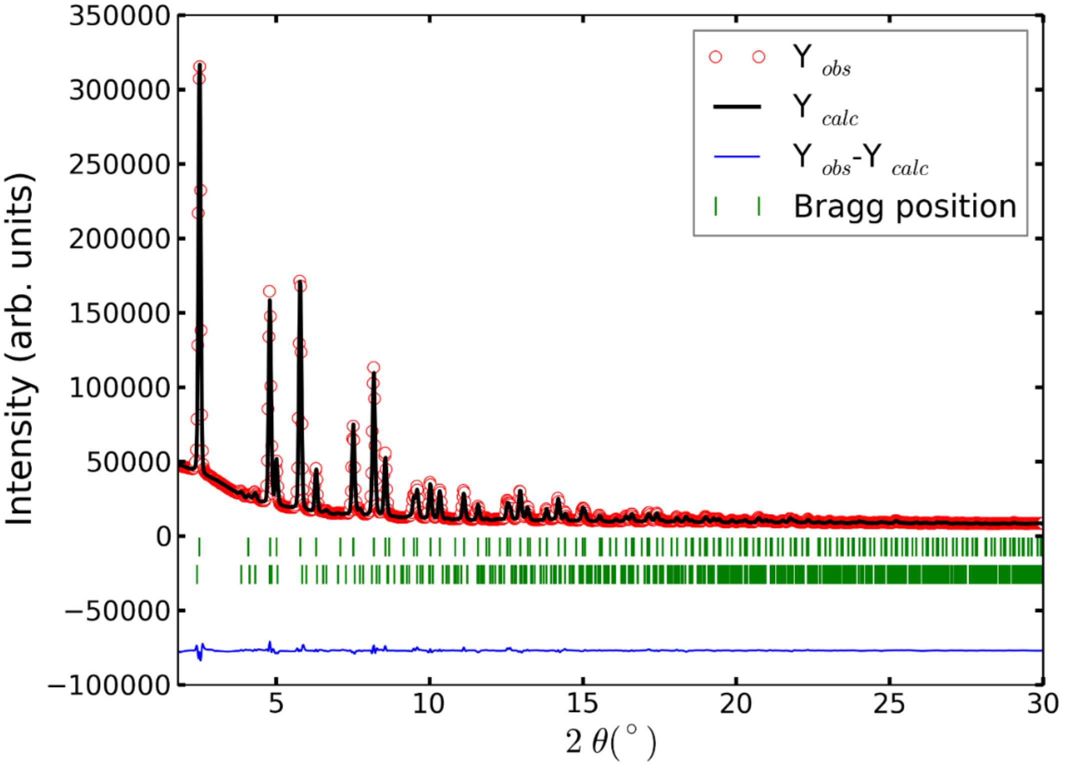

Figure 77 *- Synchrotron diffraction pattern of $LiMn_2O_4$ and Rietveld refinement with a cubic phase ($Fd\bar{3}m$ space group) and impurity Mn_3O_4 (lower line of indices) at 0.2079 Å.*

Table 20 *– Refinement results from the Rietveld analysis for $LiMn_2O_4$.*

Rietveld Analysis			
Average Atom Distances (Å)		**Cell Parameters (Å)**	
Li-O	1.9713(9)	**a=b=c**	8.2426(2)
Mn-O	1.9588(9)	**R_{wp}(%)**	4.39
Mn-Mn	2.91422(3)		
O-O	2.6093(13)		
O-O	2.9222(13)		

Bond valence sum (BVS) values were calculated using the VENUS (Visualization of Electron Nuclear and Structures) software package. The bond valence method is a technique to estimate the oxidation states of atoms [118–120]. The bond valence sum (BVS) between two ions in any compound can be calculated from the bond lengths and it is determined by the expression.

$$BVS = \sum_{i=1}^{n} exp\left(\frac{R_0 - R}{b}\right) \tag{45}$$

where R_0 is the tabulated bond lengths for the central atom of the selected coordination polyhedron [121], R is the actual bond length and b is a constant which is determined empirically by examining the bonding in a large number of structures and it is fixed at a typical value of 0.37 Å [118–120]. The crystal structure is shown in ***Figure 78***.

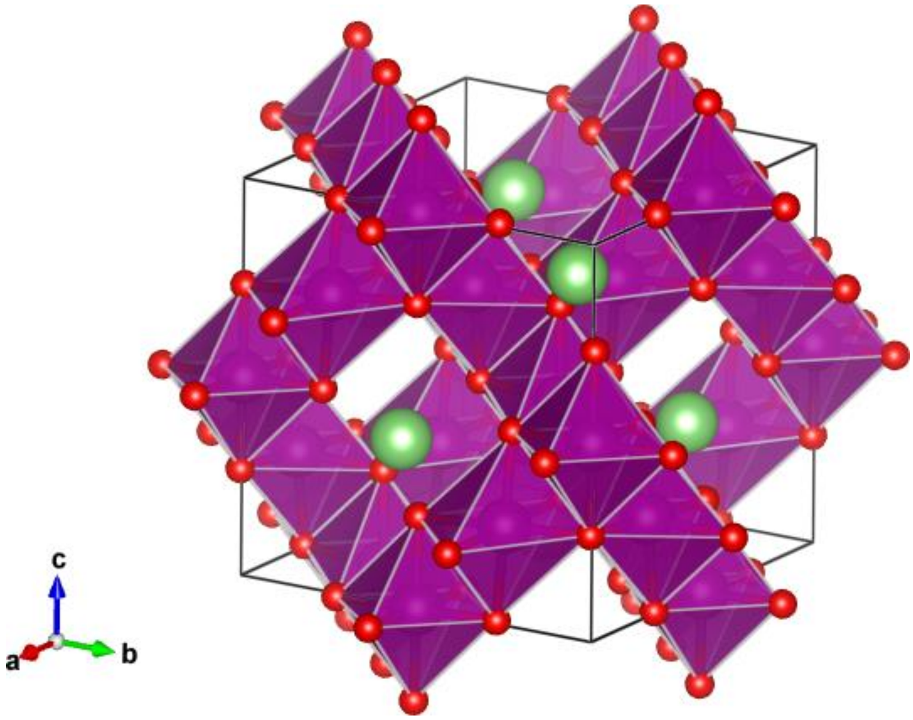

***Figure 78** – The crystal structure of $LiMn_2O_4$.*

The average oxidation state of Mn is +3.5 in a [MnO_6] octahedron which has six equivalent Mn-O distances. The bond valence parameter of the Mn^{4+} is 1.75 [120]. The calculated bond valence sum is +3.413 and the expected bond length is 1.949 Å. Results of the BVS calculation are listed in ***Table 21***.

__Table 21__ - Results of BVS calculation.

Input a bond valence parameter	1.75
Bond valence of O (x6)	-0.5688
Bond valence sum	3.413
Oxidation state of the cation	+3.5
Expected bond length (Å)	1.949

By using the PDF method, the atomic positions are determined more precisely than in conventional Rietveld refinement where the atomic positions are related to the intensities of the Bragg peaks. In order to calculate the BVS of Mn more precisely, the PDF method is necessary. Firstly, to estimate the diffuse scattering of $LiMn_2O_4$, background points with small steps were selected and the scattering data were subtracted by the empty capillary data. Then a full profile fitting with the structural model of $LiMn_2O_4$ was done (***Figure 79***). The diffuse scattering intensity is shown in blue in ***Figure 79*** as a result of the refinement of the background points.

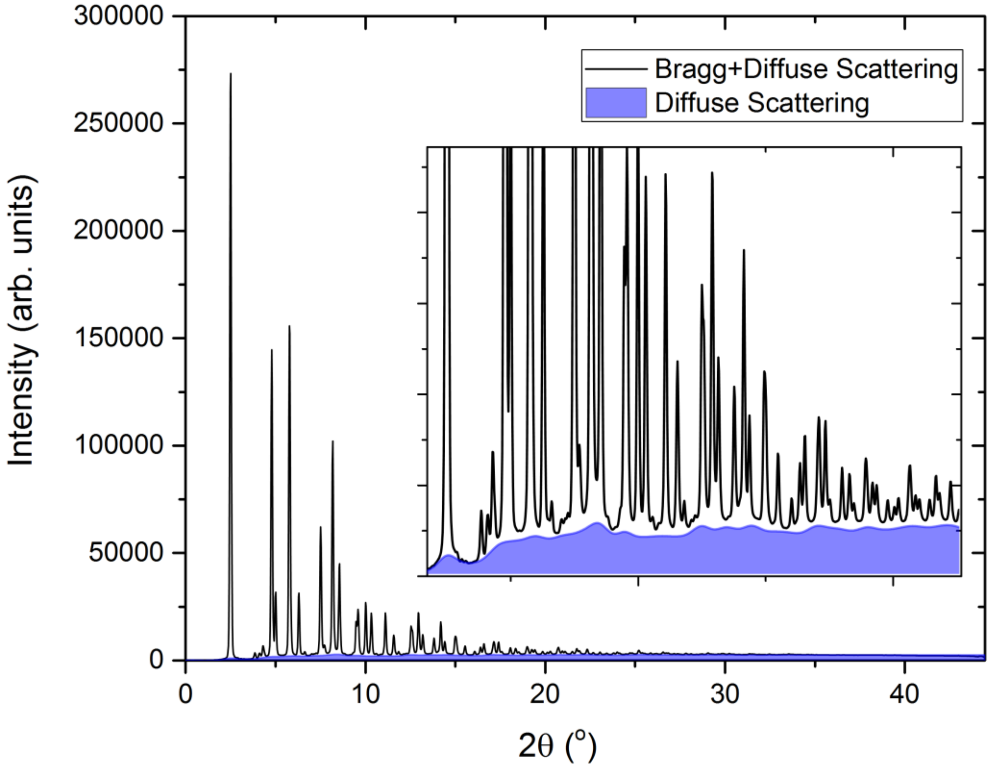

Figure 79 - *Estimation of diffuse scattering $LiMn_2O_4$.*

4.2.1.2. Small-Box Modelling

The structure of $LiMn_2O_4$ was investigated using small-box modelling. One unit cell with periodic conditions was analysed based on experimental PDF data using a least-squares procedure. The scale factors, cell parameters, thermal displacement parameters, the atomic correlation parameters and the positions of the oxygen ions and data scale parameters were refined to improve the fit (see ***Figure 80***). The refinement results in a large ADP parameter for the oxygen atoms. The mass fraction of the impurity phase Mn_3O_4 is 4 %. Results from the PDF analysis for the main phase are listed below (***Table 22***).

Table 22 *- Refinement results from the PDF analysis for* $LiMn_2O_4$ *main phase.*

PDF Analysis			
Average Atom Distances (Å)		**Cell Parameters (Å)**	
Li-O	1.946	**a=b=c**	8.247
Mn-O	1.973	**U_{iso} (Li)**	0.018
Mn-Mn	2.916	**U_{iso} (Mn)**	0.009
O-O	2.653	**U_{iso} (O)**	0.04
O-O	2.922	**R_{wp}(%)**	9.27

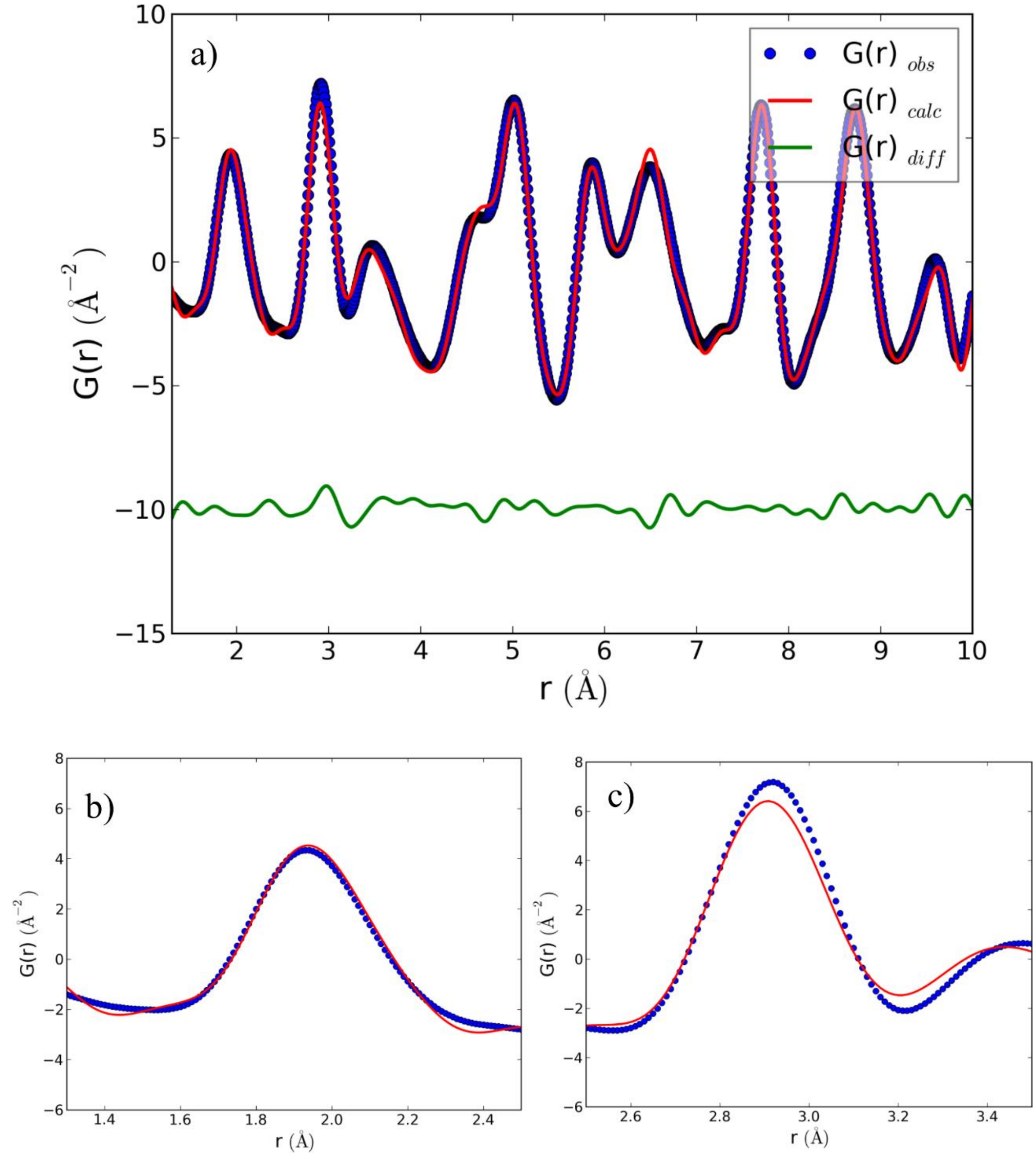

***Figure 80 -** a) PDF refinement of LiMn$_2$O$_4$, b) and c) zoomed views of the local structure region.*

The PDF fit is in good agreement except for the peaks at 1.93 Å, 2.92 Å, 3.48 Å, 6.50 Å, and 9.59 Å. The position of the peaks of the calculated and the experimental PDFs are mismatched at 1.93 Å, 3.48 Å and 9.59 Å, which are mostly related with Mn-O correlations. Additionally, the intensities are mismatched at 2.92 Å and 6.50 Å that contributes from O-O and Mn-Mn. After PDF refinement, the individual PDFs of each phase are compared in ***Figure 81***.

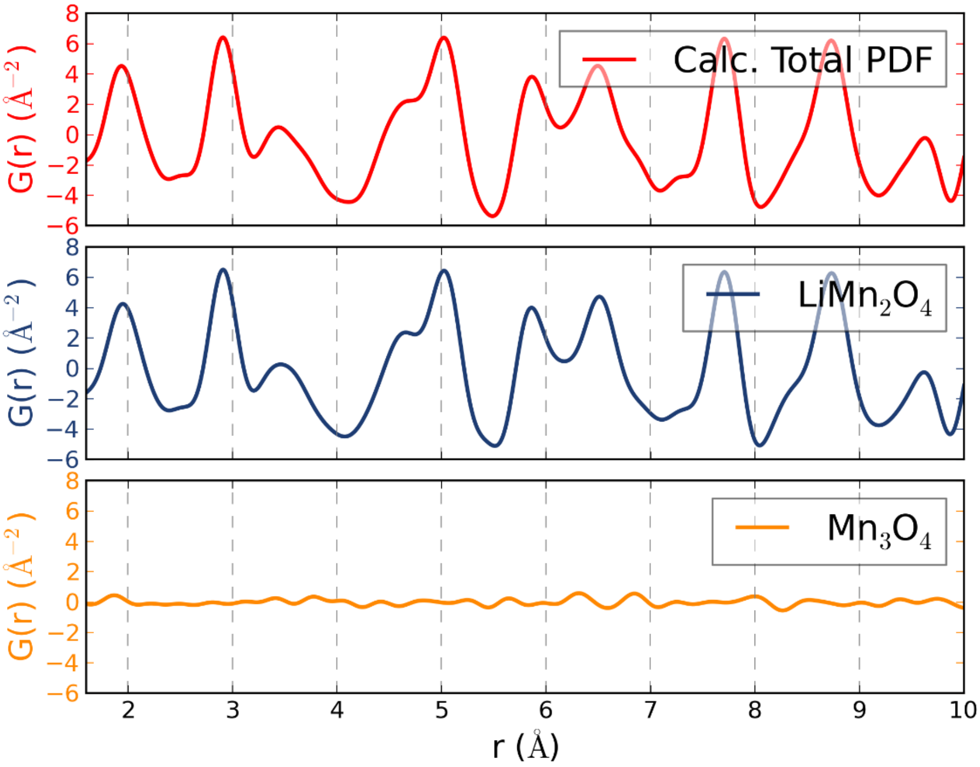

Figure 81 *– Individual PDFs of* $LiMn_2O_4$ *(96 %) and* Mn_3O_4 *(4 %).*

The first PDF peak around 1.93 Å is the nearest neighbour of Li-O and Mn-O. The second PDF peak indicates the Mn-Mn and O-O pairs. The partial PDFs of the atom pairs are shown in ***Figure 82***. The PDF peaks of the partial Mn-Mn pairs are narrower due to a lower temperature parameter of the Mn ions than that of other partial PDFs atom pairs. The broad PDF peak of the O-O pairs reveals a structural distortion with the oxygen ions involved.

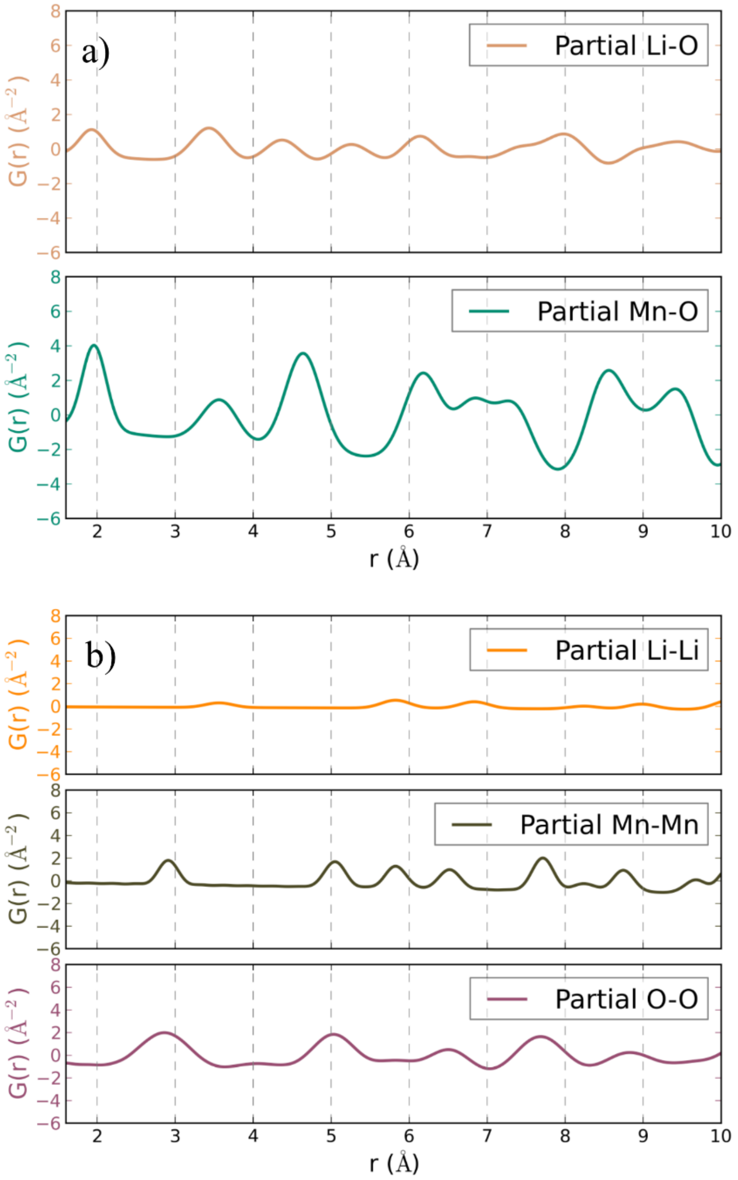

***Figure 82** – Weight-independent partial PDFs of a) metal-oxygen and b) metal-metal pairs.*

4.2.1.3. Big-Box Modelling

The structural distortion in $LiMn_2O_4$ was also investigated using the big-box modelling based on the same experimental PDF data. The DISCUS program package was used to model and refine the structural parameters of $LiMn_2O_4$ using a RMC algorithm. Its pair distribution function was computed by taking into account the termination ripples from the limited Q-range. Since it is not possible to refine multiple phases in the RMC algorithm, the calculated

PDF of the impurity phase was subtracted from the experimental PDF data. Firstly, the structural parameters based on the experimental PDF were refined using PDFGUI with two phases. The PDF of impurity phase was modelled with its scale factor and the structural parameters and then the modelled PDF was subtracted from the experimental PDF data. The results of the Rietveld refinement were used as starting parameters. A 3x3x1 supercell of $LiMn_2O_4$ (9 unit cells/504 atoms) was analysed (***Figure 83***). Mn atoms disproportionated into Mn^{3+} and Mn^{4+} are equally distributed on the octahedral site (*16d*) of $LiMn_2O_4$.

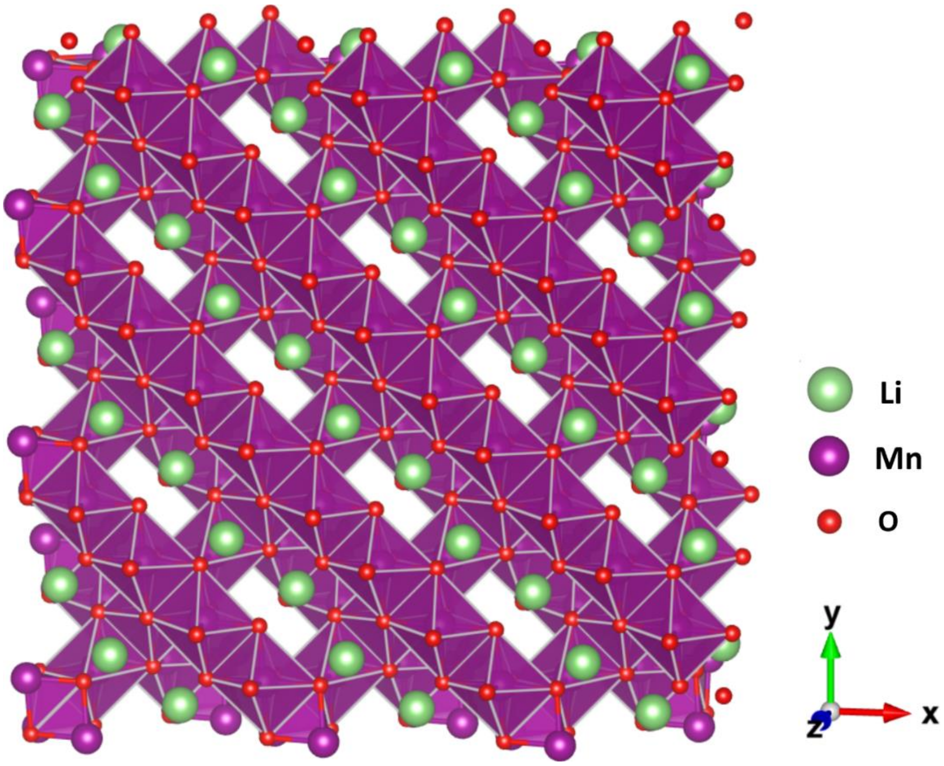

Figure 83 *– 3x3x1 supercell of* $LiMn_2O_4$ *viewed along of the z-direction.*

The structural parameters were refined in the range of 1.5-10 Å. To avoid unphysical atom movements, the minimum ion-ion distances were constrained for Mn-O, Li-O and O-O to 1.5 Å. The oxygen ions were selected and their positions shifted in 0.02 Å steps for each direction. The RMC refinement and the structure are shown in ***Figure 84***.

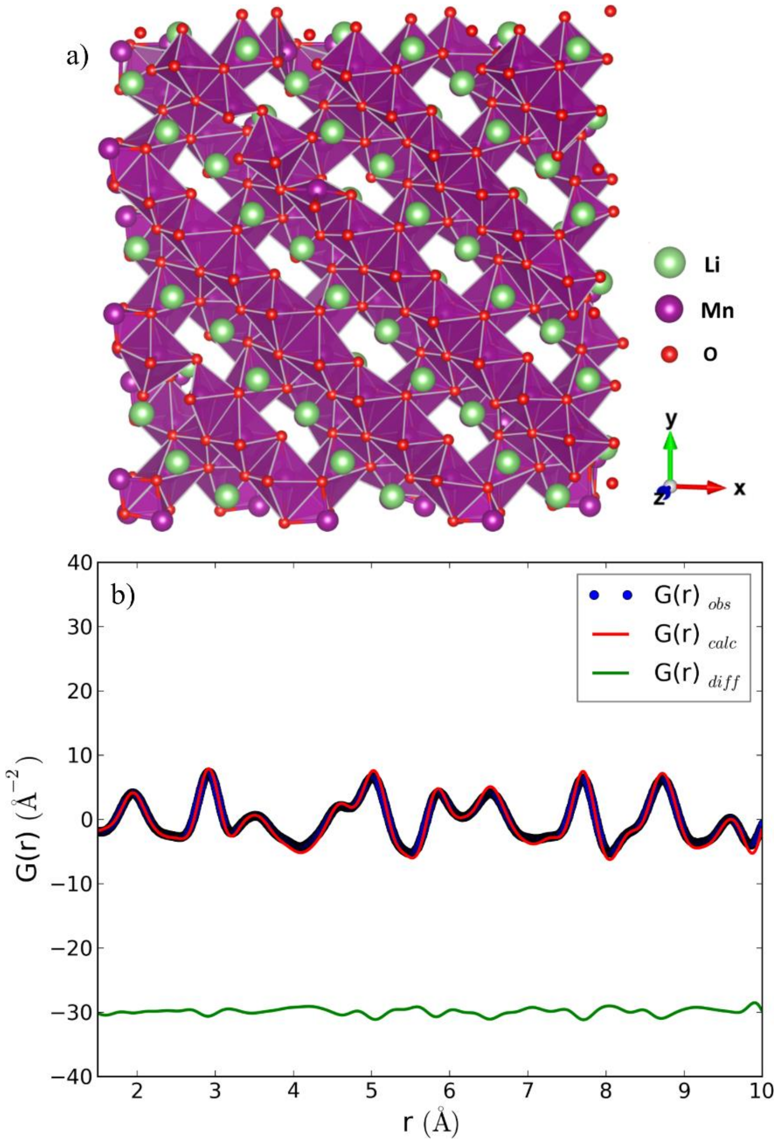

Figure 84 *– a) A two dimensional cut through the 3D model and b) comparison of calculated and experimental PDFs of $LiMn_2O_4$.*

After RMC refinement, the goodness-of-fit χ^2 decreased from 1.96 to 0.06 and hence all peaks are matched very well. Since the ionic radii of Mn^{3+} (high spin) and Mn^{4+} are 0.645 Å and 0.53 Å, respectively, the expected bond length of Mn^{3+}-O^{2-} is longer than that of Mn^{4+}. The mean bond length of Mn-O is about 1.97 Å as giving in the results of the small-box modelling. However, in the big-box modelling, the mixed-valence Mn^{3+}/Mn^{4+} can be distinguished. To understand the local environment of the mixed Mn valences, firstly, the weight-independent partial PDFs of the metal-oxygen pairs were obtained (***Figure 85***). Then its first peak was analysed.

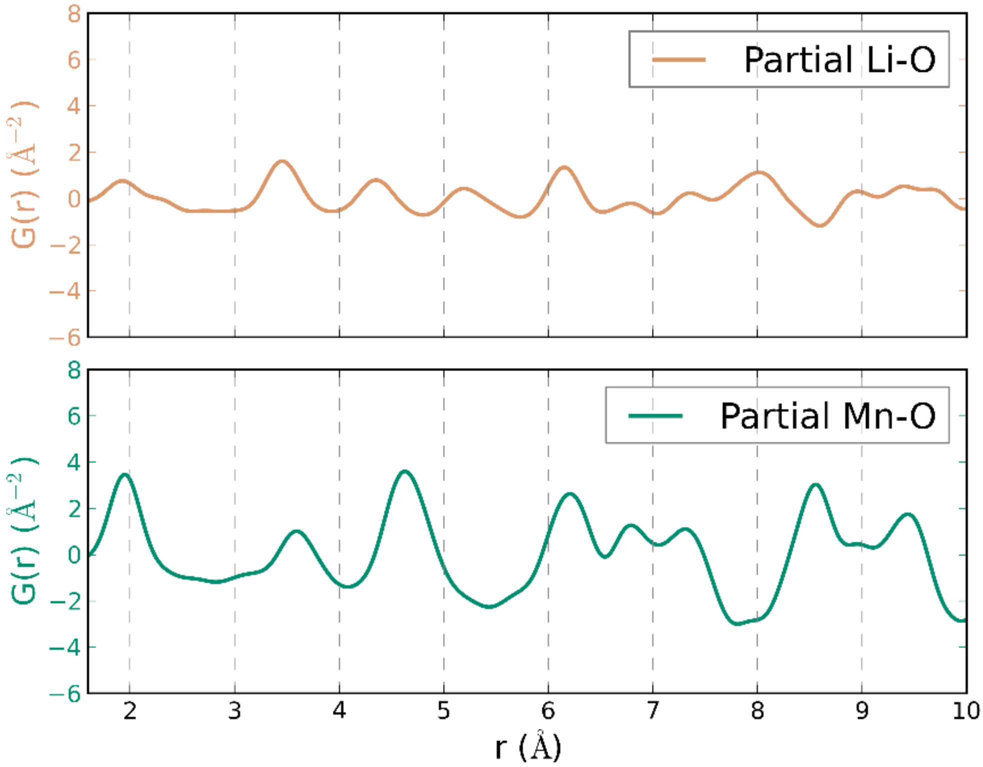

Figure 85 - *The weight-independent partial PDFs of $LiMn_2O_4$.*

The first peak of the weight-independent partial PDFs of Mn-O was fitted using a Gaussian function. It is shown in ***Figure 86*** where the negatively slopping yellow baseline is related to the average number density. The fit was done with two Gaussian peaks at 1.944 Å and 1.965 Å. The shorter bond length can be assigned to Mn^{4+} and the longer one to Mn^{3+}. The area of the PDF peak is related to the coordination number [8]. ***Figure 86*** and ***Table 23*** show that the number of the long bonds is higher than that of short bonds. In other words, the peak areas of Peak 1 and Peak 2 are 72 % and 28 %, respectively. According to this result, the structure has 0.56 mol of Mn^{3+} (28% of 2 moles of Mn). This observation is consistent with the results of electrochemistry (0.54 mol of Mn^{3+}) [13]. According to the area of the PDF peak, the average valence of the Mn ions is +3.72. Additionally, after the RMC refinement, the average bond valence sum from bond lengths of Mn-O using the BVS theory is +3.74. During BVS calculation, uncompleted octahedra on the surface of the structure were not taken into account.

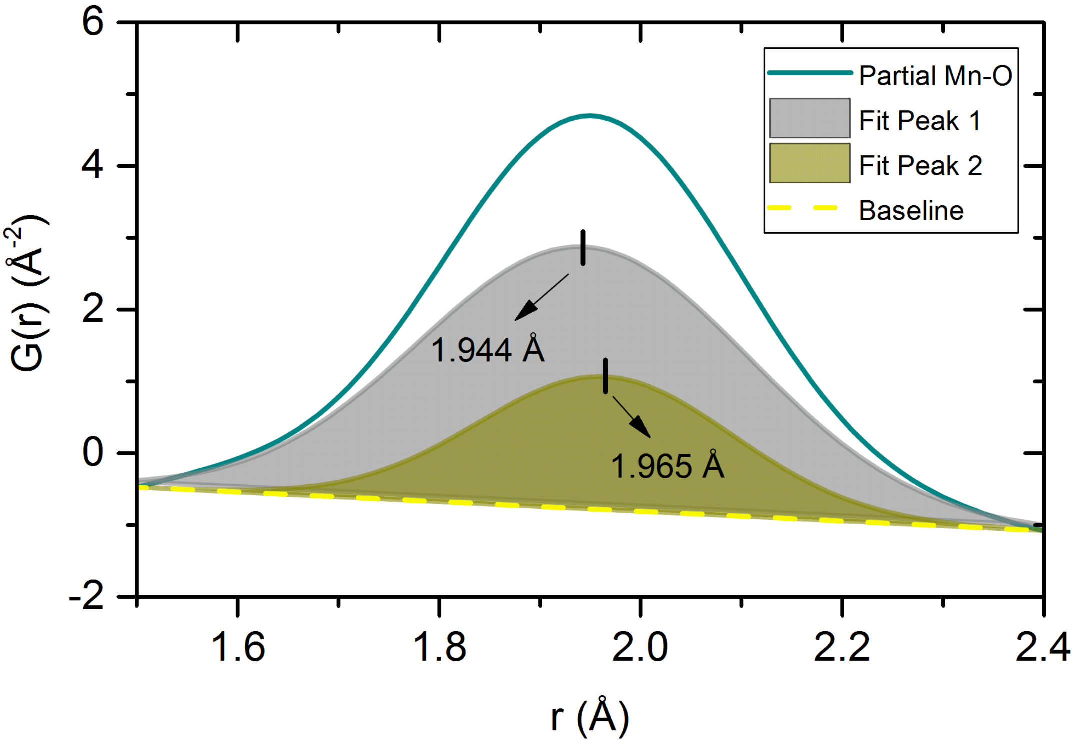

Figure 86 *- Gaussian fit of the first peak of weight-independent partial PDF of Mn-O.*

Table 23 *- Peak characteristics of the fitted peaks of the weight-independent partial PDF of Mn-O.*

	Mn-O	
	Peak 1	Peak 2
Peak Center (Å)	1.940	1.968
Peak Area	1.479	0.572
Area Ratio (%)	72	28

4.2.2. *In situ* X-ray PDF Analysis of $LiMn_2O_4$

In situ total scattering experiments were performed on lithium manganese oxide, $LiMn_2O_4$. It was carried out at a SDD of 400 mm and the maximum *Q*-value was about 24 $Å^{-1}$. ***Figure 87*** displays the first charging and subsequent discharging voltage profiles of the $LiMn_2O_4$ sample, as they correspond to the *in situ* synchrotron diffraction patterns. The $LiMn_2O_4$ cathode material was cycled with a charge/discharge rate of C/5 in the voltage range 1.5-4.9 V with the GCPL method (galvanostatic cycling with potential limitation) at room temperature. The electrochemical activity in the ~4V region, which is attributed to the Mn^{4+}/Mn^{3+}, directly correlates to the amount of Mn^{3+} in the material (0.54 moles). Using Faraday´s Law (Q=n.F/M) (Eq. **5**), the number of moles of Mn^{3+} can be estimated. The voltage profile shows a re-intercalation of ~0.75 mole of lithium into $LiMn_2O_4$ at ~3V during discharging. From ~3V, when the discharging process continues, an irreversible tetragonal phase starts to appear. The reason for this deep-discharge is to investigate the irreversible structural changes with the PDF technique in detail. The diffraction data recording was started with the charging of the cell and the exposure time per pattern was 1 min.

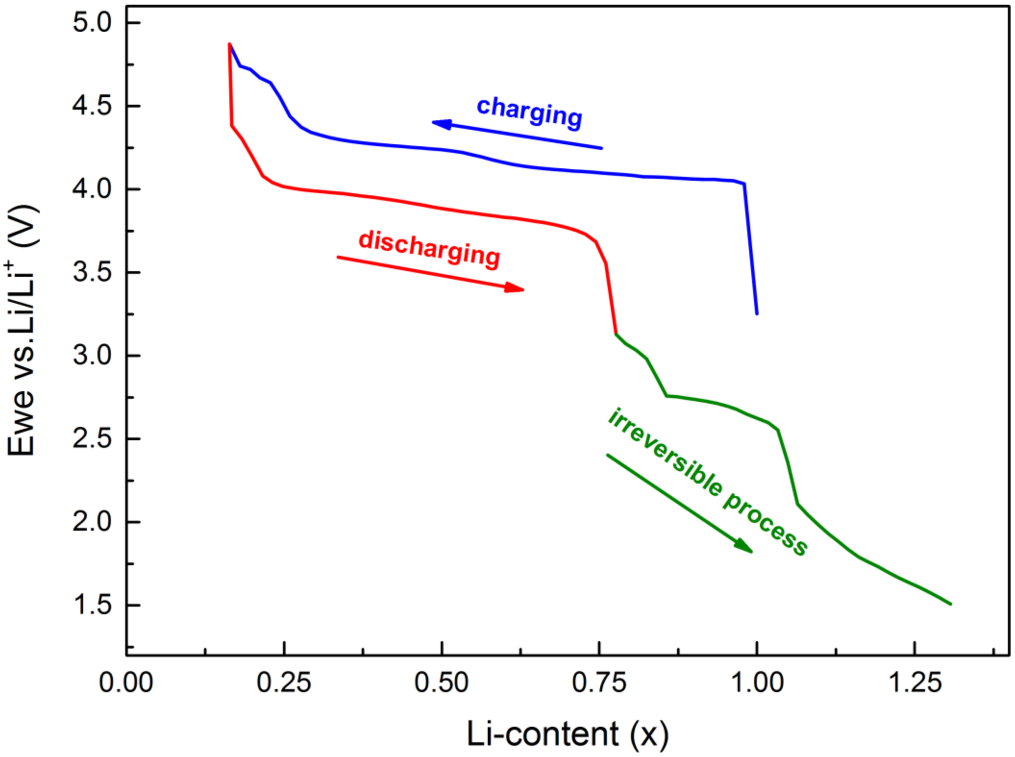

Figure 87 *- Voltage vs. Li content of* $Li_xMn_2O_4$.

All cell components without the active material were treated as background. The diffraction pattern of the first *in situ* data, the total background measurement and the background contributions of the individual components are shown in ***Figure 88***. This background comes from a separator, binder (wt. 10%), carbon (wt. 10%), electrolyte (200 ml) and two windows. Further data treatment was done with the background contribution subtracted from the diffraction signal. It is proven that the background is subtractable. The contribution of carbon and binder to total background is negligibly small.

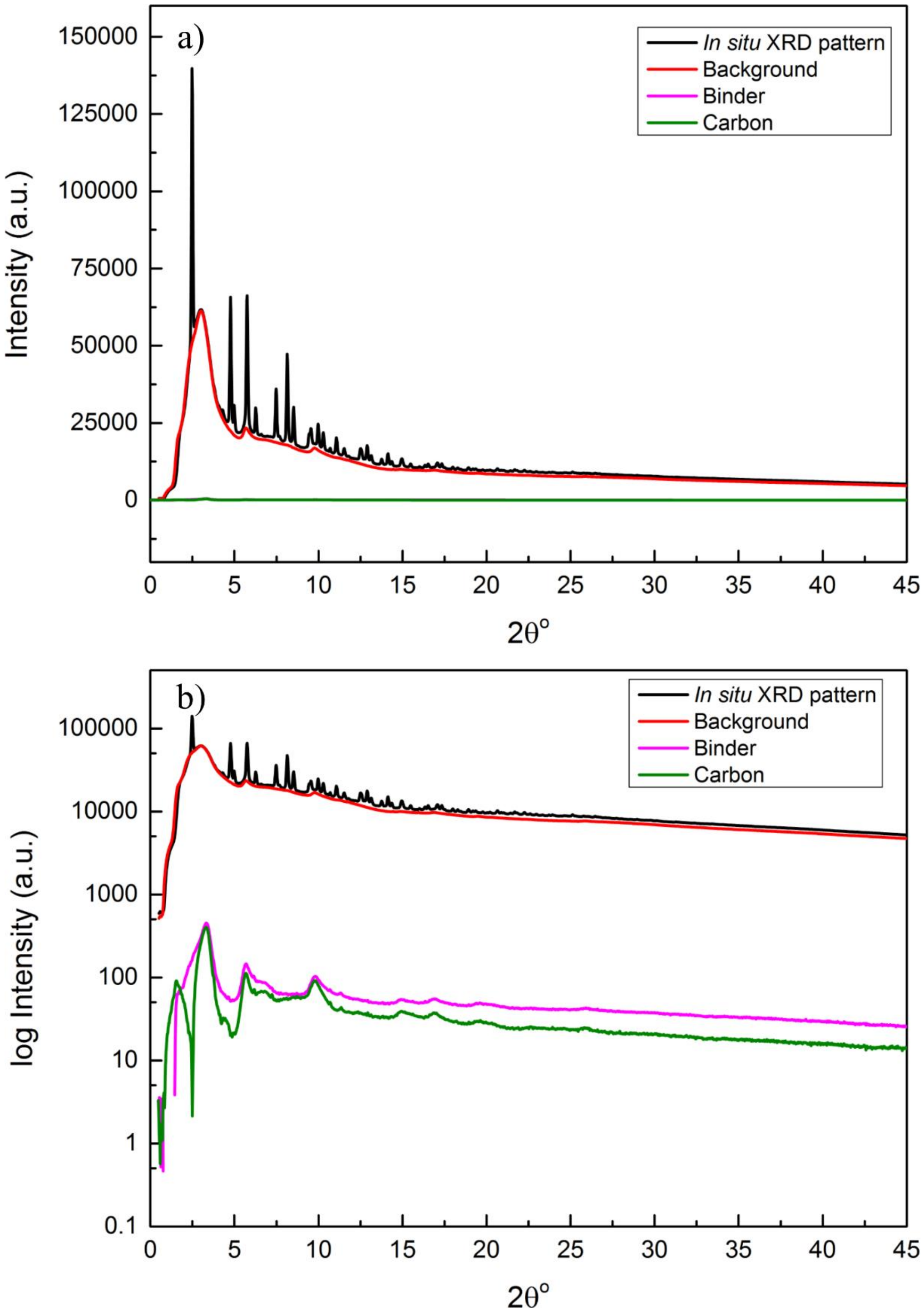

Figure 88 *– The XRD pattern of the first in situ data set and its background contributions a) in linear and b) in log scale.*

In ***Figure 87*** and ***Figure 89***, blue, red and green colours show charge, discharge and deep-discharge with C/2, respectively. Li ions shuttle repeatedly between both electrodes by hopping from one *8a* site to another one through the vacant octahedral *16c* site. Crystal field theory illustrates that Mn^{4+} ions have empty orbitals, on the other hand, Mn^{3+} ions have the available number of electrons for hopping in the e_g-band. Preserving the overall charge neutrality, the valences of the Mn reshuffle with Li diffusion during cycling. Therefore, Mn^{3+} and Mn^{4+} ions cannot be distinguished from *in situ* XRD and X-ray total scattering measurements. Only the average Mn valence can be seen.

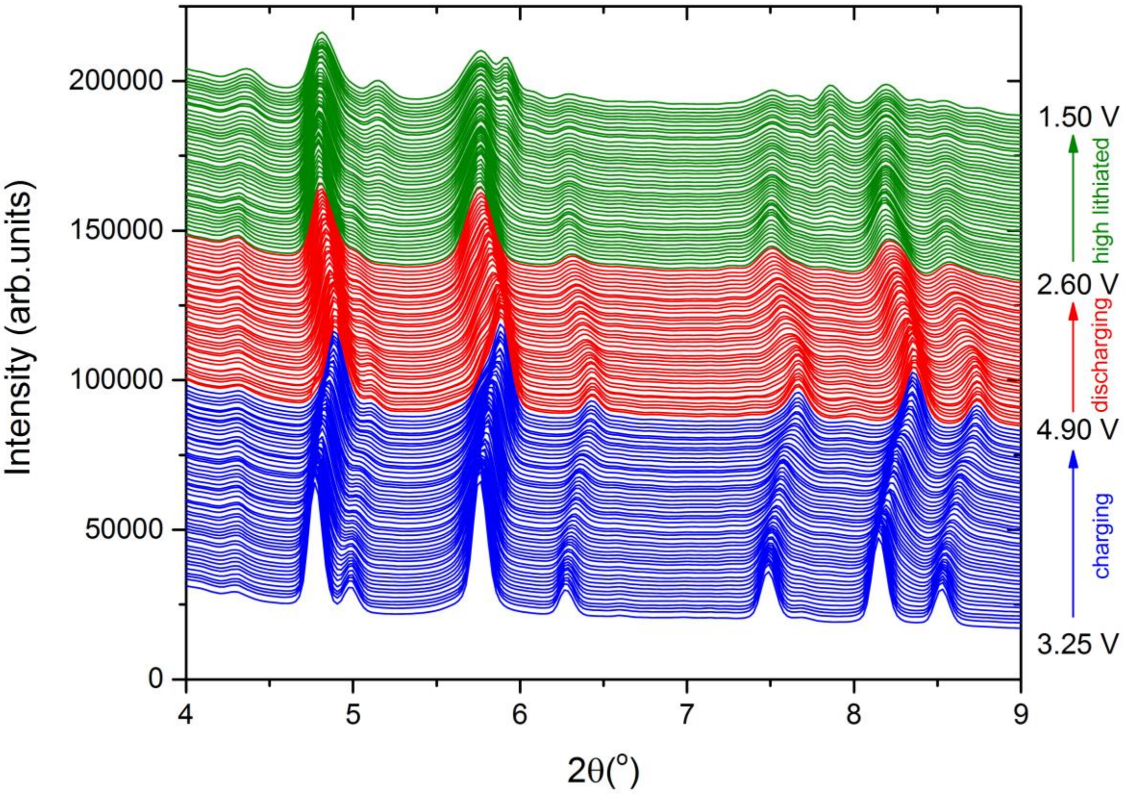

Figure 89 *– In situ diffraction patterns of $LiMn_2O_4$ during electrochemical cycling.*

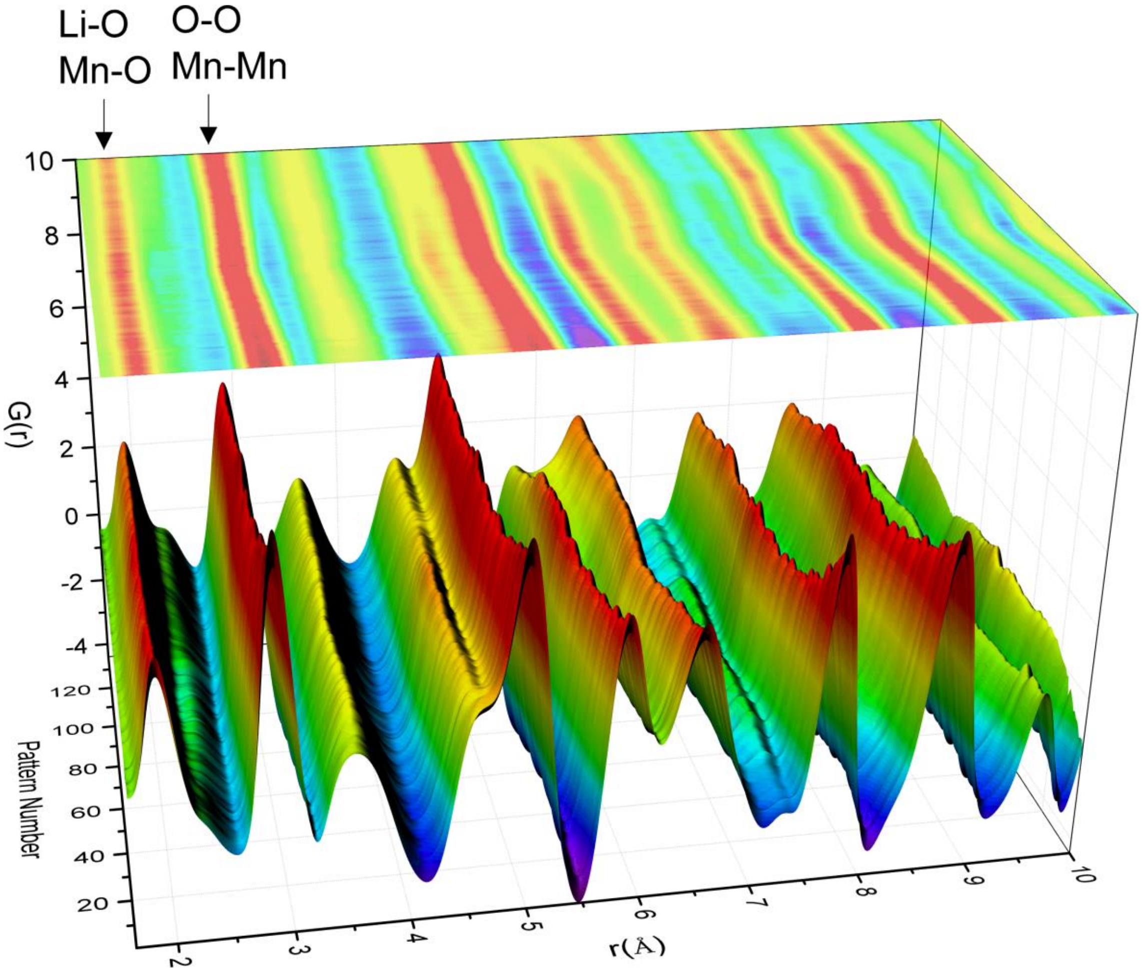

Figure 90 - *3D plot of the in situ PDFs of $LiMn_2O_4$ during electrochemical cycling.*

The diffraction patterns show that the Bragg peaks get higher 2θ values during charging because of Li deintercalation. So, the cell parameters (***Figure 91***) and bond lengths (***Figure 92***) get smaller. The opposite process occurs during discharging. The $Li_2Mn_2O_4$ type structure appears at 0.78 moles of Li (2.60 V) and it can be clearly seen as a new peak at 5.9° in the diffraction pattern (***Figure 89***). The tetragonally distorted $Li_{1+x}Mn_2O_4$ phase occurs when more than half of the Mn-ions are the Jahn-Teller distorted Mn^{3+} ions.

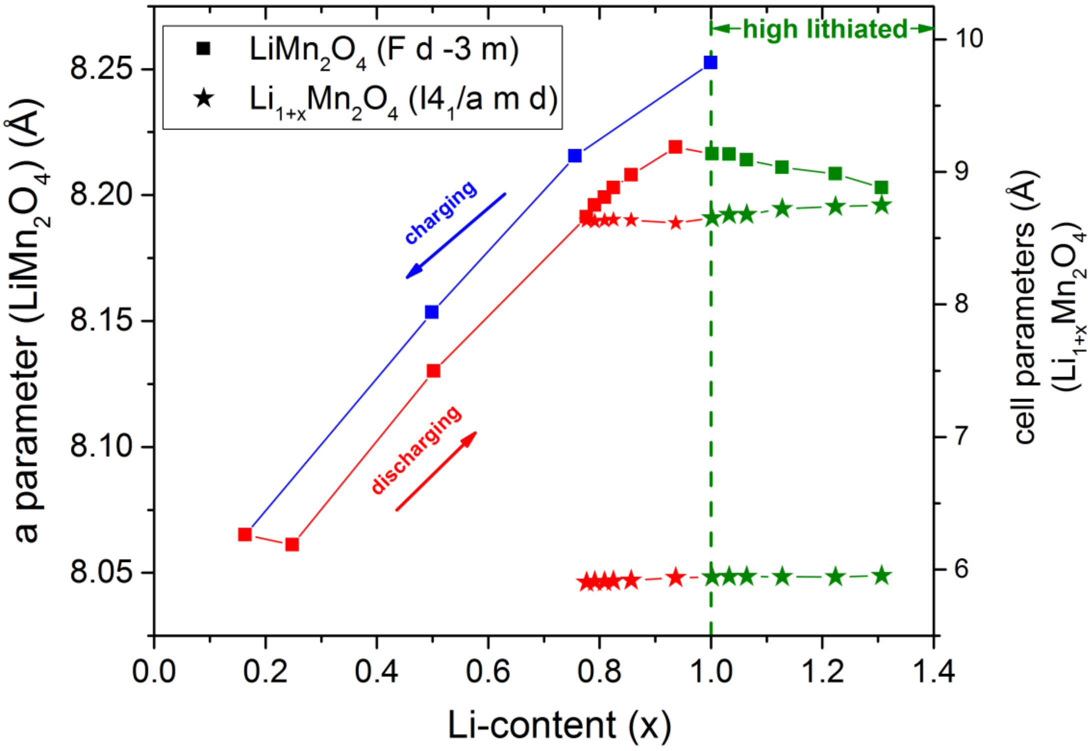

Figure 91 *- Cell parameters of phases from PDF refinement.*

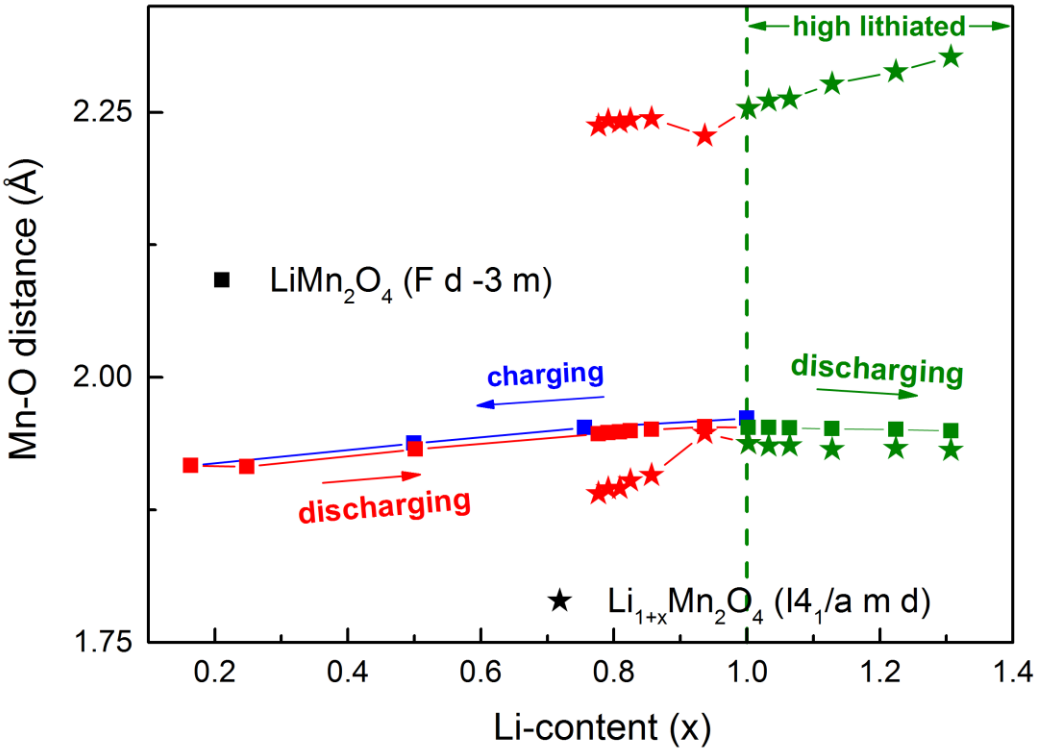

Figure 92 *- Mn-O distances during electrochemical cycling.*

According to the PDF analysis, the phase fraction of the main phase is more or less constant during charging. However, it decreases during discharging. The $Li_{1+x}Mn_2O_4$ phase with 7 % shows up at 3.5 V and its phase fraction increases with further discharge ***Figure 93***.

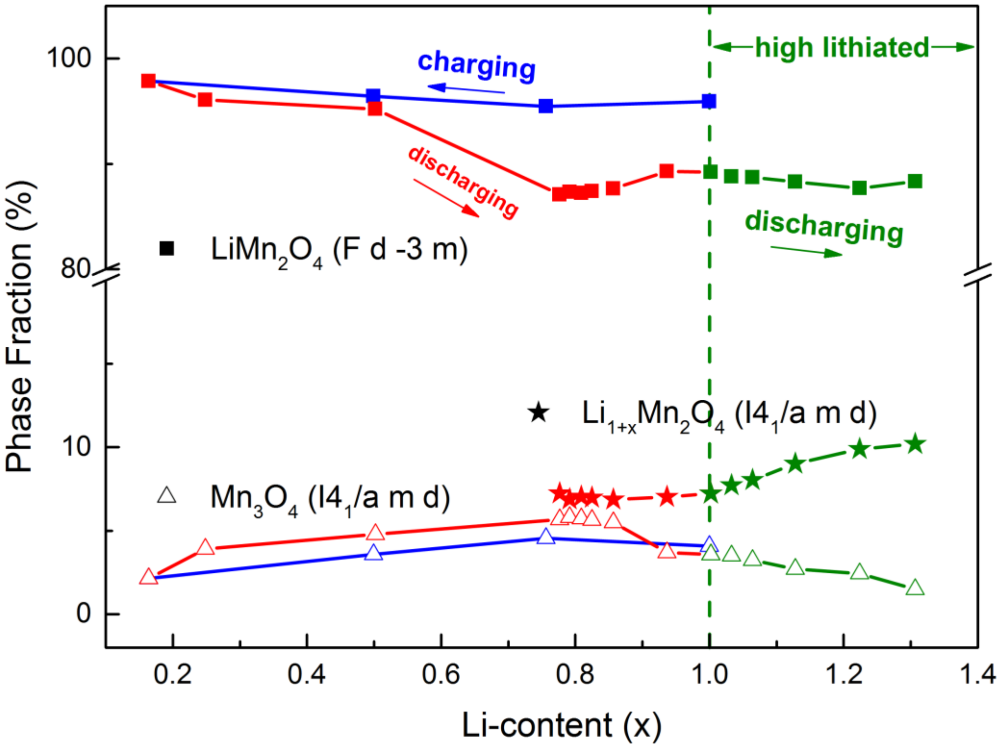

Figure 93 *- Phase fractions of in situ $LiMn_2O_4$ during electrochemical cycling.*

4.2.3. DISCUSSION

Before the application of *in situ* total scattering experiments on $LiMn_2O_4$, the electronic structure of $LiMn_2O_4$, a well-known positive electrode material for Li-ion batteries, was investigated using the Rietveld method and PDF methods based on *ex situ* data. After subtraction of the empty capillary measurement, a flat background contribution shows that, the material is crystalline. However, in the case of non-linear background, disorder exists in the crystalline material. The average structure was examined based on PDF data in a small box and based on diffraction data and the results are in good agreement with each other. In contrast to the average structure analysis based on PDF data, peaks are not matched very well in short range due to local distortion around Mn ions. The structural distortion in $LiMn_2O_4$ was investigated using a RMC algorithm. RMC refinement shows that the average valence of the Mn ions is +3.72 and Mn^{3+}/Mn^{4+} can be distinguished.

In situ total scattering experiments were successfully performed on $LiMn_2O_4$. All components without the active material were measured as background. The experiment demonstrates that the background is subtractable.

Chapter 5 - CONCLUSION and SUMMARY

The aim of this work was to check the applicability of the PDF method on battery electrode materials. Therefore, the instrument parameters of a Mo-$K_{\alpha1}$ diffractometer, the P02.1 beamline at Petra III and the MSPD beamline at ALBA for both real and reciprocal space were determined. The second aim was to investigate the average and local structure of nanocrystalline $Al_{0.57}Sn_{0.43}O_{1.71}$ anode material using conventional Rietveld refinement and X-ray Pair Distribution Function (PDF) technique. Furthermore, the electronic structure of $LiMn_2O_4$ was obtained using Rietveld and PDF methods based on *ex situ* data and the successful application of *in situ* total scattering experiments on $LiMn_2O_4$ was shown.

The finite Q-resolution of the measurement leads to a fading of the signal amplitude with r in the PDF data. If the amplitude of the PDF attenuates faster than dictated by the Q-resolution, the structural coherence of the sample can be determined by experimental PDF. Therefore, the determination of the dampening factor (Q_{damp}) that is characteristic for each experimental setup is important to measure the structural coherence. The structural peaks of LaB_6 in the PDF are evident up to 130 Å, 500 Å and 1150 Å for the P02.1 beamline (SDD 200mm) at Petra III, a Mo-$K_{\alpha1}$ diffractometer and the MSPD beamline at ALBA, respectively. For instance, to estimate the average crystallite size of a sample having a crystallite size of 20 nm and to perform a PDF, a Mo-$K_{\alpha1}$ diffractometer can be used as well as the MSPD beamline. However, the two-dimensional amorphous silicon (a-Si) flat panel detector has to be moved 400 mm away from the sample at beamline P02.1 at Petra III to get a sufficiently high Q-range. In this case the Q_{max} value is 22.74 Å^{-1}.

In the case of nanostructured complex materials, the results obtained from the average structure investigation with the Rietveld method and the PDF results are slightly different due to the small size of the nanoparticles and the increased contribution from surface-near ions compared to the bulk. In particular, the crystallite size of $Al_{0.57}Sn_{0.43}O_{1.71}$ nanoparticles determined from the peak attenuation in the PDF refinement is about 20 Å which is in good agreement with earlier HRTEM investigations on the same sample as compared to the Rietveld refinement which gives much smaller values of 14 (±3) Å and 11 (±2) Å for $Al_{0.57}Sn_{0.43}O_{1.71}$ calcined at 550°C and 40°C, respectively. The cell parameters obtained from PDF refinement of $Al_{0.57}Sn_{0.43}O_{1.71}$ nanoparticles calcined at 550°C and 40°C are smaller than that of the aristotype structure of SnO_2 due to the presence of oxygen vacancies and Al^{3+} ions instead of Sn^{4+} ions. The weight-independent partial PDFs of cation-anion pairs for both samples indicate that oxygen vacancies are located mostly around the Al atoms and cation-cation pairs for both samples illustrate a clustering of Al atoms. The maximum distortion around the aluminium and tin ions is about 0.1 Å for both samples. The Sn-O octahedra are rather compressed along the 'vertical' axis and elongated for the Al-O octahedral for the material calcined at 550°C. In contrast to that, for the material calcined at 40°C, the oxygen octahedra around Sn are elongated along the 'vertical' axis and the Al octahedra are compressed. The best electrochemical cycling stability performance was obtained for the sample calcined at 550°C. The volume changes during Li-Sn alloying/dealloying can be attuned by a Li-Al-O matrix and the elongated Al octahedra may help to construct a large enough matrix to compensate for the volume changes during electrochemical cycling, which results in a better cycling stability.

The electronic structure of $LiMn_2O_4$ was investigated using Rietveld and PDF methods based on *ex situ* data. After subtraction of the empty capillary measurement from the total scattering data, the baseline or background of the diffraction pattern that contains both Bragg and diffuse scattering shows that it is non-linear due to existence of disorder around the Mn ions. The results of the average structure analysis obtained from the Rietveld refinement are in accord with that of PDF. However, PDF peaks with short distances of $LiMn_2O_4$ do not match very well due to local distortion around the Mn ions. To illustrate the electronic structure given by *ex situ* PDF data a RMC refinement was performed. According to the RMC refinement, the average valence of Mn ions is +3.72 and the structure has 0.56 mol of Mn^{3+} which is consistent with the results of electrochemistry (0.54 mol of Mn^{3+}).

In situ total scattering experiments were carried out on $LiMn_2O_4$ successfully. Background measurements were done using components without the active material. The experiment demonstrates that the background from this *in situ* setup can be subtracted and a reliable PDF analysis of the electrochemically active material could be performed.

Bibliography

[1] L. B. McCusker, R. B. Von Dreele, D. E. Cox, D. Louër, and P. Scardi, '*Rietveld refinement guidelines*', Journal of Applied Crystallography, 32, 36–50, 1999.

[2] A. Clearfield, J. Reibenspies, and N. Bhuvanesh, '*Principles and Applications of Powder Diffraction*', John Wiley & Sons Ltd, 2008.

[3] P. Debye and P. Scherrer, '*Interferenz an regellos orientierten Teilchen im Röntgenlicht I*', Physikalische Zeitschrift, 17, 277, 1916.

[4] A. W. Hull, '*A New Method of X-ray Crystal Analysis*', Phys. Rev., 10, 661, 1917.

[5] J. I. Langford and D. Lou, '*Powder diffraction*', Rep. Prog. Phys., 59, 131–234, 1996.

[6] W. Paszkowicz, P. Knipping, and M. Laue, '*Ninety Years of Powder Diffraction : from Birth to Maturity*', Synchrotron Radiation in Natural Science, 5, 115–126, 2006.

[7] H. M. Rietveld, '*Line profiles of neutron powder-diffraction peaks for structure refinement*', Acta Crystallographica, 22, 151–152, 1967.

[8] T. Egami and S. J. L. Billinge, '*Underneath The Bragg Peaks Structural Analysis of Complex Materials*', Pergamon, 2003.

[9] S. L. J. Billinge and M. F. Thorpe, '*Local Structure from Diffraction*', Fundamental Materials Research, 1998.

[10] E. J. Mittemeijer and U. Welzel, '*Modern Diffraction Methods*', Wiley-VCH Verlag&Co. KGaA, 2013.

[11] T. R. Welberry, '*Diffuse x-ray scattering and models of disorder*', Rep. Prog. Phys., 48, 1543–1593, 1985.

[12] J. Xiao, X. Chen, P. V Sushko, M. L. Sushko, L. Kovarik, J. Feng, Z. Deng, J. Zheng, G. L. Graff, Z. Nie, D. Choi, J. Liu, J.-G. Zhang, and M. S. Whittingham, '*High-*

performance $LiNi_{0.5}Mn_{1.5}O_4$ spinel controlled by Mn^{3+} concentration and site disorder.', Advanced materials (Deerfield Beach, Fla.), 24, 2109–16, 2012.

[13] N. Kiziltas-Yavuz, A. Bhaskar, D. Dixon, M. Yavuz, K. Nikolowski, L. Lu, R.-A. Eichel, and H. Ehrenberg, '*Improving the rate capability of high voltage Lithium-ion battery cathode material $LiNi_{0.5}Mn_{1.5}O_4$ by ruthenium doping*', Journal of Power Sources, 267, 533–541, 2014.

[14] A. Bhaskar, *Investigations on $LiM_{0.5}Mn_{1.5}O_4$ (M=Fe, Co, Ni) Spinels as High-Volt Cathode Materials for Rechargeable Lithium-Ion Batteries, Technische Universität Darmstadt*, Technische Universität Darmstadt, 2011.

[15] J. Lee, A. Urban, X. Li, D. Su, G. Hautier, and G. Ceder, '*Unlocking the potential of cation-disordered oxides for rechargeable lithium batteries.*', Science (New York, N.Y.), 343, 519–22, 2014.

[16] B. Xu, D. Qian, Z. Wang, and Y. S. Meng, '*Recent progress in cathode materials research for advanced lithium ion batteries*', Materials Science and Engineering R: Reports, 73, 51–65, 2012.

[17] W.-M. Zhang, J.-S. Hu, Y.-G. Guo, S.-F. Zheng, L.-S. Zhong, W.-G. Song, and L.-J. Wan, '*Tin-Nanoparticles Encapsulated in Elastic Hollow Carbon Spheres for High-Performance Anode Material in Lithium-Ion Batteries*', Advanced Materials, 20, 1160–1165, 2008.

[18] A. R. Kamali and D. J. Fray, '*Tin-Based Materials As Advanced Anode Materials for Lithium Ion Batteries: A Review*', Rev. Adv. Mater. Sci., 27, 14–24, 2011.

[19] Y. Idota, '*Tin-Based Amorphous Oxide: A High-Capacity Lithium-Ion-Storage Material*', Science, 276, 1395–1397, 1997.

[20] T. Zheng and J. Dahn, '*Carbon Materials for Advanced Technologies*', Pergamon, 1999.

[21] J. S. Chen and X. W. D. Lou, '*SnO_2-based nanomaterials: synthesis and application in lithium-ion batteries*', Small (Weinheim an der Bergstrasse, Germany), 9, 1877–93, 2013.

[22] X. W. Guo, X. P. Fang, Y. Sun, L. Y. Shen, Z. X. Wang, and L. Q. Chen, '*Lithium storage in carbon-coated SnO_2 by conversion reaction*', Journal of Power Sources, 226, 75–81, 2013.

[23] J. Chen, '*Recent Progress in Advanced Materials for Lithium Ion Batteries*', Materials, 6, 156–183, 2013.

[24] C. Zhang, X. Peng, Z. Guo, C. Cai, Z. Chen, D. Wexler, S. Li, and H. Liu, '*Carbon-coated SnO_2/graphene nanosheets as highly reversible anode materials for lithium ion batteries*', Carbon, 50, 1897–1903, 2012.

[25] M. Zhang, D. Lei, Z. Du, X. Yin, L. Chen, Q. Li, Y. Wang, and T. Wang, '*Fast synthesis of SnO_2/graphene composites by reducing graphene oxide with stannous ions*', Journal of Materials Chemistry, 21, 1673, 2011.

[26] X. Wang, X. Zhou, K. Yao, J. Zhang, and Z. Liu, '*A SnO_2/graphene composite as a high stability electrode for lithium ion batteries*', Carbon, 49, 133–139, 2011.

[27] C.-M. Park, J.-H. Kim, H. Kim, and H.-J. Sohn, '*Li-alloy based anode materials for Li secondary batteries.*', Chemical Society reviews, 39, 3115–3141, 2010.

[28] C. Kim, M. Noh, M. Choi, J. Cho, and B. Park, '*Critical Size of a Nano SnO Electrode for Li-Secondary Battery*', Society, 17, 3297–3301, 2005.

[29] N. Li, C. R. Martin, and B. Scrosati, '*Nanomaterial-based Li-ion battery electrodes*', Journal of Power Sources, 97-98, 240–243, 2001.

[30] J.-K. Park, '*Principles and Applications of Lithium Secondary Batteries*', Wiley-VCH Verlag&Co. KGaA, 2012.

[31] J. O. Besenhard, J. Yang, and M. Winter, '*Will advanced lithium-alloy anodes have a chance in lithium-ion batteries?*', Journal of Power Sources, 68, 87–90, 1997.

[32] H. M. Rietveld, '*A profile refinement method for nuclear and magnetic structures*', Journal of Applied Crystallography, 2, 65–71, 1969.

[33] S. J. L. Billinge, '*The atomic pair distribution function: past and present*', Zeitschrift für Kristallographie, 219, 117–121, 2004.

[34] C. Daniel and J. O. Besenhard, '*Handbook of Battery Materials*', Wiley-VCH Verlag&Co. KGaA, Weinheim, Germany, 2011.

[35] D. Linden and T. B. Reddy, '*Handbook of Batteries*', McGraw-Hill Inc., 2001.

[36] M. Winter and R. J. Brodd, ‘*What are batteries, fuel cells, and supercapacitors?*’, Chemical reviews, 104, 4245–69, 2004.

[37] K. A. Aifantis, S. A. Hackney, and R. V. Kumar, ‘*High Energy Density Lithium Batteries Materials, Engineering, Applications*’, Wiley-VCH Verlag&Co. KGaA, 2010.

[38] K. Xu, ‘*Nonaqueous liquid electrolytes for lithium-based rechargeable batteries.*’, Chemical reviews, 104, 4303–417, 2004.

[39] Y. Abu-Lebdeh and I. Davidson, ‘*Nanotechnology for Lithium-Ion Batteries*’, Springer US, Boston, MA, 2013.

[40] J. L. Schaefer, Y. Lu, S. S. Moganty, P. Agarwal, N. Jayaprakash, and L. a. Archer, ‘*Electrolytes for high-energy lithium batteries*’, Applied Nanoscience, 2, 91–109, 2012.

[41] G. Pistoia, ‘*Lithium-Ion Batteries Advances and Applications*’, Elsevier, 2014.

[42] M. Yoshio, R. J. Brodd, and A. Kozawa, ‘*Lithium-Ion Batteries: Science and Technologies*’, Springer Science+Business Media, LLC, 2009.

[43] J. Xu, S. Dou, H. Liu, and L. Dai, ‘*Cathode materials for next generation lithium ion batteries*’, Nano Energy, 2, 439–442, 2013.

[44] M. M. Thackeray, ‘*Manganese Oxides for Lithium Batteries*’, Prog. Solid St. Chem., 25, 1–71, 1997.

[45] D. P. Shoemaker and R. Seshadri, ‘*Total-scattering descriptions of local and cooperative distortions in the oxide spinel* $Mg_{1-x}Cu_xCr_2O_4$ *with dilute Jahn-Teller ions*’, Physical Review B, 82, 214107, 2010.

[46] N. Loeffler, D. Bresser, and S. Passerini, ‘*Secondary Lithium-Ion Battery Anodes: From First Commercial Batteries to Recent Research Activities*’, Johnson Matthey Technology Review, 59, 34–44, 2015.

[47] J. Vetter, P. Novák, M. R. Wagner, C. Veit, K. C. Möller, J. O. Besenhard, M. Winter, M. Wohlfahrt-Mehrens, C. Vogler, and a. Hammouche, ‘*Ageing mechanisms in lithium-ion batteries*’, Journal of Power Sources, 147, 269–281, 2005.

[48] A. Barré, B. Deguilhem, S. Grolleau, M. Gérard, F. Suard, and D. Riu, '*A review on lithium-ion battery ageing mechanisms and estimations for automotive applications*', Journal of Power Sources, 241, 680–689, 2013.

[49] M. Winter, J. O. Besenhard, M. E. Spahr, and P. Novák, '*Insertion Electrode Materials for Rechargeable Lithium Batteries*', Advanced Materials, 10, 725–763, 1998.

[50] D. Ma, Z. Cao, and A. Hu, '*Si-Based Anode Materials for Li-Ion Batteries: A Mini Review*', Nano-Micro Letters, 6, 347–358, 2014.

[51] M. S. Park, G. X. Wang, Y. M. Kang, D. Wexler, S. X. Dou, and H. K. Liu, '*Preparation and electrochemical properties of* SnO_2 *nanowires for application in lithium-ion batteries*', Angewandte Chemie - International Edition, 46, 750–753, 2007.

[52] S. M. Becker, I. Issac, R. Heinzmann, M. Scheuermann, A. Eichhöfer, D. Wang, V. S. K. Chakravadhanula, C. Kübel, A. S. Ulrich, H. Hahn, and S. Indris, '*Nanocrystalline solid solutions* $Al_ySn_{1-y}O_{2-y/2}$ *(y=0.57, 0.4) as electrode materials for lithium-ion batteries*', Journal of Power Sources, 229, 149–158, 2013.

[53] N. Sharma, K. M. Shaju, G. V. S. Rao, and B. V. R. Chowdari, '*Anodic behaviour and X-ray photoelectron spectroscopy of ternary tin oxides*', Journal of Power Sources, 139, 250–260, 2005.

[54] E. Rönnebro, J. Yin, A. Kitano, M. Wada, and T. Sakai, '*Comparative studies of mechanical and electrochemical lithiation of intermetallic nanocomposite alloys for anode materials in Li-ion batteries*', Solid State Ionics, 176, 2749–2757, 2005.

[55] R. Alcántara, G. F. Ortiz, P. Lavela, and J. L. Tirado, '*Electrochemical and* ^{119}Sn *Mössbauer studies of the reaction of* Co_2SnO_4 *with lithium*', Electrochemistry Communications, 8, 731–736, 2006.

[56] I. Issac, M. Scheuermann, S. M. Becker, E. G. Bardají, C. Adelhelm, D. Wang, C. Kübel, and S. Indris, '*Nanocrystalline* $Ti_{2/3}Sn_{1/3}O_2$ *as anode material for Li-ion batteries*', Journal of Power Sources, 196, 9689–9695, 2011.

[57] G. Wang, X. P. Gao, and P. W. Shen, '*Hydrothermal synthesis of* Co_2SnO_4 *nanocrystals as anode materials for Li-ion batteries*', Journal of Power Sources, 192, 719–723, 2009.

[58] X. W. Lou, Y. Wang, C. Yuan, J. Y. Lee, and L. a. Archer, '*Template-Free Synthesis of* SnO_2 *Hollow Nanostructures with High Lithium Storage Capacity*', Advanced Materials, 18, 2325–2329, 2006.

[59] J. Ning, T. Jiang, K. Men, Q. Dai, D. Li, Y. Wei, B. Liu, G. Chen, B. Zou, and G. Zou, '*Syntheses, Characterizations, and Applications in Lithium Ion Batteries of Hierarchical SnO Nanocrystals*', The Journal of Physical Chemistry C, 113, 14140–14144, 2009.

[60] C. Xu, J. Tamaki, N. Miura, and N. Yamazoe, '*Grain size effects on gas sensitivity of porous* SnO_2*-based elements*', Sensors and Actuators B: Chemical, 3, 147–155, 1991.

[61] I. Sayago, J. Guierrez, L. Ares, J. I. Robla, M. C. Horrillo, J. Getino, J. Rino, and J. A. Agapito, '*The effect of additives in tin oxide on the sensitivity and selectivity to Nox and CO*', Sensors and Actuators B, 26-27, 19–23, 1995.

[62] M. Lei, Q. R. Hu, S. L. Wang, and W. H. Tang, '*Structural and optical properties of Al-doped* SnO_2 *nanowires*', Materials Letters, 64, 19–21, 2010.

[63] R. Alca, F. J. Ferna, J. C. Jumas, and J. Olivier-fourcade, '*Preparation , Sintering , and Electrochemical Properties of Tin Dioxide and Al-Doped Tin Dioxides Obtained from Citrate Precursors*', Chem. Mater, 12, 3044–3051, 2000.

[64] L. Xi, D. Qian, X. Huang, and H. E. Wang, '*Fine nanoparticles of Al-*SnO_2 *prepared by a co-precipitation route in water/oil microemulsion*', Journal of Alloys and Compounds, 462, 42–46, 2008.

[65] Y. M. Al-Angari, M. W. Kadi, I. M. Ismail, and M. a. Gabal, '*Effect of alumina incorporation on restricting grain growth of nanocrystalline tin(IV) oxide*', Central European Journal of Chemistry, 8, 331–340, 2010.

[66] T. a. Miller, S. D. Bakrania, C. Perez, and M. S. Wooldridge, '*A New Method for Direct Preparation of Tin Dioxide Nanocomposite Materials*', Journal of Materials Research, 20, 2977–2987, 2005.

[67] I. Issac, R. Heinzmann, S. M. Becker, T. Bräuniger, Z. Zhao-Karger, C. Adelhelm, V. S. Kiran Chakravadhanula, C. Kübel, A. S. Ulrich, and S. Indris, '*Synthesis of nanocrystalline solid solutions* $Al_ySn_{1-y}O_{2-y/2}$ *(y = 0.57, 0.4) investigated by XRD,* $^{27}Al/^{119}Sn$ *MAS NMR, and Mössbauer spectroscopy*', RSC Advances, 2, 10700, 2012.

[68] J. Rodriguez-Carvajal, '*Recent advances in magnetic structure determination by neutron powder diffraction*', Physica B, 192, 55–69, 1993.

[69] T. Proffen and H. Kim, '*Advances in total scattering analysis*', Journal of Materials Chemistry, 19, 5078, 2009.

[70] C. a. Young and A. L. Goodwin, ‘*Applications of pair distribution function methods to contemporary problems in materials chemistry*’, Journal of Materials Chemistry, 21, 6464, 2011.

[71] T. E. Faber and J. M. Ziman, ‘*A theory of the electrical properties of liquid metals*’, Philosophical Magazine, 11, 153–173, 1965.

[72] R. I. Barabash, G. E. Ice, and P. E. A. Turchi, ‘*Diffuse Scattering and the Fundamental Properties of Materials*’, 2009.

[73] P. Debye, ‘*Zerstreuung von Röntgenstrahlen*’, Annalen der Physik, 46, 809–823, 1915.

[74] B. E. Waren, ‘*X-Ray Diffraction*’, Dover New York, 1990.

[75] S. J. L. Billinge and C. L. Farrow, ‘*Towards a robust ad-hoc data correction approach that yields reliable atomic pair distribution functions from powder diffraction data*’, 2012.

[76] R. E. Dinnebier and S. J. L. Billinge, in *Powder Diffraction*, eds. R. E. Dinnebier and S. J. L. Billinge, Royal Society of Chemistry, Cambridge, 2008.

[77] C. N. J. Wagner, ‘*Structure of Amorphous Alloy Films*’, Journal of Vacuum Science and Technology, 6, 650, 1969.

[78] V. Petkov, Y. Ren, S. Kabekkodu, and D. Murphy, ‘*Atomic pair distribution functions analysis of disordered low-Z materials*’, Physical Chemistry Chemical Physics, 15, 8544, 2013.

[79] S. J. L. Billinge and M. G. Kanatzidis, ‘*Beyond crystallography: the study of disorder, nanocrystallinity and crystallographically challenged materials with pair distribution functions*’, Chemical Communications, 749, 2004.

[80] B. H. Toby and T. Egami, ‘*Accuracy of pair distribution function analysis applied to crystalline and non-crystalline materials*’, Acta Crystallographica Section A Foundations of Crystallography, 48, 336–346, 1992.

[81] F. Fauth, I. Peral, C. Popescu, and M. Knapp, ‘*The new Material Science Powder Diffraction beamline at ALBA Synchrotron*’, Powder Diffraction, 28, S360–S370, 2013.

[82] R. G. Haverkamp and K. S. Wallwork, '*X-ray pair distribution function analysis of nanostructured materials using a Mythen detector*', Journal of synchrotron radiation, 16, 849–56, 2009.

[83] M. Herklotz, '*Advances in in situ powder diffraction of battery materials – a case study of the new beamline P02.1 at DESY Hamburg*', Journal of Applied Crystallography, 46, 1117 – 1127, 2013.

[84] P. J. Chupas, X. Qiu, J. C. Hanson, P. L. Lee, C. P. Grey, and S. J. L. Billinge, '*Rapid-acquisition pair distribution function (RA-PDF) analysis*', Journal of Applied Crystallography, 36, 1342–1347, 2003.

[85] M. Yavuz, N. Kiziltas-Yavuz, A. Bhaskar, M. Scheuermann, S. Indris, F. Fauth, M. Knapp, and H. Ehrenberg, '*Influence of Iron on the Structural Evolution of $LiNi_{0.4}Fe_{0.2}Mn_{1.4}O_4$ during Electrochemical Cycling Investigated by in situ Powder Diffraction and Spectroscopic Methods*', Zeitschrift für anorganische und allgemeine Chemie, 640, 3118–3126, 2014.

[86] V. Pecharsky and Zavalij, '*Fundamentals of Powder Diffraction and Structural Characterization of Materials*', Springer-Verlag, New York, 2005.

[87] F. Sanchez-Bajo and F. L. Cumbrera, '*The use of the pseudo-Voigt function in the variance method of X-ray line broadening analysis*', Journal of Applied Crystallography, 30, 427–430, 1997.

[88] G. Walker, '*Solid-State hydrogen Materials and Chemistry*', Woodhead Publishing Limited and CRC Press LLC, 2008.

[89] P. J. Chupas, K. W. Chapman, and P. L. Lee, '*Applications of an amorphous silicon-based area detector for high-resolution, high-sensitivity and fast time-resolved pair distribution function measurements*', Journal of Applied Crystallography, 40, 463–470, 2007.

[90] C. L. Farrow, P. Juhas, J. W. Liu, D. Bryndin, E. S. Božin, J. Bloch, T. Proffen, and S. J. L. Billinge, '*PDFfit2 and PDFgui: computer programs for studying nanostructure in crystals*', Journal of Physics: Condensed Matter, 19, 335219, 2007.

[91] A. P. Hammersley, S. O. Svensson, M. Hanfland, a. N. Fitch, and D. Hausermann, '*Two-dimensional detector software: From real detector to idealised image or two-theta scan*', High Pressure Research, 14, 235–248, 1996.

[92] X. Yang, P. Juhás, and S. J. L. Billinge, '*On the estimation of statistical uncertainties*

on powder diffraction and small-angle scattering data from two-dimensional X-ray detectors', Journal of Applied Crystallography, 2014.

[93] X. Qiu, J. W. Thompson, and S. J. L. Billinge, '*PDFgetX2 : a GUI-driven program to obtain the pair distribution function from X-ray powder diffraction data*', Journal of Applied Crystallography, 37, 678–678, 2004.

[94] P. Juhás, T. Davis, C. L. Farrow, and S. J. L. Billinge, '*PDFgetX3 : a rapid and highly automatable program for processing powder diffraction data into total scattering pair distribution functions*', Journal of Applied Crystallography, 46, 560–566, 2013.

[95] X. Q. and S. J. L. Billinge, '*PDFgetX2: a user-friendly program to obtain the pair distribution function from X-ray powder diffraction data*', 2–4, 2004.

[96] S. Ergun, '*Structure of Carbon*', Chemistry and Physiscs of Carbon, 3, 211–288, 1968.

[97] W. Ruland, '*The separation of coherent and incoherent Compton X-ray scattering*', British Journal of Applied Physics, 15, 1301–1307, 1964.

[98] C. W. Dwiggins and D. a. Park, '*Calculation of the intensity of secondary scattering of X-rays by non-crystalline materials*', Acta Crystallographica Section A, 27, 264–272, 1971.

[99] I. Jeong, J. Thompson, T. Proffen, and S. Billinge, '*PDFGetX User 's Manual*', 2003.

[100] C. Lamberti and G. Agostini, '*Characterization of Semiconductor Heterostructures and Nanostructures*', Elsevier, 2013.

[101] T. Proffen and R. B. Neder, '*DISCUS : a program for diffuse scattering and defect-structure simulation*', Journal of Applied Crystallography, 30, 171–175, 1997.

[102] R. L. McGreevy and L. Pusztai, '*Reverse Monte Carlo Simulation: A New Technique for the Determination of Disordered Structures*', Molecular Simulation, 1, 359–367, 1988.

[103] R. L. McGreevy and M. a Howe, '*RMC: Modeling Disordered Structures*', Annual Review of Materials Science, 22, 217–242, 1992.

[104] N. Metropolis, A. W. Rosenbluth, M. N. Rosenbluth, A. H. Teller, and E. Teller, '*Equation of State Calculations by Fast Computing Machines*', The Journal of

Chemical Physics, 21, 1087, 1953.

[105] R. B. Neder and T. Proffen, '*Diffuse Scattering and Defect Structure Simulations*', Oxford University Press, 2008.

[106] Z. L. Wang, Y. Lui, and Z. Zhang, '*Handbook of Nanophase and Nanostructured Materials*', 2002.

[107] S. Indris, M. Scheuermann, S. M. Becker, V. Šepelák, R. Kruk, J. Suffner, F. Gyger, C. Feldmann, A. S. Ulrich, and H. Hahn, '*Local Structural Disorder and Relaxation in SnO_2 Nanostructures Studied by ^{119}Sn MAS NMR and ^{119}Sn Mössbauer Spectroscopy*', The Journal of Physical Chemistry C, 115, 6433–6437, 2011.

[108] W. H. Baur and a. a. Khan, '*Rutile-type compounds. IV. SiO_2, GeO_2 and a comparison with other rutile-type structures*', Acta Crystallographica Section B Structural Crystallography and Crystal Chemistry, 27, 2133–2139, 1971.

[109] S. J. L. Billinge and I. Levin, '*The problem with determining atomic structure at the nanoscale.*', Science (New York, N.Y.), 316, 561–5, 2007.

[110] B. Y. R. D. Shannon, M. H, N. H. Baur, O. H. Gibbs, M. Eu, and V. Cu, '*Revised Effective Ionic Radii and Systematic Studies of Interatomie Distances in Halides and Chaleogenides*', Acta Cryst., A32, 751, 1976.

[111] A. M. M. Abeykoon, W. Donner, M. Brunelli, M. Castro-Colin, A. J. Jacobson, and S. C. Moss, '*From Average to Local Structure: A Rietveld and an Atomic Pair Distribution Function (PDF) Study of Selenium Clusters in Zeolite-NdY*', Journal of the American Chemical Society, 131, 13230–13231, 2009.

[112] U. Holzwarth and N. Gibson, '*The Scherrer equation versus the "Debye-Scherrer equation"*', Nature nanotechnology, 6, 534, 2011.

[113] V. H. Tiensuu, S. Ergun, and L. E. Alexander, '*X-Ray diffraction from small crystallites*', Journal of Applied Physics, 35, 1718–1720, 1964.

[114] S. Britto, S. Joseph, and P. V. Kamath, '*Distinguishing crystallite size effects from those of structural disorder on the powder X-ray diffraction patterns of layered materials*', Journal of Chemical Science, 122, 751–756, 2010.

[115] I.-K. Jeong, T. Proffen, F. Mohiuddin-Jacobs, and S. J. L. Billinge, '*Measuring Correlated Atomic Motion Using X-ray Diffraction*', The Journal of Physical

Chemistry A, 103, 921–924, 1999.

[116] J. Cho and M. M. Thackeray, '*Structural Changes of $LiMn_2O_4$ Spinel Electrodes during Electrochemical Cycling*', Journal of The Electrochemical Society, 146, 3577–3581, 1999.

[117] N. Ishizawa, D. Du Boulay, M. Hayatsu, S. Kuze, Y. Matsushima, H. Ikuta, M. Wakihara, Y. Tabira, J. R. Hester, K. Tateishi, D. du Boulay, and K. Kawamura, '*Structural disorder along the lithium diffusion pathway in cubically stabilized lithium manganese spinel II. Molecular dynamics calculation*', Journal of Solid State Chemistry, 174, 167–174, 2003.

[118] I. D. Brown and D. Altermatt, '*Bond-Valence Parameters Obtained from a Systematic Analysis of the Inorganic Crystal Structure Database*', Acta Cryst., B41, 244–247, 1985.

[119] N. E. Brese and M. O'Keeffe, '*Bond-valence parameters for solids*', Acta Crystallographica Section B Structural Science, 47, 192–197, 1991.

[120] W. Liu and H. H. Thorp, '*Bond valence sum analysis of metal-ligand bond lengths in metalloenzymes and model complexes. 2. Refined distances and other enzymes*', Inorganic Chemistry, 32, 4102–4105, 1993.

[121] I. D. Brown, '*The Chemical Bond in Inorganic Chemistry: The Bond Valence Model*', Oxford University Press, 2002.

Acknowledgement

The presented study is accomplished at the Helmholtz Institute Ulm (HIU) and Institute of Applied Materials - Energy Storage Systems (IAM-ESS). The financial support of this PhD work by Helmholtz Institute of Ulm is gratefully acknowledged.

First of all, I want to thank my supervisors Prof. Dr. rer. nat. Helmut Ehrenberg who gave me a chance to work with his group in IAM-ESS, for his support, guidance and valuable advice during this PhD work and Prof. Dr. rer. nat. Wolfgang Donner again for his support, nice discussions and his valuable time that he spent for me. I would like to thank a lot my co-supervisor Dr. Michael Knapp who taught me a lot, spent a lot of time for me and answered all my questions, guided me perfectly, helped me find a way to go further with my research.

I wish to thank Dr. Sylvio Indris, Dr. Nilüfer Kiziltas-Yavuz and Dr. Aiswarya Bhaskar for their kind help and guidance about electrochemical part. Additionally, I would like to thank Dr. Björn Schwarz for nice discussions about the structural aspects of the samples and his guidance during the experiments at synchrotron facilities.

This PhD work has benefitted from beamtime allocation by HASYLAB at PETRA III beamline P02.1 in Hamburg and Materials Science and Powder Diffraction (MSPD) beamline at ALBA in Barcelona which are gratefully acknowledged.

Dr. Francois Fauth (ALBA), Dr. Inma Peral (ALBA) and Dr. Manuel Hinterstein (PETRA) for Synchrotron Powder Diffraction Experiments are gratefully acknowledged.

All colleagues in Institute of Applied Materials- Energy Storage Systems are gratefully acknowledged for their support and help during this PhD thesis wok.

Finally, I would like to thank my wife Dr. Nilüfer Kiziltas-Yavuz for being with me always and her great support. I would also like to express my gratitude to our both families who live in Turkey, for their kind support and confidence in me.

Curriculum Vitae

Personal Information

Name	**:**	Murat
Surname	**:**	Yavuz
Date of Birth	**:**	June 12th, 1985
Place of Birth	**:**	Tekirdağ, Turkey
Nationality	**:**	Turkish
Marital Status	**:**	Married

Education

2011-2015	**PhD**, Institute of Applied Materials-Energy Storage Systems (IAM-ESS), **Karlsruhe Institute of Technology (KIT)**, Karlsruhe and Institute of Material Science, TU Darmstadt, Germany
2008-2010	**M.Sc.**, Graduate School of Natural and Applied Sciences, Department of Physics Engineering **Ankara University**, Ankara, Turkey
2003-2008	**Bachelor**, Department of Physics Engineering **Ankara University**, Ankara, Turkey

Academic Experience

2011-present	**Research Associate**	Institute of Applied Materials-Energy Storage Systems (IAM-ESS) and Helmholtz Institute Ulm (HIU), **Karlsruhe Institute of Technology (KIT)**, Karlsruhe
2007-2010	**Research Associate**	Magnetic Materials Research Group, Department of Physics Engineering **Ankara University**, Ankara
2007 (2 months)	**Bachelor Training**	Institute of Ion Beam Physics and Materials Research, **Helmholtz-Zentrum Dresden-Rossendorf (HZDR)**, Germany

Practical Experience

2011-present	**Synchrotron and Neutron Diffraction Experiments at different Beamlines**, DESY (Hamburg), Germany; ALBA (Barcelona), Spain, ESRF and ILL (Grenoble), France
10-13/09/2012	**4th Discus Workshop 2012 (Workshop on Diffuse Scattering and Structure Simulation)**, University of Erlangen-Nürnberg, Nürnberg, Germany
17-21/09/2012	**Hercules Specialised Courses: Neutrons and Synchrotron Radiation in Materials for Energy**, The European Synchrotron Radiation Facility (ESRF) *Practical Trainings* : X-ray and neutron diffraction, Powder diffraction (neutrons and x-rays), X-ray spectroscopy techniques (EXAFS, XANES, XES), Surface diffraction and small angle scattering
18-22/03/2013	**ADD2013-School and Conference on Analysis of Diffraction Data in Real Space,** The European Synchrotron Radiation Facility (ESRF), Grenoble, France

Scientific Publications

1. N. Kiziltas-Yavuz, **M. Yavuz**, S. Indris, N. N. Bramnik, M. Knapp, H. Ehrenberg, and A. Bhaskar, *'The effects of Fe substitution on the structure and electrochemical performance of* $LiNi_{0.5-x}Fe_{2x}Mn_{1.5-x}O_4$ *(x=0, 0.1, 0.15, 0.2) spinel cathode materials'*, 2015.

2. N. Kiziltas-Yavuz, **M. Yavuz**, A. Bhaskar, N. Bramnik, M. Knapp, H. Ehrenberg, *'Influence of Ru-doping on the structural elucidation of high-voltage Ni-Mn cathode materials using in situ synchrotron diffraction'*, 2015.

3. M. Herklotz, J. Weiß, E. Ahrens, **M. Yavuz**, L. Mereacre, N. Kiziltas-Yavuz, C. Dräger, H. Ehrenberg, J. Eckert, F. Fauth, L. Giebeler, and M. Knapp, *'A novel high throughput, facile and universal setup for in situ characterization of batteries'*, Journal of Applied Crystallography, 49, 340-345, 2016.

4. **M. Yavuz**, M. Knapp, S. Indris, W. Donner, H. Ehrenberg, *'XRD Total Scattering investigation of* $Al_{0.57}Sn_{0.43}O_{1.71}$ *Nanoparticles'*, Journal of Applied Crystallography, 48, 1699-1705, 2015.

5. G. Balachandran, D. Dixon, N. Bramnik, A. Bhaskar, **M. Yavuz**, L. Pfaffmann, F. Scheiba, H. Ehrenberg, *'Elucidation of the Electrochemical Eeaction Mechanism in* MFe_2O_4 *(M = Ni, Co) Conversion-Type Negative Electrode Systems by In situ X-ray Absorption Spectroscopy'*, ChemElectroChem, 10, 1510-1518, 2015.

6. R. Chen, S. Ren, **M. Yavuz**, A. A. Guda, R. Witter, M. Fichtner, and H. Hahn, *'Li+ Intercalation in isostructural* Li_2VO_3 *and* Li_2VO_2F *with* O^{2-} *and mixed* O^{2-}/F^- *anions'*, Physical Chemistry Chemical Physics, 17, 17288, 2015.

7. I. Bezza, M. Kaus, R. Heinzmann, **M. Yavuz**, M. Knapp, S. Mangold, S. Doyle, C. P. Grey, H. Ehrenberg, S. Indris, I, Saadoune, *'Mechanism of the delithiation/lithiation process in* $LiFe_{0.4}Mn_{0.6}PO_4$*: In situ and ex situ investigations on long-range and local structures'*, The Journal of Physical Chemistry C, 119, 9016-9024, 2015.

8. K. Kleiner, D. Dixon, P. Jakes, J. Melke, **M. Yavuz**, C. Roth, K. Nikolowski, V. Liebau, and H. Ehrenberg, *'Fatigue of* $LiNi_{0.8}Co_{0.15}Al_{0.05}O_2$ *in Commercial Li Ion Batteries'*, Journal of Power Sources, 273, 70-82, 2015.

9. R. Chen, M. Knapp, **M. Yavuz**, S. Ren, R. Witte, R. Heinzmann, H. Hahn, H. Ehrenberg, and S. Indris, *'Nanoscale spinel* $LiFeTiO_4$ *for intercalation pseudocapacitive* Li^+ *storage"*, Phys. Chem. Chem. Phys, 17, 1482-1488, 2015.

10. **M. Yavuz**, N. Kiziltas-Yavuz, A. Bhaskar, M. Scheuermann, S. Indris, F. Fauth, M. Knapp, and H. Ehrenberg, *'Influence of Iron on the Structural Evolution of* $LiNi_{0.4}Fe_{0.2}Mn_{1.4}O_4$ *during Electrochemical Cycling Investigated by in situ Powder Diffraction and Spectroscopic Methods'*, Zeitschrift für anorganische und allgemeine Chemie, 640, 3118-3126, 2014.

11. R. Chen, M. Knapp, **M. Yavuz**, R. Heinzmann, D. Wang, S. Ren, V. Trouillet, S. Lebedkin, S. Doyle, H. Hahn, H. Ehrenberg, and S. Indris, *'Reversible* Li^+ *Storage in a* $LiMnTiO_4$ *Spinel and Its Structural Transition Mechanisms'*, J. Phys. Chem. C, 118, 12608-12616, 2014.

12. N. Kiziltas-Yavuz, A. Bhaskar, D. Dixon, **M. Yavuz**, K. Nikolowski, L. Lu, R.-A. Eichel, and H. Ehrenberg, *'Improving the Rate Capability of High Voltage Lithium-Ion Battery Cathode Material* $LiNi_{0.5}Mn_{1.5}O_4$ *by Ruthenium Doping'*, Journal of Power Sources, 267, 533-541, 2014.

13. G. Lieser, M. Schroeder, H. Geßwein, V. Winkler, S. Glatthaar, **M. Yavuz** and J. R. Binder, *'Sol-gel processing and electrochemical characterization of monoclinic* Li_3FeF_6*'*, Journal of Sol-Gel Science and Technology, 71, 50-59, 2014.

Conference Publications

- □ PDF Analysis of Disordered Rock-Salt-Type Li_2VO_2F

  M. Yavuz, *I. Peral, M. Knapp, R. Chen, H. Ehrenberg*

  23rd Annual Conference of the German Crystallographic Society 2015, Göttingen, Germany

- □ *In situ* PDF Experiments during Electrochemical Cycling of Cathode Materials for Li-ion Batteries

  M. Yavuz, *N. K. Yavuz, M. Knapp, K. Nikolowski, H. Ehrenberg*

  Structural and in situ materials science at Beamline P02.1@PETRA III, 2013, Hamburg, *Germany*

- □ XRD Total Scattering and Pair Distribution Function (PDF) Measurements on $Li(Ni,Mn)_2O_4$ Spinel

  M. Yavuz, *N.K. Yavuz, M. Knapp, K. Nikolowski, H. Ehrenberg*

  2nd International Conference on Materials for Energy 2013 (Enmat II), Karsruhe Convention Center, 2013, Karlsruhe, Germany

- □ Influence of the Synthesis Route of $Li(Ni,Mn)_2O_4$ on the Structure measured by XRD

  M.Yavuz, *N.K.Yavuz, M.Knapp, K.Nikolowski, H.Ehrenberg*

  ADD2013-School and Conference on Analysis of Diffraction Data in Real Space 2013, Grenoble, France

- □ PDF Experiments and In-situ Investigations of Li-ion Battery Electrode Materials

  M. Yavuz, *N. K. Yavuz, K. Nikolowski, M. Knapp, H. Ehrenberg*

  Hercules Specialised Courses: Neutrons and Synchrotron Radiation in Materials for Energy 2012, Grenoble, France

- □ Total Scattering Experiments on Li-ion Battery Electrode Materials

  M. Yavuz, *N. K. Yavuz, K. Nikolowski, M. Knapp, H. Ehrenberg*

  13th *Electrochemical Talks (UECT 2012*), Neu-Ulm, Germany

- Electrical Force Microscopy and SKPM Investigations of Pb Doped CdS Films

  *S.A.Klimova, M.Arslan, S.V.Stetsyura, **M.Yavuz**, A.A.Serdobintsev, S.B.Venig, Y.Elerman*

  6th Nanoscience and Nanotechnology Conference 2010, Cesme/Izmir, Turkey

- Investigation of CdS Langmuir-Blodgett Thin Films by Using EFM Technique

  *S.A.Klimova, **M.Yavuz**, S.V.Stetsyura, M.Arslan, A.A.Serdobintsev, S.B.Venig, Y.Elerman*

  6th Nanoscience and Nanotechnology Conference 2010, Cesme/Izmir, Turkey

  International Journal of Material Science and Electronics Research (IJMSER)

- Syntesis of Graphene via Scotch Tape Method

  *Z. Varol, I. Mutlay, **M. Yavuz**, N. Yildiz and A. Calimli*

  International Conference on Nanomaterials and Nanosystems 2009, Istanbul, Turkey

- Investigation of the LSH Thin Films with Different pH by Scanning Probe Microscopy (AFM, EFM, SKM, SCM) Measurements

  *S.A.Klimova,**M.Yavuz**,S.V.Stetsyura,G.Durak,E.G.Glukhovskoy,M.Arslan,S.B.Venig, Y.Elerman*

  5th Nanoscience and Nanotechnology Conference 2009, Eskisehir, Turkey

- Scanning Probe Microscopy Measurements of the Langmuir-Blodgett Organic Thin Films

  *S.A.Klimova,**M.Yavuz**,S.V.Stetsyura,G.Durak,E.G.Glukhovskoy,M.Arslan,S.B.Venig, Y.Elerman*

  5th Nanoscience and Nanotechnology Conference 2009, Eskisehir, Turkey

- The Investigation of Magnetic Properties of $Si/SiO_2/PEI/(Fe_3O_4)/PAH)_x$ (x= 6, 11, and 16) Nanocomposite Multilayers

  *O.A.Inozemtseva, **M.Yavuz**, A.M.Yaschenok, S.B.Venig, Y.Elerman*

  5th Nanoscience and Nanotechnology Conference 2009, Eskisehir, Turkey

☐ The Investigation of Magnetic Ribbons of $Nd_{13.4}Fe_{68.6}Co_{11.4}B_{6.4}Zr_{0.2}$ by Using Magnetic Force Microscopy (MFM)

__M.Yavuz__, S.Ener, E.Esiguzel, Y.Elerman

5th Nanoscience and Nanotechnology Conference 2009, Eskisehir, Turkey

☐ Effect of Heat Treatment on the Magnetic Properties of $Nd_2Fe_{14}B$ Alloy

__M.Yavuz__, S.Ener, E.Yuzuak, I.Dincer, Y.Elerman

25th International Physics Conference 2008, Mugla, Turkey

☐ Magnetic and Structural Characterization of Nanostructured Melt-Spun $La_{0.5}Pr_{0.5}Mn_2Si_2$ Ribbons

B.Emre, __M.Yavuz__, E.Yuzuak, S.Ener, I.Dincer, Y.Elerman

4*th Nanoscience and Nanotechnology Conference 2008, Istanbul, Turkey*

☐ Effect of Melt Spinning Process on the Magnetic Properties of $Nd_2Fe_{14}B$ Alloy

S.Ener, __M.Yavuz__, B.Emre, E.Yuzuak, I.Dincer, Y.Elerman

4*th Nanoscience and Nanotechnology Conference 2008, Istanbul, Turkey*